On the diversity of gibbsite crystal morphologies

Shapes, defects and kinetics

Chantal Sweegers

On the diversity of gibbsite crystal morphologies

Shapes, defects and kinetics

een wetenschappelijke proeve op het gebied van de
Natuurwetenschappen, Wiskunde en Informatica

Proefschrift

ter verkrijging van de graad van doctor
aan de Katholieke Universiteit Nijmegen,
volgens besluit van het College van Decanen
in het openbaar te verdedigen op
dinsdag 3 april 2001,
des namiddags om 3.30 uur precies

door

Chantal Sweegers

geboren op 13 juli 1971
te Heeze

Promotor:	Prof. Dr. E. Vlieg
Co-promotoren:	Dr. H. Meekes Dr. W.J.P. van Enckevort
Manuscriptcommissie:	Prof. Dr. P. Bennema Dr. P.J.C.M. van Hoof (Organon N.V., Oss) Prof. Dr. G.J. Witkamp (TU Delft)

Sweegers Chantal
On the diversity of gibbsite crystal morphologies
– Shapes, defects and kinetics –
PhD Thesis, University of Nijmegen, The Netherlands
With summary in Dutch
ISBN 90-9014587-7
Cover design by: Femke Gerris, fmegerris@hotmail.com
Printed by: UniversiteitsDrukkerij TUE
The work presented in this thesis was financially supported by
Billiton International Metals B.V.

Contents

Chapter 1

General introduction

1.1 Introduction

In this thesis, the results of a study into the formation and habit of gibbsite crystals grown from aqueous caustic solutions are presented. Gibbsite is an aluminium trihydroxide mineral, γ-Al(OH)$_3$, and is an important technical intermediate in the production of alumina, Al_2O_3. The latter compound is the material from which aluminium is obtained. Other industrial applications of gibbsite are white pigment, fire retardant filler and reinforcing agent for plastics and rubber.

Gibbsite is recovered from the ore bauxite in the commercial production of alumina via the Bayer process, through crystallisation from a sodium aluminate solution, and is subsequently calcined to alumina, Al_2O_3. The alumina industry is very interested in the gibbsite crystallisation step, because it offers the purification and separation of gibbsite particles from bauxite within a single process step. The quality of the gibbsite crystals and agglomerates determines the quality of the successive calcination product, alumina. For that reason, the particle size, morphology, strength, amount of agglomeration and incorporation of impurities are important parameters. To improve product quality and productivity, fundamental knowledge of the crystallisation process, i.e. nucleation, crystal growth and agglomeration, is beneficial to optimise and control the crystallisation step. Despite its importance and the fact that alumina has been produced for more than hundred years via the Bayer process, the crystal growth mechanism of gibbsite is still not well understood. Therefore, gibbsite crystallisation has been studied widely over the last decades and continues to be the subject of a substantial amount of research efforts.

In this introduction, an overview is given of the use of gibbsite in the aluminium production industry. Furthermore, some physical and chemical properties of gibbsite are described. Since a substantial amount of research has already been reported by other authors, the studies on the growth of gibbsite are briefly reviewed. Finally, an outline of the thesis is given.

1.2 The production of aluminium

Aluminium is the most abundant metallic element in the earth's crust (8%) and is present in most rocks, vegetation and animals [1]. Aluminium occurs rarely in a pure state and is normally found in compounds with other elements, like oxygen, silica, alkali and alkaline-earth metals, fluorine, and as hydroxides, sulphates and phosphates. All these aluminium minerals are quite stable.

The chemical production process of aluminium was developed throughout the 18th and 19th century. In 1887 the Austrian chemist Karl Joseph Bayer developed the process for the production of Al_2O_3 from bauxite by dissolving the bauxite in alkali, leaving the insoluble impurities behind. The first production plant was constructed in 1901 in East St. Louis Illinois. The production of aluminium through the reduction of alumina with cryolite (aluminium fluoride with sodium) was developed in the late 19th century. This electrolytic process was discovered independently, and almost simultaneously, in early 1886 by Charles Martin Hall in Oberlin, Ohio, and Paul L.T. Héroult in Gentilly, France.

In less than three years the invention was implemented industrially in North America and in Europe. With the development of the Bayer process and the Hall-Héroult process, the technology for the commercial production of pure aluminium from bauxite was realised. This has resulted in a rapid growth of the aluminium industry in the last decade of the 19th century. The basic outline of the production of aluminium is presented in figure 1.1.

Bauxite

Bauxite is the primary ore of aluminium and consists of aluminium oxide hydroxide minerals with iron and other elements like silicon and titanium. The presence of iron accounts for the red colour of the bauxite. Commonly, gibbsite (γ-Al(OH)$_3$) and boehmite (γ-AlO(OH)) are the main constituents of bauxite. Typical compositions for the industrial use of bauxites are: $Al_2O_3.xH_2O$ 35-60 %, SiO_2 1-10 %, Fe_2O_3 7-30 %, TiO_2 2-4 %, and F, P_2O_5, V_2O_5, 0.05-0.2 %.

Bauxite deposits are confined to several large areas in tropical and sub-tropical regions, like the Carribean, West Africa, India and Australia, and have been produced by the weathering of surface rocks by hot, torrential rains over thousands of years. Bauxite is found in 44 countries around the world and mined in 24 countries with some deposits in Europe. Bauxite is almost invariably refined into alumina through the Bayer process.

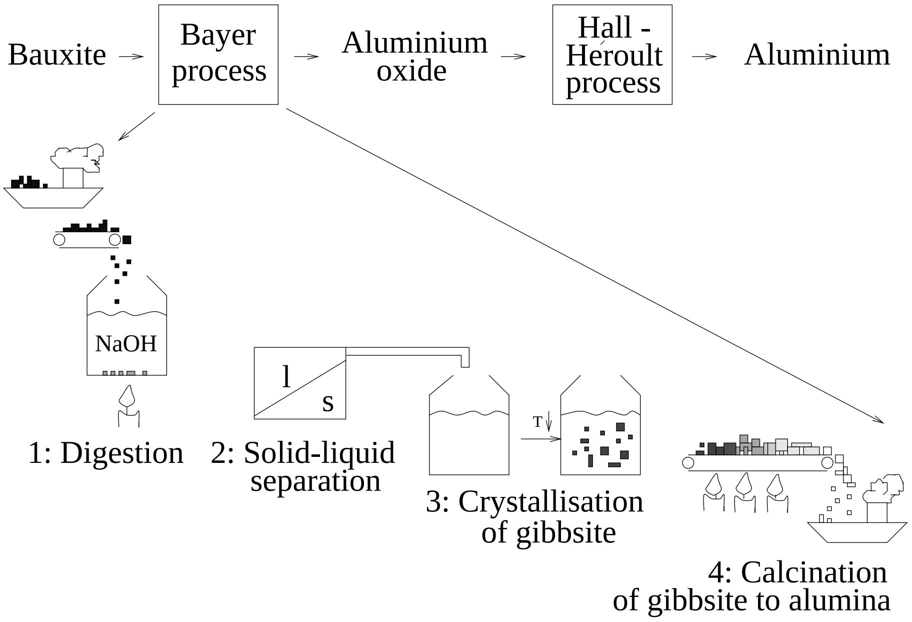

Figure 1.1: The basic outline of the production of aluminium. The main steps are: the production of aluminium oxide from bauxite by the Bayer process, and the extraction of aluminium from alumina by the Hall-Héroult process.

The Bayer process

In the Bayer process, the aluminium oxide hydroxide minerals are digested in caustic soda solution at high temperature and pressure. Most of the impurities remain solid and are removed before the hot red-brown sodium aluminate solution enters the chain of, usually, fifteen crystallisation tanks. The sodium aluminate solution is cooled and seeded with fine crystals of aluminium hydroxide. During the crystallisation step, the fine seed particles grow by deposition of $Al(OH)_3$ from the solution. New particles are formed by (secondary) nucleation. Finally, the solid particles of aluminium hydroxide are classified. The larger crystals are removed as product, while the finer particles are recycled as seed crystals to grow further. The depleted solution is returned to the start of the process and reused to digest bauxite.

Figure 1.2: Crystallisation tanks of an alumina plant.

In an industrial crystalliser, gibbsite forms agglomerates of about 100 microns in size. The agglomerates consist of small gibbsite crystals of different shapes and sizes, oriented in all directions. In figure 1.3, gibbsite agglomerates from an alumina plant in Australia, and from a plant in South America are shown. These agglomerates are 80 to 150 microns in diameter. There is a large difference in appearance due to a difference in the raw bauxite and process conditions. The process conditions are chosen such as to yield a high productivity and a product of desired particle size, strength and purity.

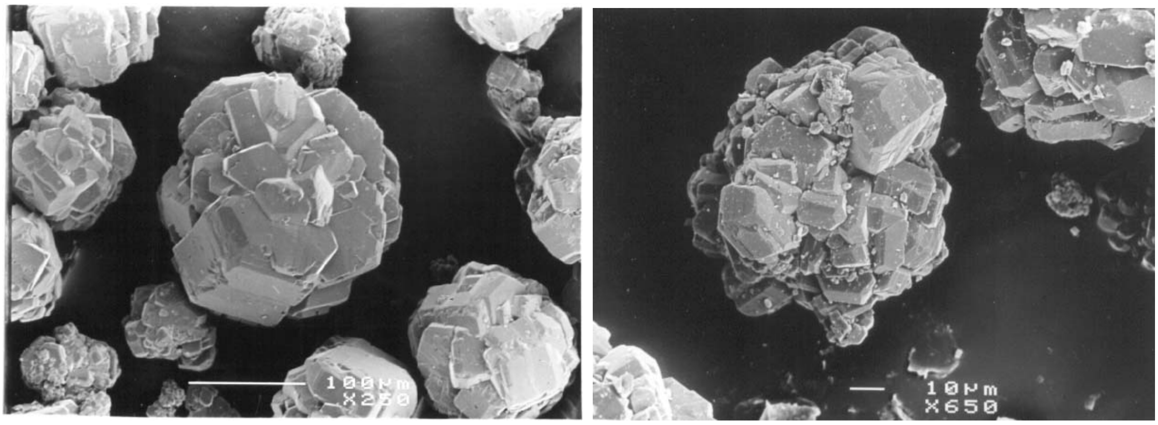

(a) (b)

Figure 1.3: Gibbsite agglomerates from an alumina plant of (a) Australia, and (b) South America. The scale bars are 100 and 10 μm, respectively.

The collected solid particles of aluminium hydroxide are subsequently transformed to aluminium oxide in the calcination process. A fluidised bed reactor operating at 1000°C is used to remove the crystal water molecules, leaving a fine, white, anhydrous powder of alumina, Al_2O_3.

The process in concept has changed only little the last 100 years since its first development. For the production of 1 tonne of alumina, about 2-3 tonnes of bauxite are required.

The Hall-Héroult process

Aluminium is separated from its bonded oxygen by an electrolytic process. The electrolyte in the cell is a mixture of cryolite (Na_3AlF_6), AlF_3 and fluorspar (CaF_2) in the ratio 87:5:8 to which alumina is added up to 8%. The alumina is dissolved in the molten cryolite at 970°C and reacts with AlF_6^{3-} ions to give complex oxygen containing ions as $Al_2OF_6^{2-}$ and $Al_2O_2F_4^{2-}$. These transform to pure aluminium. The mixture of alumina and electrolytic materials connected to the molten aluminium is the cathode; the anode is made of carbon which changes to CO_2 during electrolysis. A simple representation of the overall reaction in the cell is given by:

$$2Al_2O_3(\text{dissolved}) + 3C(s) \rightarrow 4Al(l) + 3CO_2(g). \tag{1.1}$$

The process takes place in huge electrolytic cells. The cells are about 10 meters long and several meters wide. The carbon anode is about 2 meters in diameter and decomposes alumina into Al and O. It lasts about three weeks before it is burned away.

Aluminium melting is a high energy consuming process and smelters are located near cheap sources of electricity, usually hydroelectric, nuclear or coal-fired. For the production of 1 tonne of aluminium, about 2 tonnes of alumina are required.

(a) (b)

Figure 1.4: (a) Electrolytic cell for the extraction of aluminium from alumina, and (b) used carbon anodes.

1.3 Properties of gibbsite

Structure

Gibbsite (or hydrargillite), γ-Al(OH)$_3$, has a monoclinic space group, P2$_1$/n, with cell parameters $a = 8.684$ Å, $b = 5.078$ Å, $c = 9.736$ Å and $\beta = 94.54°$ [2]. There are eight Al(OH)$_3$ molecules per unit cell.

Triclinic crystals embedded in the monoclinic ones have also been observed, with $a = 17.338$ Å, $b = 10.086$ Å, $c = 9.730$ Å and $\beta = 94.1$ ° [3,4]. The structure of these triclinic crystals shows a large similarity to the monoclinic one.

The structure of gibbsite is pseudohexagonal with the c-axis as the pseudohexagonal axis. The OH groups, assumed to be spherical, are stacked in two close packed layers A and B forming a sheet structure [4], with the OH groups of layer B right above the triangle formed by the 3 OH groups in layer A. The aluminium atoms are distributed in the octahedral holes in such a way that the entire double layer is electrically neutral, i.e. two thirds of the holes are filled. The distribution of the aluminium atoms sandwiched between the two OH$^-$ sheets is such that they are in a regular hexagonal arrangement, as shown in figure 1.5. Viewed perpendicular to $\boldsymbol{c}$, the aluminium atoms are arranged along straight lines normal to the basal plane. In this way, each Al atom is octahedrally coordinated to six OH groups and each OH group is coordinated to two Al atoms causing bonds in the double layer AB. As a consequence of partially occupied holes, the lattice is somewhat deformed [5,6].

The unit cell contains two such AB layers. The double layers are stacked with the OH$^-$ ions of the third OH layer placed above those of the second OH layer [3–6]. The stacking can be represented by ...-AB-BA-... Three of the hydrogen atoms are located within the oxygen layers whereas the three others are placed between the Al(OH)$_3$ layers, resulting

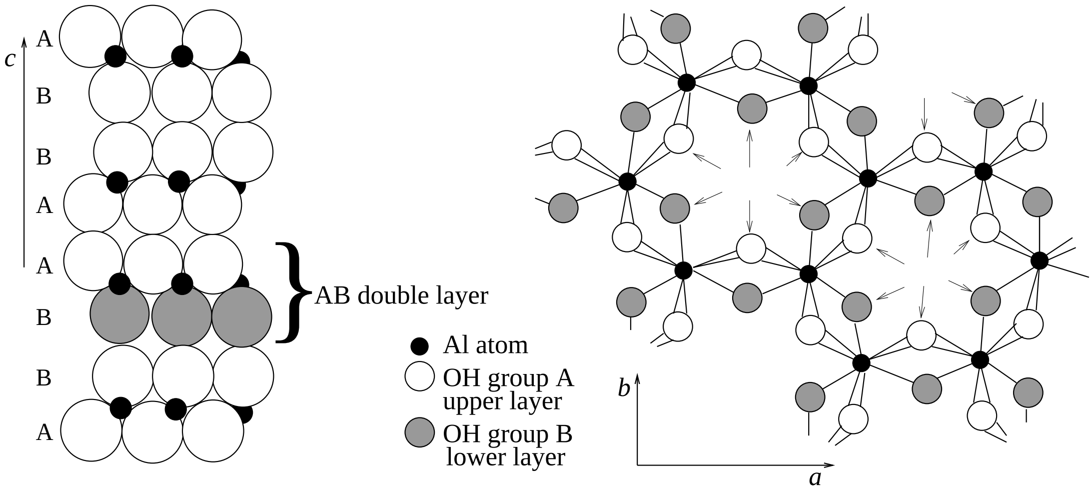

Figure 1.5: Projections of the atomic arrangement of the gibbsite structure; on the left, a view along ***b***: the structure consists of double layers (AB) of close packed OH groups with Al atoms occupying two third of the octahedral interstices within the layers; on the right, a top-view of an AB layer along ***c***: each aluminium atom is octahedrally bonded to three O atoms of layer A and to three O atoms of layer B. Due to the fact that $\frac{1}{3}$ of the octahedral interstices is empty, the hexagonal arrangement is somewhat distorted [4].

in hydrogen bonds linking the adjacent double layers [2]. The O-H...O values of 2.781, 2.829 and 2.888 Å agree with the hydrogen bridge distances found in other compounds containing H-bonds.

Morphology

The crystal morphology of natural gibbsite is usually reported as pseudohexagonal tabular parallel to the {001} basal faces, with {100} and {110} side faces and {101} and {112} chamfered faces, giving platelets forming nearly regular hexagons [4,5]. Excellent cleavage parallel to the basal plane is a result of the layer structure [6]. Gibbsite produced in the Bayer process or synthesised in the laboratory in addition forms prismatic crystals and aggregates, depending on the crystallisation conditions [7–9]. Sometimes, lozenge-shaped crystals have been observed, with side faces being indexed as {110} [10].

The effect of sodium and potassium on the morphology of gibbsite has been reported [4]: pseudohexagonal, elongated prisms prevail when gibbsite is precipitated from K-aluminate solutions as compared to Na-aluminate solutions. The reason for this is still unclear.

Another characteristic of gibbsite crystals is twinning. In natural gibbsite, twinning usually occurs on {001} and about the [130] rotation axis with {001} as the composition plane. Twinning on {100} and {110} has occasionally been found [6, 11]. Twinning has also been reported for synthetic gibbsite [7, 12].

Both natural and synthetic gibbsite crystals exhibit a large variation in their morphology. Up to now, little research has been done on the morphological appearance of gibbsite. The growth morphology of gibbsite is the main subject of this thesis.

Impurities

Analysis of natural gibbsite usually shows the presence of Fe_2O_3 and minor amounts of other oxides [6]. Some oxides are undoubtedly also present as impurities. Technical gibbsite produced by the Bayer process usually contains a few hundredths up to several tenths of a percent of alkali metal ions [4]. It is shown that these small amounts of alkali atoms are atomically dispersed in the crystal lattice of gibbsite. Probably, these ions substitute the Al^{3+} ions in the structure.

Other aluminium trihydroxide polymorphs

Apart from the above mentioned $Al(OH)_3$ mineral gibbsite, other polymorphic structures exist, like bayerite, nordstrandite and doyleite [3,5,13].

The space group symmetry of bayerite is $P2_1/a$. The structure is based on a stacking of neutral $Al(OH)_3$ double layers similar to gibbsite. However, in the bayerite mineral they are ordered in an ...-AB-AB-AB... sequence. Accordingly, the *c*-axis is somewhat shorter. Bayerite crystals usually occur as somatoids which are not enclosed by crystal faces.

The third form of aluminium trihydroxide is nordstrandite. This mineral is rare in nature, but readily formed during synthesis, generally in association with gibbsite and/or bayerite. The nordstrandite structure has a triclinic unit cell and consists of the same AB layers as in gibbsite and bayerite. It has been suggested that the nordstrandite lattice is built up from two double layers with bayerite sequence and two double layers with gibbsite sequence [4].

In 1985, the structure determination of an other trihydroxide aluminium mineral was reported, named doyleite [4]. It crystallises in the tabular morphology typical for gibbsite. The symmetry was determined to be triclinic, space group P1 or $P\bar{1}$. Structural data indicate that in this form of $Al(OH)_3$, the stacking sequence of the hydroxyl double layers can be considered to be an intermediate between the triclinic gibbsite and nordstrandite. Whether or not this material can be considered as a fourth modification of $Al(OH)_3$ is still an open question.

The natural abundance of the polymorph gibbsite has suggested that this polymorph is the thermodynamically most stable form of $Al(OH)_3$, despite the fact that bayerite has a higher density ($2.53\ g.cm^{-1}$) as compared to gibbsite ($2.42\ g.cm^{-1}$) [4]. The reason for the formation of the other aluminium trihydroxide minerals is not well understood. A possible cause is the presence of impurities, which would determine the stacking sequence of the hydroxyl groups in the double layers. Several authors believe that alkali atoms are necessary to stabilise the gibbsite structure [4]. If impurities determine the structure of the $Al(OH)_3$ polymorphs, the relative thermodynamical stability would be less relevant.

1.4 Gibbsite crystal growth

Over the years, the crystallisation of gibbsite from caustic aluminate solutions has been investigated intensively. In these studies, (secondary) nucleation, growth, agglomeration, and the induction period preceded by crystallisation received considerable attention.

Growth of gibbsite proceeds extremely slow and is considered to be surface reaction controlled. This was concluded from the very low growth rate, its dependence on surface area of the solid and the negligible effect of agitation on growth [8, 9, 14]. It is proposed that the rate limiting step is the restructuring of the aluminate ion at the interface into octahedrally coordinated ordered species, which are formed by a combination of aluminate ions [10, 15]. A loose polymeric network which transforms into crystalline $Al(OH)_3$ upon further densification is also proposed by Gerson et al. [16]. In 1997, Addai-Mensah [17] reported the occurrence of a poorly-formed crystalline material at the surfaces of gibbsite at the early stage of unseeded crystallisation experiments using pure Bayer liquors. The crystalline surface layer turned out to be $Al(OH)_3$ and was suggested to be bayerite.

The crystal growth mechanism has been studied using batch crystallisers [14, 18–20]. These studies have led to kinetic models for the growth rate of gibbsite crystals, which are based on:

$$\boldsymbol{R} = k_0 \exp\left(\frac{-E}{RT}\right) * S^2, \tag{1.2}$$

with k_0 a kinetic coefficient, E the activation energy for 2D nucleation, T the crystallisation temperature and S the crystallisation driving force (as detailed in chapter 4). From the fits of expression (1.2) to experimental growth rates, various growth rate constants k_0 and E were obtained.

The square dependence of the growth rate on the driving force in eq. 1.2 suggests that gibbsite crystallisation is controlled by a screw dislocation growth mechanism. However, the growth rate equation of gibbsite crystallisation based on eq. 1.2 was not based on actual growth mechanisms, but was the result of semi-empirical data fit procedures, and therefore this does not reveal the actual growth mechanism.

Some authors investigated the growth mechanism of gibbsite crystals in more detail. Misra et al. [8] suggested that growth takes place by the axial and radial enlargement of hexagonal prisms as well as by the formation of new hexagonal plates on seed surfaces, presumably due to the existence of defects. The occurrence of dislocations and other growth defects, like twinning, internal boundaries and plate-like branching, which can affect the crystal growth mechanism, was shown by Gnyra et al. [7]. Brown et al. [9] suggested that the growth of the basal faces proceeds via a surface nucleation mechanism with little or no contribution from screw dislocations. The continuous spreading mechanism on the basal face was also observed by Cornell et al. [21]. More recently, the results of an *in situ* microscopic study suggested that at low supersaturation growth of the basal faces is determined by dislocation growth and that at higher supersaturation a continuous birth and spread mechanism is dominant [22]. Prismatic faces are suggested to grow by a dislocation mechanism. AFM studies by Freij et al. [23] showed the presence of various defects on the basal face of gibbsite, which might influence the crystal growth processes.

As described in chapter 3, surface examination of the gibbsite particles confirmed that 2D nucleation and dislocation growth are important mechanisms for the growth of gibbsite crystals. However, as will be shown in this thesis, the growth mechanism that occurs depends on the type of crystal morphology which in each case is determined by the defect structure and the presence of impurities.

A repeatedly asked question concerns the influence of impurities on the gibbsite crystallisation process and the degree to which they affect the properties of the crystals. It is well-known that the growth morphology can be altered by the presence of trace amounts of certain impurities atoms or molecules which adsorb on the surface of growing crystals.

The caustic aluminate solution of the Bayer process contains a large number of organic carbon compounds derived from the humic matter in the starting bauxite ore. Consequently, many studies have been reported on the nature of specific organic compounds in Bayer liquors and their effect on the different stages in gibbsite crystallisation from synthetic sodium aluminate solutions [24–33]. These organic compounds are known to lower the productivity, to increase the impurity content of crystallised gibbsite and to cause generation of fine crystalline material. The mechanism by which these compounds inhibit gibbsite crystallisation is suggested to be due to, firstly, the adsorption of the organic ligands onto the gibbsite surface and, secondly, the complex formation of the compounds with aluminate ions and/or clusters in the sodium aluminate solutions.

The main inorganic impurities in Bayer liquors are sodium oxalate and other sodium salts. Sodium oxalate, $Na_2C_2O_4$, is nearly always the most important impurity in alumina. Although it has an effect on the calcination step, it does not harm the Al metal purity. The sodium salts of CO_3^{2-}, SO_4^{2-}, Cl^- and F^- all interfere with gibbsite crystallisation, probably because they increase the Na^+ concentration in the solution and consequently the solubility of $Al(OH)_3$. Some studies have been done on the influence of inorganic impurities on the crystallisation of gibbsite from sodium aluminate solutions. Brown [34] studied the effect of copper ions on the crystallisation of gibbsite using scanning electron microscopy. He found that copper ions adsorb preferably on the $\{001\}$ faces and further induce secondary nucleation, mainly on the prismatic faces of the gibbsite seed crystals. The roughened seed surfaces and the tiny crystallites promote agglomeration during the crystallisation process. He also studied the effect of calcium ions on the agglomeration of gibbsite [35] and concluded that small amounts of calcium ions in caustic aluminate solutions can lead to enhanced agglomeration of gibbsite particles. The effect of iron atoms was studied by Veesler et al. [36]. They suggested that gibbsite growth is blocked at low supersaturations by impurity adsorption, resulting in a dead zone.

1.5 Scope of this thesis

The present study concerns the growth habit and growth behaviour of gibbsite crystallised from sodium aluminate solutions, in order to understand the fundamental processes involved in the crystallisation of gibbsite in the Bayer process. Careful evaluation of properties such as the defect structure of the small particles, growth rate dispersion, habit modification and solvent uptake is of great importance in defining and formulation of industrial processing requirements as well as optimising product performance. The growth morphology and growth mechanisms of gibbsite are studied both by experiment, i.e. examining crystals *ex-situ* and *in-situ*, and by theory. Almost all chapters emphasise the dominant role of the defect structure of the crystals as the cause for the large diversity of gibbsite morphologies.

Laboratory experiments on the growth of gibbsite crystals from unseeded sodium aluminate solutions resulted in crystals (and agglomerates) with various morphologies. In chapter 2, three main morphologies are described: lozenge-shaped platelets, hexagonal platelets and prismatic crystals. Many of these crystals are twinned. The effect of various kinds of twinning on the growth morphology and growth kinetics is discussed. It is concluded that lozenge-shaped crystals exhibit the basic morphology of gibbsite crystals instead of the hexagons, normally considered as the basic morphology in the literature. These latter crystal shapes and in addition the prisms, are found to be formed through single or multiple twinning, dislocations and the presence of impurities.

A study of the surface topography using optical and atomic force microscopy is presented in chapter 3. With this study a detailed understanding of the growth and interface properties of the three main types of gibbsite crystals is obtained. *Ultra thin* lozenge-shaped crystals are completely determined by a 2D nucleation growth mechanism. Most gibbsite crystals, however, contain many dislocations and defects. Several growth phenomena, like 2D nuclei, monomolecular and higher steps, growth hillocks, contact nucleation and planar faults are described. It turns out that the growth features observed are related to the different gibbsite crystal morphologies found.

The occurrence of twinning makes it difficult to investigate the growth kinetics of the different types of gibbsite crystals separately under industrial plant conditions. *In-situ* observations of growing gibbsite crystals with optical microscopy is the best approach to study the growth properties of individual faces for the different crystal types. The growth rate measurements are presented in chapter 4. To interpret these results, a definition of the driving force adapted for gibbsite crystallisation from caustic aluminate solution is derived in this chapter. Furthermore, besides the well-known crystal growth models for birth and spread and spiral growth, a new analytical model for contact nucleation is introduced. Fits of the growth data points with the analytical expressions for birth and spread, spiral growth and contact nucleation reveals that for all faces, birth and spread and contact nucleation are the most probable growth mechanisms under various growth conditions. This is in accordance with the surface topography studies reported in chapter 3.

In chapter 5, the growth morphology of gibbsite crystals is characterised for a wide range of growth conditions using scanning electron microscopy. These observations lead to a description of a general morphology evolution during the crystallisation process. Crystallisation starts with the formation of small, rounded hexagons, which develop upon further growth into large blocks with many defects and stress regions. Depending on the driving force (and caustic concentration), the different stages of the process are reached sooner or later. Experiments to study the influence of inorganic impurities on the growth of gibbsite crystals, like metal hydroxides and sodium salts, are described. It shows that the presence of inorganic impurities does not have a significant effect on the gibbsite morphology. In contrast, gibbsite crystals grown from potassium aluminate solutions show a morphology which is elongated along the c-axis.

The theoretical morphology of gibbsite on the basis of an extended connected net analysis is the subject of chapter 6. This method relies on determining crystal faces parallel to connected nets in the crystal structure, followed by calculating the edge energy of 2D nuclei for each face. By ascribing the highest morphological importance to the faces with the highest value of edge (free) energy, i.e. the highest nucleation barrier, the growth morphology is obtained. It is shown on theoretical grounds that, despite the fact that the structure of gibbsite is pseudohexagonal, a lozenge-shaped morphology is the most favoured one.

References

[1] N.N. Greenwood and A. Earnshaw, Chemistry of the Elements (Pergamon Press, 1986) 1^{st} edition.

[2] H. Saalfeld and M. Wedde, Z. für Kristall. 139 (1974) p. 129.

[3] B.C. Lippens, Structure and Texture of Aluminas, PhD thesis Technische Hogeschool Delft (1961).

[4] K. Wefers and C. Misra, Oxides and Hydroxides of Aluminium, Technical Report Technical Paper no. 19, revised Alcoa Research Laboratories, Pittsburgh, Pennsylvania (1987).

[5] A.C.D. Newman, Chemistry of Clays and Clay minerals (Longman Scientific & Technical, 1987) 2^{nd} edition.

[6] W.A. Deer, R.A. Howie and J. Zussman, An Introduction to Rock Forming Minerals (Longman Scientific & Technical, 1992) 2^{nd} edition.

[7] B. Gnyra, R.F. Jooste and N. Brown, J. Cryst. Growth 21 (1974) p. 141.

[8] C. Misra and E.T. White, J. Cryst. Growth 8 (1971) p. 172.

[9] N. Brown, J. Cryst. Growth 12 (1972) p. 39.

[10] M.-Y. Lee, A.L. Rohl, J.D. Gale, G.M. Parkinson and F.L. Lincoln, IChemE 74 (1996) p. 739.

[11] W.L. Roberts, G.R. Rapp jr. and J. Weber, Encyclopedia of minerals (Van Nostrand Reinhold Company, New York, 1974).

[12] L. Armstrong, J. Hunter, N. Calos, G. Miller, P. Uwins and J. Barry, Proc. of the Fourth International Alumina Quality Workshop (1996) p. 239.

[13] K. Wefers and G.M. Bell, Oxides and Hydroxides of Aluminium, Technical Report Technical Paper no. 19 Alcoa Research Laboratories, Pittsburgh, Pennsylvania (1972).

[14] C. Misra and E.T. White, Chem. Eng. Prog. Symp. Series 110 67 (1971) p. 53.

[15] J. Zambo, Light Metals (1986) p. 199.

[16] A. Gerson, J. Addai-Mensah, J. Counter, T. Soar and J. Watson, Light Metals (1998) p. 167.

[17] J. Addai-Mensah, Min. Eng. 10 (1997) p. 81.

[18] W.R. King, Light Metals (1973) p. 551.

[19] A. Halfon and S. Kaliaguine, Can. J. Chem. Eng. 54 (1976) p. 160.

[20] E.T. White and S.H. Bateman, Light Metals (1988) p. 157.

[21] R.M. Cornell, C.F. Vernon and D.S. Pannett, Proc. of the Fourth International Alumina Quality Workshop (1996) p. 97.

[22] M.-Y. Lee and G. Parkinson, J. Cryst. Growth 198/199 (1999) p. 270.

[23] S. Freij, M.-Y. Lee, M. Reyhani and G. Parkinson, Proc. of the Fifth International Alumina Quality Workshop (1999) p. 41.

[24] G. Lever, Light Metals (1978) p. 71.

[25] J.D. Guthrie, P.J. The and W.D. Imbrogno, Light Metals (1984) p. 127.

[26] P.J. The, Light Metals (1980) p. 119.

[27] A. Alamdari, J.A. Raper and M.S. Wainwright, Light Metals (1993) p. 143.

[28] P.G. Smith, H.R. Watling and P. Crew, Colloids and Surf. A 111 (1996) p. 119.

[29] M. Lee, F. Lincoln, G. Parkinson and P. Smith, Proc. of the Fourth International Alumina Quality Workshop (1996).

[30] D.S. Rossiter, D. Ilievski, P.G. Smith and G.M. Parkinson, ICemE 74 (1996) p. 828.

[31] H.R. Watling, R. Townsend and J.S.C. Loh, IChemE (1999).

[32] A. Owen, H.R. Watling, W. van Bronswijk and Z.-S. Yu, ICemE (1999).

[33] I. Seyssiecq, S. Veesler, G. Pèpe and R. Boistelle, J. Cryst. Growth 196 (1999) p. 174.

[34] N. Brown, J. Cryst. Growth 87 (1988) p. 281.

[35] N. Brown, J. Cryst. Growth 92 (1988) p. 26.

[36] S. Veesler, S. Roure and R. Boistelle, J. Cryst. Growth 135 (1994) p. 505.

Chapter 2

The impact of twinning on the morphology of gibbsite crystals

C. Sweegers, W.J.P. van Enckevort, H. Meekes, P. Bennema,
I.D.K. Hiralal and A. Rijkeboer [1]

Abstract

Gibbsite, γ-Al(OH)$_3$, is an important technical product, used mostly as an intermediate in the production of aluminium. According to the literature, the morphology of natural and industrial gibbsite crystals is pseudohexagonal with $\{001\}$ basal, and $\{100\}$ and $\{110\}$ side faces. Laboratory experiments on the growth of gibbsite crystals from unseeded sodium aluminate / sodium hydroxide solutions result in crystals (and agglomerates) with various morphologies, such as lozenge-shaped plates, hexagonal plates, as well as prisms. Optical polarisation microscopy showed many of the crystals to be twinned. Three kinds of reflection twin, $\{110\}$, $\{001\}$ and $\{100\}$ as mirror and composition plane, were identified. In addition, [130] rotation twinning with $\{001\}$ as composition plane were found. The effect of various kinds of twinning on the growth morphology and growth kinetics of gibbsite crystals is studied.

---

[1] The work in this chapter has been published in *J. Cryst. Growth*, 1999, **197**, 244.

2.1 Introduction

An important step in the Bayer process is the crystallisation of gibbsite, γ-Al(OH)$_3$, from sodium aluminate / sodium hydroxide solutions. Gibbsite is subsequently calcined to alumina, the material from which aluminium is obtained by electrolysis. In an industrial crystalliser, gibbsite forms agglomerates, about 100 microns in size [1]. The agglomerates consist of small gibbsite crystals of different shapes and sizes, oriented in all directions. The industrial process conditions are chosen such as to yield a product of the desired size, purity and strength required for subsequent aluminium production.

Gibbsite has a monoclinic space group, P2$_1$/n, with a = 8.684 Å, b = 5.078 Å, c = 9.736 Å and β = 94.54°. There are eight Al(OH)$_3$ molecules per unit cell [2]. The structure of gibbsite is pseudohexagonal with the c-axis as the pseudohexagonal axis and consists of double layers (AB) of close packed OH$^-$ groups with Al^{3+} occupying two thirds of the octahedral interstices within the layers [1, 3]. The AB layers are stacked according to the sequence ...-ABBA-ABBA-... .

The morphology of natural gibbsite crystals is usually reported as pseudohexagonal plate-like with {001} basal, and {100} and {110} side faces. Furthermore, prismatic crystals and lamellar or stalactitic aggregates have been found [1, 3, 4]. Gibbsite produced in the Bayer process or synthesised in the laboratory also forms (agglomerates of) pseudohexagonal plates or prisms [5–7]. Sometimes, lozenge-shaped crystals have been observed, which side faces have been indexed as {110} [8]. The morphological importance (MI, [9]) of each face and the size of gibbsite crystals depend on the specific crystallisation conditions.

In natural gibbsite, twinning usually occurs on {001} and about the [130] rotation axis with {001} as the composition plane. Sometimes, twinning on {100} and {110} has been found [3, 10]. Unfortunately, the literature reports little about these twin possibilities, except for a very early report by Rose [11]. Twinning has also been observed in synthetic gibbsite [5, 12]. Scanning electron microscopy and optical microscopy studies have indicated the occurrence of repeated twinning with parallel twin boundaries (i.e. lamellar or polysynthetic twinning) perpendicular to the pseudohexagonal c-axis, related to faults in the stacking of the AB layers. Twin boundaries parallel to the pseudohexagonal c-axis emanating from the centre of a hexagonal crystal (cyclic sector twinning) have also been reported. In addition, dislocations and grain boundaries have been observed [5, 12]. Energy calculations of single crystalline and twinned structures of gibbsite have predicted the appearance of {001}, and less commonly {110} twinning, with in both cases reflection as well as composition plane [13].

Both natural and synthetic gibbsite crystals exhibit a large variation in their morphological appearance [5–7, 12]. The reason for this high diversity is still unclear. This chapter reports the results of laboratory experiments of the growth of gibbsite crystals from unseeded sodium aluminate / sodium hydroxide solutions. The morphology of the crystals obtained showed a high diversity and several kinds of twinning. We discuss in detail the twin possibilities of gibbsite and especially the effect of twinning on the morphology of these crystals for varied growth conditions. This leads to the main conclusion that the basic morphology of gibbsite is lozenge-shaped and that large hexagons only appear if twinning occurs.

2.2 Experimental

The gibbsite crystals were grown from pure sodium aluminate / sodium hydroxide solutions. These solutions were prepared by dissolving pure aluminium metal (purity 99.999%) in 6M sodium hydroxide solutions at 90-100°C. This was done in teflon vessels instead of stainless steel ones, to prevent leaching of ions from the stainless steel. The freshly prepared solutions were slightly cooled and subsequently filtered through a Millipore HVLP filter (0.45 μm) to remove any undissolved aluminium and dust particles. The filtered solutions were then poured into teflon vessels, which were closed and placed in a thermostated bath, which maintained a constant temperature of 80°C. No seed crystals were used in the experiments; nucleation was allowed to take place spontaneously. The experiments were continued for 24 h, while stirring.

The relative supersaturation, σ, of the solution was determined from the difference between the initial gibbsite concentration, c, of the solution, and the equilibrium concentration, c_{eq}, at the crystallisation temperature:

$$\sigma = \frac{c - c_{eq}}{c_{eq}}. \tag{2.1}$$

The equilibrium concentration, c_{eq}, was calculated by using an equation derived by McCoy et al. [14], relating the equilibrium solubility of gibbsite to the temperature, caustic concentration and impurity concentrations of sodium aluminate liquors. For the experiments carried out during the present investigation, the initial supersaturations of the aluminium hydroxide solutions were comparable to those used under industrial plant conditions, namely from 0.21 ± 0.01 to 0.45 ± 0.01.

After 24 hours, the solutions were filtered (Millipore HVLP, 0.45 μm) to collect the crystallised solid particles. The small crystals and agglomerates were washed with warm, deionised water to remove the solvent adhered to the surface of the crystals. Finally, the crystalline material was dried at room temperature for several days.

Regular checks with X-ray powder diffraction were done to establish whether gibbsite was formed. The crystals were examined with optical transmission polarisation microscopy, reflection differential interference contrast microscopy (DICM) and scanning electron microscopy (SEM).

2.3 Results and Discussion

In each batch, gibbsite crystals appeared in a large variety of morphologies. The gibbsite crystals were isolated or incorporated into agglomerates. The morphology of the gibbsite crystals obtained can be classified into three categories: plate-like lozenges, plate-like hexagons and prisms (rods). Several examples of the crystal morphologies observed are shown in figure 2.1. X-ray powder diffraction showed that the material obtained was purely gibbsite, free of other $Al(OH)_3$ phases.

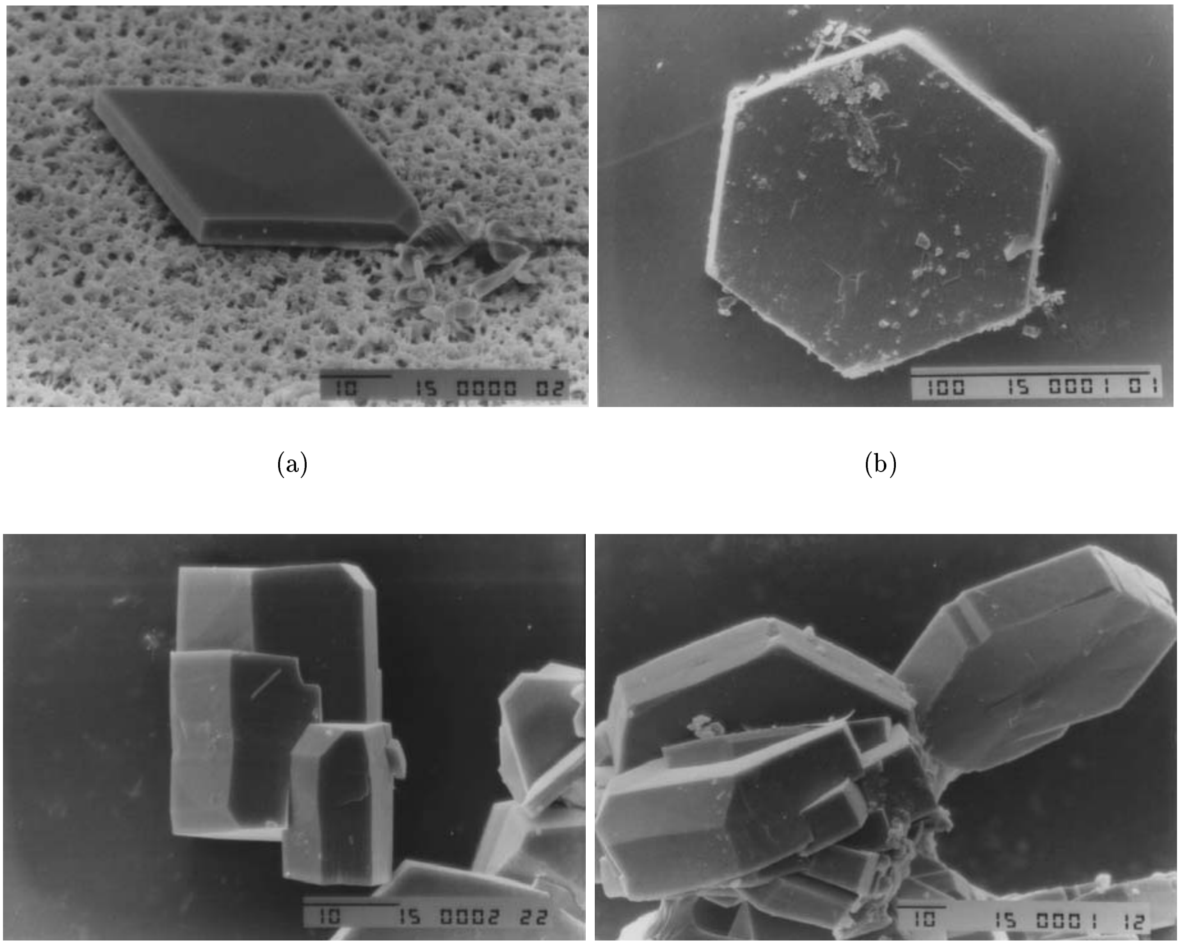

(a) (b)

(c) (d)

Figure 2.1: SEM micrographs showing examples of gibbsite crystal morphologies, with (a) lozenge, (b) hexagon, (c) prisms and (d) agglomerate. The length of the scale bars in the insets is in microns.

From solutions of low supersaturation ($\sigma = 0.21 \pm 0.01$), crystallisation mainly resulted in small plate-like lozenges and in prismatic crystals. The lozenges were 30 to 50 microns in size and only a few microns thick. The prisms were roughly 2-5 microns wide and 10-15 microns thick; the aspect ratio ranged from 2 to 7. The prisms had either a (truncated) lozenge-based or a hexagonal-based morphology. Sometimes, elongated prisms (aspect ratio up to ten) were observed. The ratio of lozenges and prisms varied in several experiments, but was roughly $\frac{1}{3}$.

Increasing the supersaturation ($\sigma = 0.34 \pm 0.01$ to 0.45 ± 0.01) led to large hexagonal plate-like crystals. The hexagons were 100 to 200 microns in size and about 10 microns thick. The relative number of hexagonal plates increased for higher supersaturations, at the expense of lozenges and prisms, while also more agglomerates were present. Half of the crystals was hexagonal shaped for solutions of medium supersaturation (0.34 ± 0.01).

The other half were lozenges and prisms. For the highest supersaturation (0.45 ± 0.01), mainly hexagons and a few lozenges and prisms were present.

In addition to the lozenge- and hexagon-based morphology, other kinds of crystal shapes were observed in solutions of both low and high supersaturation. These crystals deviated to some extent from the perfect lozenge or hexagonally shaped crystals.

Several kinds of twinning were observed in gibbsite crystals, using SEM and polarisation microscopy. The following sections discuss in detail the three categories of morphology of gibbsite and try to explain their relative occurrences in terms of single and multiple twinning and growth kinetics.

2.3.1 Lozenges

Optical polarisation microscopy showed that the lozenge-shaped crystals were single crystalline. They all had straight side faces (figure 2.2a), and the angles between the intersecting lines of these faces were $60° \pm 1°$ and $120° \pm 1°$, as shown in figure 2.2b. Observations with SEM showed that the side faces were perpendicular to the top face, to within a few degrees. The faces were indexed as {001} basal and {110} side faces, which was confirmed with polarisation microscopy. The {110} faces of lozenge-shaped crystals have also been observed in a study on the morphology of lozenges, using transmission electron microscopy [8]. Other faces, indexed as {100}, {101} and {112}, were sometimes observed and their occurrence was probably dependent on the local growth conditions. From the shapes of the lozenges, it is concluded that the morphological importance of the faces decreases with: $\mathrm{MI}_{\{001\}} \gg \mathrm{MI}_{\{110\}} > \mathrm{MI}_{\{100\}} > \mathrm{MI}_{\{101\}} \approx \mathrm{MI}_{\{112\}}$.

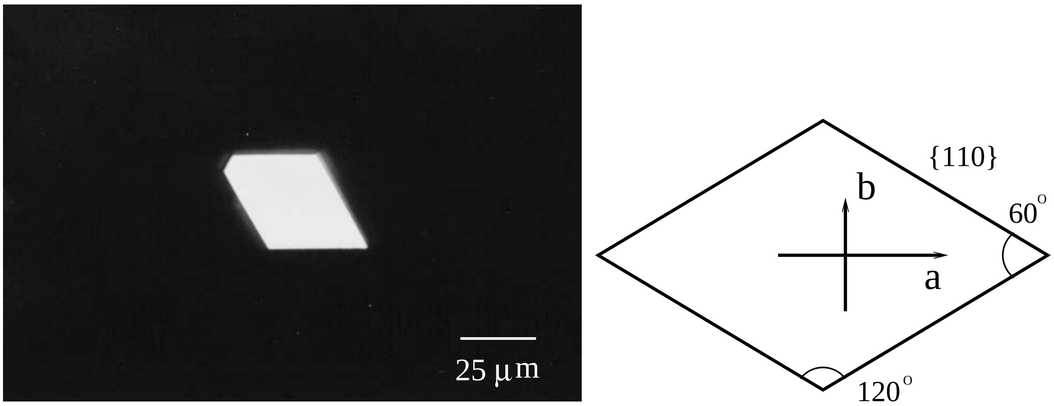

(a) (b)

Figure 2.2: (a) Lozenge-shaped morphology of gibbsite, showing a small {100} face, (b) orientation of crystallographic axes ***a*** and ***b*** determined with polarisation microscopy.

2.3.2 Hexagons

On increasing the supersaturation, hexagonal plate-like crystals were formed, as is shown in figure 2.1b. The hexagonal crystals were relatively large (100 to 200 microns and 10 microns thick) compared to the lozenges. The angles between the intersecting lines of the side faces were about 120°.

Analysing the hexagons with polarisation microscopy revealed that the crystals were not single crystalline, but were built up of six domains. A polarisation micrograph of such a crystal is presented in figure 2.3a. These cyclic sector twins have earlier been observed by Gnyra et al. [5] and by Armstrong et al. [12]. Under crossed polarisers, two opposite crystal domains were always in extinction simultaneously. The three pairs of opposite domains were in extinction in three successive 60° directions. The orientation of the crystallographic axes in each crystal domain was determined by analysing the extinction direction of that domain. The extinction directions indicated that in each crystal domain either the *a*- or the *b*-axis is perpendicular to the side face (assuming that $\boldsymbol{c}$ is perpendicular to the top and bottom face).

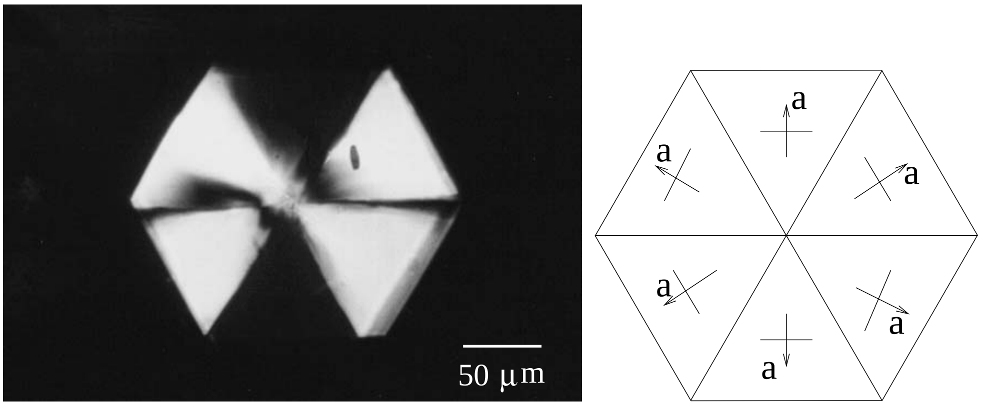

(a) (b)

Figure 2.3: (a) Polarisation micrograph of a sixfold twinned hexagon. Two opposite crystal domains are in extinction in three successive 60° orientations. (b) Orientation of $\boldsymbol{a}$ and $\boldsymbol{b}$ in the six crystal domains.

In the present study, the twin boundaries seemed to be parallel to the {110} planes and the six side faces were indexed as {100}. This follows from the triangular twin domains and the optical extinction for polarisers parallel to the bisector of the central angle. Focusing through the crystal with an optical microscope showed that the boundary between two adjacent domains was within 2-3° perpendicular to the {001} top and bottom faces.

As was observed for the lozenge-shaped crystals, more side faces sometimes appeared on the twinned hexagons. These side faces had angles of 135° ± 2° with respect to the top face, corresponding to {101} faces.

Optical microscopy (DICM) showed that the {001} faces of the domains in the sixfold twinned hexagons were ordered either in a convex or in a concave arrangement. This suggests that the six domains of the sixfold twinned hexagon have a common *c*-axis, as $\beta = 94.54°$. The angle between two opposite domain faces is expected to be (180 - 2x4.54)°. However, a slightly different angle of $165° \pm 1°$ was mostly measured. A possible explanation for this deviation is the occurrence of growth steps emanating from sources at the centre of the hexagon.

Some surfaces were quite irregular, as is shown in figure 2.4. A characteristic feature is found by the steps which seem to change their growth direction on passing a twin plane. Further, isolated shallow growth hillocks and high growth steps originating from grain boundaries and twin boundaries were seen. A detailed study of the surface morphology of gibbsite crystals using atomic force microscopy is described in chapter 3.

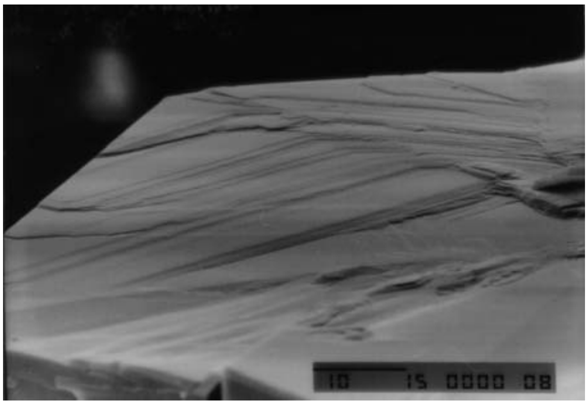

Figure 2.4: SEM micrograph of a {001} surface of a sixfold twinned hexagon. Steps change their growth direction on passing a twin boundary. The length of the scale bar is 10 microns.

Each twinned hexagon had a highly strained centre, judging from polarisation microscopy images showing stress birefringence. The appearance of six regular triangular domains touching each other at the centre of the crystal suggests that twinning already occur at the initial stage of nucleation, introducing a lot of stress. It is possible that twinning is induced by a rearrangement of molecules in a highly strained nucleus, which does not necessarily have the same composition or phase as gibbsite. It nucleate as hexagonal and transfer at a certain size to the monoclinic form.

Thus, it seems that the adjacent twin domains are related to each other by a reflection symmetry element in {110}, as mirror and composition plane. This is not exactly correct. The angle between the (110) and $(1\bar{1}0)$ face of a crystal domain, i.e. the two twin planes of one domain, is 60.6° calculated from lattice parameters. Six of such domains constructed into a sixfold twinned hexagon do not fit perfectly. The boundary between two domains will be filled with extra dislocations, resulting in a tilted twin boundary. The stress in these regions can indeed clearly be seen by stress birefringence in the optical micrograph of figure 2.3.

In addition to the sixfold twinned hexagons, some single twinned hexagons were observed. The twin boundary traversed the crystal between two opposite corners and the hexagon was elongated along this direction. The extinction directions of the two domains were plus and minus 30° with respect to the orientation of the twin boundary. The appearance of these crystals can be explained by a single twin on {110}. In a single {110} twinned hexagon, four adjacent faces are {110} faces, while the remaining two are {100} faces. This is schematically represented in figure 2.5. This crystal will develop through a combination of relatively fast growing {100} faces and a re-entrant corner mechanism between two pairs of adjacent {110} faces. These two pairs of {110} faces will disappear, resulting in a hexagon elongated along the twin plane.

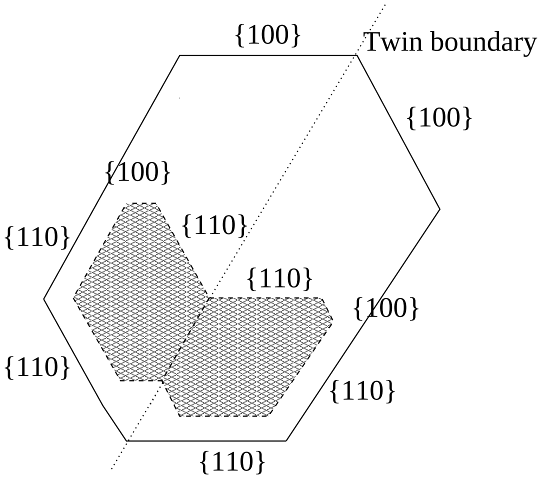

Figure 2.5: Schematic representation of crystal single twinned on {110}.

From the appearance of the lozenge-shaped crystals, it was already concluded that the {100} faces grows faster than the {110} faces. This suggests that upon further growth the sixfold twinned crystal will form a star-like crystal bounded by {110} faces. As yet, these crystal forms were only occasionally observed. In many cases, however, re-entrant corners were observed at the outcrops of the twin planes at the side faces, which can be considered as the initial stage for the formation of a star pattern. An explanation for the absence of star-like crystals is the presence of these re-entrant corners, induced by twinning, which serve as step sources for the growth of each set of two adjacent {110} faces. The combination of relatively fast growing {100} side faces and even faster step-sources at the re-entrant corners results in large plate-like hexagons up to 200 microns.

The thickness of the hexagons can be explained by the presence of dislocations and tilted twin boundaries at the {001} surfaces. These serve as nucleation points for step growth on the {001} surface, resulting in crystals with a thickness up to 15 microns. The presence of these defects introduces extended patterns of lower and higher steps on the surfaces as imaged by atomic force microscopy (chapter 3).

2.3.3 Prisms

Besides small plate-like lozenges and large plate-like sixfold twinned hexagons, prismatic crystals were simultaneously grown for especially low supersaturations. The prisms had roughly the same height as the sixfold twinned hexagons, 10-15 microns, but were much smaller in lateral size, only 5-7 microns. The prisms showed a large variation in appearance. They exhibited a lozenge-based or a hexagon-based morphology. Judging from the morphology of the prismatic crystals and the angles between adjacent faces, it was concluded that the top and bottom faces were $\{001\}$ and the side faces were $\{110\}$ and/or $\{100\}$. Further observations, using SEM, revealed that some prisms were tapered or inclined. Some other prisms consisted of two prisms stacked on top of each other, rotated over a few degrees. Sometimes more side faces, $\{101\}$ or $\{112\}$, appeared on the prisms.

Single crystalline prisms

The prisms lying on a side face were examined with polarisation microscopy. Only some of the prism were single crystalline. Most of these single crystalline prisms were in extinction if their extinction direction was rotated over 20° with respect to $\boldsymbol{c}$. This indicates that $\boldsymbol{b}$ is not oriented in the plane of the polarisers and, thus, the prisms were lying on a $\{110\}$ side face. In some cases, these prisms were in extinction when $\boldsymbol{c}$ was parallel to the direction of one of the crossed polarisers. This latter extinction direction parallel to $\boldsymbol{c}$ is in accordance with crystals lying on one of the $\{100\}$ side faces. Because most of the prisms had an extinction direction of 20°, the single crystalline prisms must have relatively large $\{110\}$ faces compared to the $\{100\}$ faces.

Twinning "parallel to $\boldsymbol{c}$"

SEM observations showed that many prism were twinned with their twin boundaries parallel to the c-axis. This is reflected in the convex and concave shapes of the top faces. As deduced from the number of linear twin boundary outcrops at these top faces, both single and multiple cyclic twinning occur. Hexagonal prisms with a sixfold cyclical inclined top face reflected sixfold twinned crystals. They correspond to the hexagons, twinned sixfold on $\{110\}$ as mirror and composition plane. Another kind of twinning was frequently found in prisms bounded by only $\{110\}$ faces. Binary inclined $\{001\}$ top faces were observed, as is shown in figure 2.6a. The twin boundary outcrop at the top face is parallel to the line connecting the two opposite 120° corners of an ideal lozenge. In combination with the observation that the twin boundary runs parallel to the c-axis, this suggests that such lozenge-based prisms are twinned on the $\{100\}$ mirror and composition plane.

Twinning with the twin boundaries parallel to $\boldsymbol{c}$ was supported by observations with polarisation microscopy with different extinction directions for different crystal domains. The extinction directions of the two crystal domains were mostly plus and minus 20° relative to $\boldsymbol{c}$. This indicates that crystal domains were formed by $\{100\}$ twinning. Twinning parallel to $\boldsymbol{c}$ can not be observed when the prisms lie on a $\{100\}$ face, as the 2D intersections of the indicatrices with $\{100\}$ are then the same in both crystal domains and thus

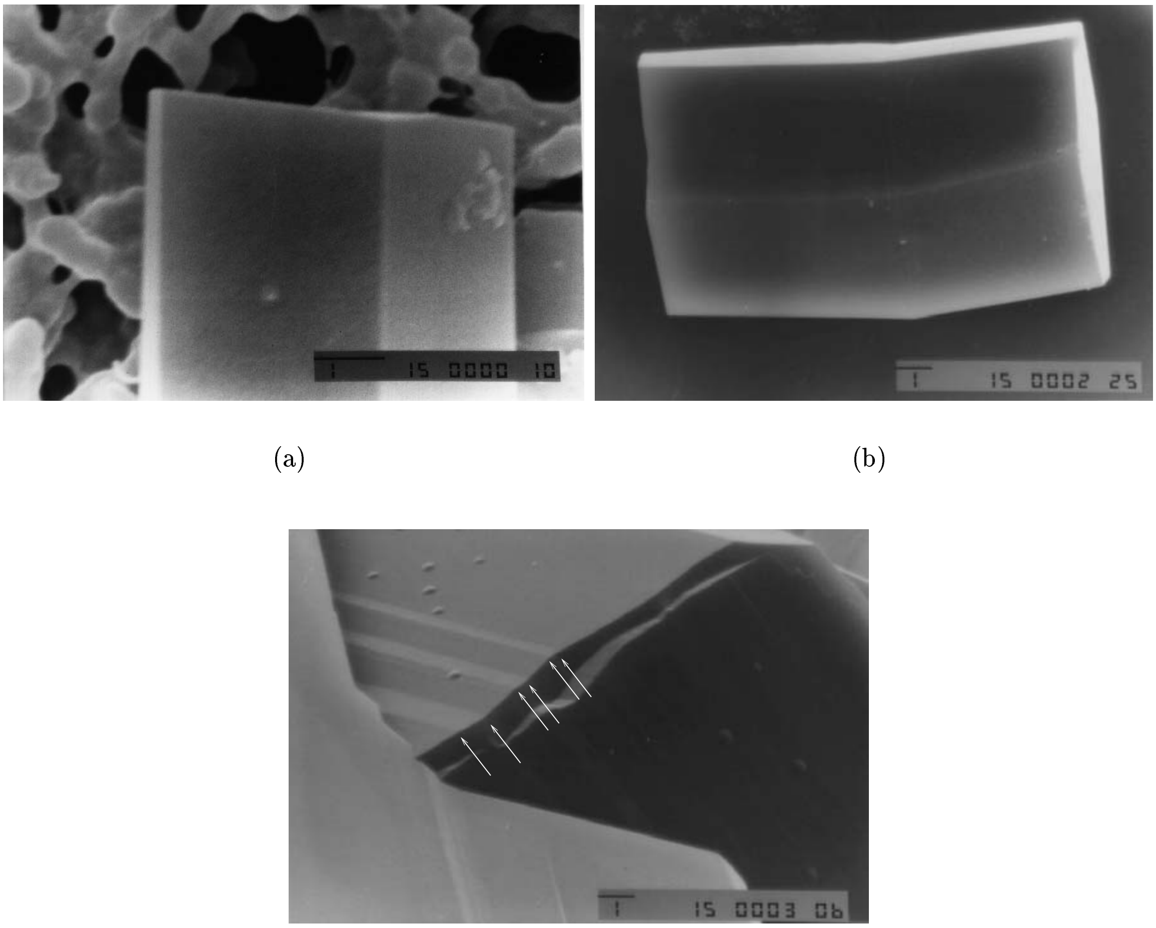

(a) (b)

(c)

Figure 2.6: (a) SEM picture of a prism with inclined {001} surface. The prism is twinned parallel to $\boldsymbol{c}$. (b) SEM photograph of prism with an inclined side face, due to twinning perpendicular to $\boldsymbol{c}$. (c) SEM picture of a polysynthetically twinned prism, as part of an agglomerate. The length of the scale bars is 1 micron.

have the same extinction direction. Unfortunately, it was not possible to examine the small prismatic crystals parallel to the crystallographic c-axis to determine all possible twin planes.

Twinning "perpendicular to $\boldsymbol{c}$"

Figure 2.6b shows a SEM micrograph of a prism inclined along $\boldsymbol{c}$. The two components of the prism are mirror symmetric with respect to the common {001} boundary. The angle between the adjacent {100} side faces of the twin components is 170° ± 1°, which can easily be explained by the occurrence of mirror twinning on {001}, as $\beta = 94.54°$. Here, the twin intergrowths consist of twin domains with the twin boundaries perpendicular to the pseudohexagonal c-axis. Other angles than 170° were measured for prisms situated on a plane other than the [010] direction or for prisms twinned in [130] with {001} as the composition plane. In many cases, repeated twinning with parallel {001} twin boundaries was observed. This is known as polysynthetic twinning. The parallel twin lamellae of crystalline material with reversed crystallographic orientation led to prism side faces with many inclinations. An example is shown in figure 2.6c.

The presence of different crystal domains, caused by {001} twinning, was also observed with polarisation microscopy. The two crystal domains showed different extinction orientations, mostly plus and minus 20° relative to $\boldsymbol{c}$. Other extinction directions, e.g. 0° and 20°, were also observed, reflecting twinning on [130] as rotation axis with {001} as composition plane. In this case, $\boldsymbol{b}$ is oriented parallel to one of the polarisers in only one of the two crystal domains.

The presence of {001} mirror twinning could not always be established using crossed polars. If a {001} twinned prism is oriented with its {100} face perpendicular to the optical axis of the microscope, then the separate domains have the same extinction direction. This also occurs if prisms, or lozenges or hexagons, are viewed from the {001} top faces. Therefore, the occurrence of {001} twins in the lozenges and hexagonal plates could not be observed with polarisation microscopy, when viewed along [001].

Interesting are the prisms with a {101} face half-way the crystal. Polarisation microscopy showed that these crystals consist of two crystal domains. The boundary between the domains is parallel to the basal face at the position of the top of the extra {101} face, half-way of the crystal. It seems that the two crystal domains do not fit perfectly. This might account for the presence of the {101} face.

Appearance of prisms

In the literature, it has been suggested that the crystallisation of gibbsite from alkali hydroxide solutions is caused by the presence of alkali atoms. Without the presence of alkali atoms, bayerite would be formed instead of gibbsite. Furthermore, the growth of gibbsite parallel to $\boldsymbol{c}$ would be induced by potassium atoms in the crystal lattice [8, 15]. The larger volume of K^+ ions would afford stronger bonding between the molecular layers and thus stimulate growth parallel to the c-axis of gibbsite [15]. This effect would be even larger for cesium atoms [8]. Prismatic crystals have also been found when gibbsite was grown from NaOH solutions of low supersaturation and high temperature [1]. No reason for this preferable growth parallel to $\boldsymbol{c}$ has been given. It is possible, however, that the formation of prismatic crystals is not so much caused by stimulation of growth parallel to the c-axis by alkali atoms as has been suggested by others, but rather by hampering of growth of the side faces, since their lateral size is considerably smaller than that of the lozenges and hexagons grown simultaneously during our experiments. An explanation for this suggestion will be given below.

Many prisms were, apart from twinning on {001}, single twinned on {100} and single or multiple twinned on {110}. This twinning generated many defects at the {001} surface, which induced growth parallel to $\boldsymbol{c}$. This resulted in crystals which were as thick as the hexagons. The lateral size of the prisms was much smaller than those of the lozenges and hexagons, which must be due to a relatively low lateral growth rate. In contrast with twinning parallel to $\boldsymbol{c}$, twinning perpendicular to $\boldsymbol{c}$ did not stimulate growth in the lateral direction. The growth of the side faces was probably inhibited by impurities. It is well-known that a few ppm of impurities can already block crystal growth [16]. The impurities thus seem to adsorb preferentially on the side faces and less on the basal {001} faces. This is in contrast to previous studies, which suggested that the {001} face is the preferred face of gibbsite crystals for adsorption of impurities [17]. The presence of impurities can also explain the formation of tapered crystals, because step propagation on the side faces is blocked in a similar way as was reported for the tapered crystals of {100} faces of KH_2PO_4 [18]. This blocking effect did not occur for solutions of high supersaturations. The driving force for growth was probably stronger than the blocking by impurities [16].

2.3.4 Discussion

It is clear that various kinds of twinning can occur in gibbsite crystals. The possibilities are single or combinations of reflection twins with {001}, {110} or {100} as mirror and composition plane, and also [130] as rotation twin axis with {001} as composition plane. This leads to a wide range of different morphologies. On the basis of energy calculations, Fleming et al. [13] already predicted some of the twin possibilities of gibbsite, namely {001} as a common twin reflection and composition plane and {110} as a rare twin plane (reflection and composition). In our experiments, these two twin possibilities were indeed observed.

Analysing the monoclinic structure of gibbsite, it is clear that a {001} mirror twin can easily be formed because of the structural similarity of the {001} and $\{00\bar{1}\}$ surfaces. The {001} mirror plane is apparently located between an AB and a BA layer in the stacking of the AB layers. This additional plane replaces the pseudo mirror plane already present in the structure, causing the -ABBA-ABBA- stacking sequence of the AB layers. This original plane is pseudo, because the AB layers are displaced in one direction (a-axis), since $\beta = 94.54°$. Therefore, twinning on the mirror plane {001} only needs reconfiguration of the hydrogen positions in such a way that β changes from 94.54° to 85.46°.
The [130] rotation twin operation with {001} as the composition plane corresponds to a rotation over 60° along $\boldsymbol{c}$ of one crystal domain relative to the other, which is quite feasible in the pseudohexagonal gibbsite structure.
The mirror twin on {110} can also easily be formed as a result of the pseudohexagonal symmetry of the crystal lattice. Only a small distortion of the atomic positions is sufficient to fit the two crystal domains. This {110} twin corresponds to the pseudohexagonal 6_3 symmetry operation.
Twinning on {100} requires repositioning of the aluminium atoms in the octahedral interstices. This suggests that this twin type is less probable than the possibilities mentioned before.

Twinning was found in gibbsite crystals grown from solutions of relatively low as well as high supersaturations. The number of sixfold twinned hexagons increased with increasing supersaturation. It is well-known that the nucleation of twinned crystals increases when the degree of supersaturation increases [19]. However, from our experiments it was not clear whether the amount or kind of twinning was dependent on the supersaturation. It is more likely that at higher supersaturations, the growth of the side faces is not inhibited by the adsorption of impurities. For lower supersaturation, many crystals sixfold twinned on $\{110\}$ remained prismatic, probably due to impurity blocking of the side faces. Moreover, the twin boundaries are better defined for higher supersaturations: it is possible that impurities influence the perfection of the boundaries.

The lozenges were single crystalline, which suggests that this is the basic morphology of gibbsite. The lozenge-shaped morphology with additional $\{100\}$ faces is in accordance with the commonly reported pseudohexagonal morphology of gibbsite. However, the absence or small size of the $\{100\}$ faces indicates that these faces grows faster than the $\{110\}$ faces. The difference in growth rate between the $\{110\}$ and the $\{100\}$ faces may be caused by the difference in attachment energy of the faces, or by the difference in blocking by sodium ions or other impurities present in the solution. In contrast, Lee et al. [8] have suggested that single crystalline lozenges are formed due to the incorporation of sodium atoms at a higher level compared to hexagonally shaped single crystals. They also indexed the side faces of small hexagonal gibbsite crystals as $\{110\}$ and $\{100\}$, using transmission electron microscopy. However, it is concluded from the present study that the $\{100\}$ faces only appear at locally lower supersaturation or perhaps through blocking of these faces by sodium or other impurities and that the lozenges exhibit the basic morphology.

2.4 Conclusions

The present experimental results show that gibbsite crystals grown from sodium hydroxide / sodium aluminate solutions occur in a large variety of shapes and sizes. It is concluded that lozenge-shaped crystals exhibit the basic morphology of gibbsite. The appearance of $\{100\}$, $\{101\}$ and $\{112\}$ depends on the crystallisation conditions. The occurrence of the various faces suggests that the MI decreases with $\mathrm{MI}_{\{001\}} \gg \mathrm{MI}_{\{110\}} > \mathrm{MI}_{\{100\}} > \mathrm{MI}_{\{101\}} \approx \mathrm{MI}_{\{112\}}$. Single or multiple twinning, dislocations and the presence of impurities lead to the formation of other crystal shapes: large hexagonal plates and prisms. The plate-like hexagonal crystals are only formed when single or multiple twinning occurs on the $\{110\}$ plane at the initial stage of nucleation. Most of the hexagonal platelets are twinned sixfold on $\{110\}$, with $\{001\}$ as the basal faces and $\{100\}$ as side faces. The combination of fast growing $\{100\}$ faces and re-entrant corners results in large sizes up to 200 microns. Steps generated from dislocations and twin boundaries cause a somewhat enlarged growth rate parallel to $\boldsymbol{c}$. It is suggested that small prismatic crystals are formed if the lateral growth of twinned crystals is inhibited by impurities. This blocking effect is overcome at high supersaturation; the number of small prisms is largely reduced by forming large hexagonal plates. Our conclusion is thus not in accordance with the usual assumption reported in the literature that the hexagonal gibbsite crystals consist of $\{110\}$ and $\{100\}$ side faces.

Many different crystal morphologies are induced by twinning, growth imperfections and impurity blocking. It is fascinating that crystals with different morphologies grew simultaneously in the same batch. Depending on the supersaturation, a difference in the relative number of the lozenges, prisms and hexagons was found. The occurrence of twinning has a large influence on the morphology of the crystals and makes it difficult to investigate the growth kinetics of gibbsite crystals under industrial plant conditions. *In-situ* observations with optical microscopy of growing gibbsite crystals is the best approach to study the growth properties of individual crystal faces. This work is described in chapter 4.

References

[1] K. Wefers and C. Misra, Oxides and Hydroxides of Aluminium, Technical Report Technical Paper no. 19, revised Alcoa Research Laboratories, Pittsburgh, Pennsylvania (1987).

[2] H. Saalfeld and M. Wedde, Z. für Kristall. 139 (1974) p. 129.

[3] W.A. Deer, R.A. Howie and J. Zussman, An Introduction to Rock Forming Minerals (Longman Scientific & Technical, 1992) 2^{nd} edition.

[4] K. Frye, The Encyclopedia of Mineralogy (Hutchinson Ross Publishing Company, Pensylvania, 1981) 16^{th} edition.

[5] B. Gnyra, R.F. Jooste and N. Brown, J. Cryst. Growth 21 (1974) p. 141.

[6] C. Misra and E.T. White, J. Cryst. Growth 8 (1971) p. 172.

[7] N. Brown, J. Cryst. Growth 12 (1972) p. 39.

[8] M.-Y. Lee, A.L. Rohl, J.D. Gale, G.M. Parkinson and F.L. Lincoln, IChemE 74 (1996) p. 739.

[9] P. Bennema and J.P. van der Eerden, Morphology of Crystals (Terra Scientific Publishing Company, 1987).

[10] W.L. Roberts, G.R. Rapp jr. and J. Weber, Encyclopedia of minerals (Van Nostrand Reinhold Company, New York, 1974).

[11] G. Rose, Z. für Krystallographie und Mineralogie 16 (1890) p. 16.

[12] L. Armstrong, J. Hunter, N. Calos, G. Miller, P. Uwins and J. Barry, Proc. of the Fourth International Alumina Quality Workshop (1996) p. 239.

[13] S.D. Fleming, G.M. Parkinson and A.L. Rohl, J. Cryst. Growth 178 (1997) p. 402.

[14] B.N. McCoy and J.L. Dewey, Light Metals (1982) p. 173.

[15] K. Wefers, Naturwissenschaften 49 (1962) p. 204.

[16] W.J.P. van Enckevort and A.C.J.F. van den Berg, J. Cryst. Growth 183 (1998) p. 441.

[17] N. Brown, J. Cryst. Growth 16 (1972) p. 163.

[18] B. Dam, P. Bennema and W.J.P. van Enckevort, J. Cryst. Growth 74 (1986) p. 118.

[19] R. Kern, Bull. Soc. Franç. Minér. Crist. 84 (1961) p. 292.

Chapter 3

Surface topography of gibbsite crystals grown from aqueous sodium aluminate solutions

C. Sweegers, M. Plomp, H.C. de Coninck, H. Meekes, W.J.P. van Enckevort, I.D.K. Hiralal and A. Rijkeboer [1]

Abstract

Optical, scanning electron and atomic force microscopy were used to examine the surface topography of gibbsite (γ-Al(OH)$_3$) crystals grown from supersaturated caustic soda solutions. Several growth phenomena like monomolecular and higher steps, growth hillocks, contact nucleation and planar faults were observed. It turned out that the growth features observed are related to the different gibbsite crystal morphologies found. Single crystalline lozenges of a few μm thickness have hillocks on the basal {001} faces related to one or a few dislocations. For ultra thin lozenges (few tens of nm and an aspect ratio larger than 1000) no dislocation sources emerging the {001} surface were found; their surface morphology is flawless. The second type of crystals, sixfold twinned hexagons, has irregular {001} surfaces as a result of many defects. The introduction of defects leads to enhanced growth parallel to $\boldsymbol{c}$. Lateral expansion proceeds by a 2D nucleation of the fast growing {100} side faces and the enhanced 2D nucleation at the reentrant corners at the outcrops of twin planes. Crystals of the third major crystal morphology found, i.e. prisms, also exhibit many defects. Mosaicity was observed and related to the presence of misaligned crystallites or impurities. These results indicate that gibbsite crystals free from dislocations grow slowly along the crystallographic $\boldsymbol{c}$ direction and mainly expand laterally, probably by a 2D nucleation mechanism, resulting in an ultra thin lozenge-shaped morphology. The growth of other gibbsite morphologies is predominantly a consequence of the formation of defects. The fact that the prismatic crystals do not show a pronounced lateral growth as the hexagons do, suggests that besides step growth induced by defects also other mechanisms influence gibbsite crystal growth.

---

[1] The work in this chapter has been submitted to *J. Cryst. Growth.*

3.1 Introduction

The crystallisation of gibbsite, γ-Al(OH)$_3$, from Bayer liquors as applied in the aluminium industry has been widely studied in the last few decades. Most of the previous work considered crystallisation kinetics and agglomeration using batch crystallisers and was especially focused on the influence of the most important parameters - like caustic concentration, supersaturation, seeds and impurities - on the crystallisation rate [1–16]. Only a few studies reported on surface topography and its relation to the growth mechanism of gibbsite [17–22]. The investigation of the surface structure is of high interest, because most crystallisation processes such as growth and secondary nucleation take place at the surface.

Already starting from 1959, optical and scanning electron microscopy (SEM) were used to examine the polycrystallinity of gibbsite [17–19]. It was concluded that twinning, coherent internal boundaries (created by internal forces due to imperfect twinning) and plate-like branches lead to the polycrystallinity of gibbsite crystals under industrial growth conditions. It was suggested that the formation of plate-like branches on the {001} basal plane in particular is the result of surface nuclei poorly oriented by dislocations in the underlying crystal. The initial orientation imposed by these defects determine the preferred orientation of the subsequently growing crystal. Many crystals grew out to agglomerates in this way.

In 1972, Brown [20] examined the changes in surface topography of gibbsite crystals during crystallisation using SEM. At high supersaturations of 150%, the basal surfaces of gibbsite showed a wave-like pattern, which was interpreted as terraces or steps growing over the surface. Only a few straight steps were observed. As crystal growth continued, the supersaturation decreased and surface irregularities were smoothed out. At low supersaturation (25%), the crystallisation rate became negligibly small. They concluded that the crystal growth of gibbsite under Bayer process conditions occurs by a surface nucleation mechanism with little or no contribution from screw dislocations.

In 1997, Addai-Mensah [23] reported the occurrence of a poorly-formed crystalline material on the surfaces of gibbsite, which was collected at the early stage of unseeded crystallisation experiments using pure Bayer liquors. The crystalline surface layer turned out to be Al(OH)$_3$ and was suggested to be bayerite.

Recently, Lloyd et al. [21] used *ex-situ* atomic force microscopy (AFM) to image the surface of gibbsite crystals. Most surfaces of the crystals were covered with small {001} plates tilted at an angle with respect to the underlying basal face. The surfaces of these plates were rough. The author suggested that growth of gibbsite is related to a mechanism dominated by the spreading of these layers.

AFM studies by Freij et al. [22] showed the presence of various defects on the basal face of gibbsite which might influence the crystal growth processes. At low supersaturation growth occurred by step growth from polygonal growth hillocks. At high supersaturation, circular nuclei were observed, developing into elongated features which coalesced to form a smooth surface. The authors suggested a continuous birth and spread mechanism. Under the same experimental conditions also step growth from a growth hillock was observed.

In chapter 2, using optical and electron microscopy, we have distinguished three main types of gibbsite crystals, namely (1) large plate-like hexagons, (2) lozenges and (3) prisms (rod-shaped crystals). Polarisation microscopy showed that the large hexagons are sixfold twinned in {110}, while the lozenges are single crystalline. The prisms showed various forms of twinning. Besides these three main categories, other shapes of gibbsite crystals were observed in batches grown from similar Bayer liquors. Examples are truncated lozenges and block-shaped crystals, intermediate between plates and prisms. It is to be expected that the different morphologies of gibbsite crystals are related to different growth mechanisms. A detailed investigation of the crystal surface topography can give more information about the growth properties of these various morphologies.

In this chapter, the results of *ex-situ* microscopic studies of the surface structure of gibbsite crystals in relation to their defect structure are reported. In particular, attention is focused on the differences between the three main morphologies of gibbsite. The investigations have revealed many defects that determine the variety of growth morphologies of gibbsite crystals to a large extent.

3.2 Experimental

Gibbsite crystals used for investigating the surface topography were nucleated and grown from pure aqueous sodium aluminate - sodium hydroxide liquors, referred to as Bayer liquors. The solutions were prepared as described in chapter 2. The Bayer liquors used are composed of 6M and 4M NaOH with a relative gibbsite supersaturation of 0.63 and 0.67, respectively [24]. The liquor composition corresponds in the North American industries terminology to a sodium or caustic concentration of C = 300 and 200 g/l Na_2CO_3 and an alumina to caustic concentration ratio, A/C = 0.8 and 0.65 (g/l Al_2O_3 / g/l Na_2CO_3), respectively. The liquors were poured in teflon vessels, placed in a thermostatic bath of 80°C under gentle stirring conditions and allowed to crystallise during 24h.

Special attention was paid to the collection of the crystallised particles from the solution in such a way that artifacts formed during separation from the solution were minimal. In case of a shut-off effect, the nature and extent of the changes to the surface morphology will obscure information about the actual growth processes. Therefore, prior to collection the solutions were diluted with sodium hydroxide solution of volume, concentration and temperature identical to the original Bayer liquors. This stopped the growth process. Subsequently, the solutions were filtered through a Millipore HVLP filter (45 μm) and washed with hot de-ionised water.

As will be described in the next section, gibbsite crystals with a large variety in habit and size were obtained, even in a single experiment. The crystals were regularly checked with X-ray powder diffraction and Raman spectroscopy to verify whether gibbsite was formed and not one of the other aluminium (oxide) hydroxide polymorphs. The bulk analysis with XPD as well as analysis of individual crystals with Raman identified gibbsite as the only polymorph.

Single crystals differing in morphology and size were collected on sample holders. The crystal surface topography was examined with differential interference contrast microscopy (DICM), scanning electron microscopy (SEM, Jeol T-300 and High Resolution Jeol 600F) and atomic force microscopy (AFM, Topometrix TMX 2000 and Digital Instruments Dimension 3100). The AFMs operated in contact mode using silicon nitride cantilevers. The crystals selected for AFM studies had relatively smooth surfaces as imaged by DICM, to minimise any scan problems. The defect structure of the crystals and twinning was investigated by using optical transmission polarisation microscopy.

3.3 Results and discussion

3.3.1 Gibbsite crystal morphologies

Gibbsite is the most common polymorph of aluminium trihydroxide. It has a monoclinic space group, $P2_1/\mathrm{n}$, with $a = 8.684$ Å, $b = 5.078$ Å, $c = 9.736$ Å and $\beta = 94.54°$ [25,26]. The structure of gibbsite is pseudohexagonal with the c-axis as the pseudohexagonal axis. The morphology of natural gibbsite crystals is usually reported as pseudohexagonal plate-like with $\{001\}$ basal, and $\{100\}$ and $\{110\}$ side faces [26,27].

The crystallisation experiments of gibbsite from caustic sodium aluminate solutions resulted in crystals of different shapes and sizes. The variation in crystal morphology and size within one batch was in most cases larger than that between two batches of different growth conditions. This strongly indicates that the defect properties of the individual crystals are more important than the imposed growth conditions. Despite this variation in shapes, the three main morphologies, hexagons, lozenges and prisms, could be identified well.

Crystalline material grown from sodium aluminate solutions of C=300 g/l Na_2CO_3 and A/C=0.8 at 80°C (σ=0.63) mostly consisted of hexagonal crystals, up to 100 μm in diameter and 15 μm thick. An example is shown in figure 3.1a. The optical polarisation micrograph of such a hexagon shows sixfold twinning (figure 3.1b). The morphology of hexagons and their twin characteristics have already been described in chapter 2, where the twin boundaries have been identified as $\{110\}$ and the side faces as $\{100\}$. This regular twinning was observed for all hexagons, often resulting in crystals having a convex top and a concave bottom face (see also chapter 2). The hexagons were sometimes more block-shaped, with smaller lateral dimensions, resulting in an aspect ratio close to one.

Figure 3.1c and d shows lozenge-shaped crystals which were also found in these batches. It was shown with polarisation microscopy that the lozenges are single crystalline, with $\{001\}$ basal and $\{110\}$ side faces. Two types of lozenges could be distinguished: *thicker* lozenges of 30-50 μm in diameter and 5-7 μm thick (figure 3.1c) and *ultra thin* lozenges of 10-30 μm in diameter and only 20-50 nm thick (figure 3.1d).

Under growth conditions of C=200 g/l Na_2CO_3, A/C=0.65 and T= 80°C (σ=0.67), similar twinned hexagons and lozenges were obtained. However, the most dominant species in these batches were block-shaped crystals, with sizes typically 10 μm in diameter and 10 μm thick (figure 3.1e). These blocks had also twinning in $\{110\}$ and, in addition, twinning parallel to the $[\boldsymbol{a},\boldsymbol{b}]$-plane.

In the next sections, the surface topography of crystals with different morphologies will be discussed.

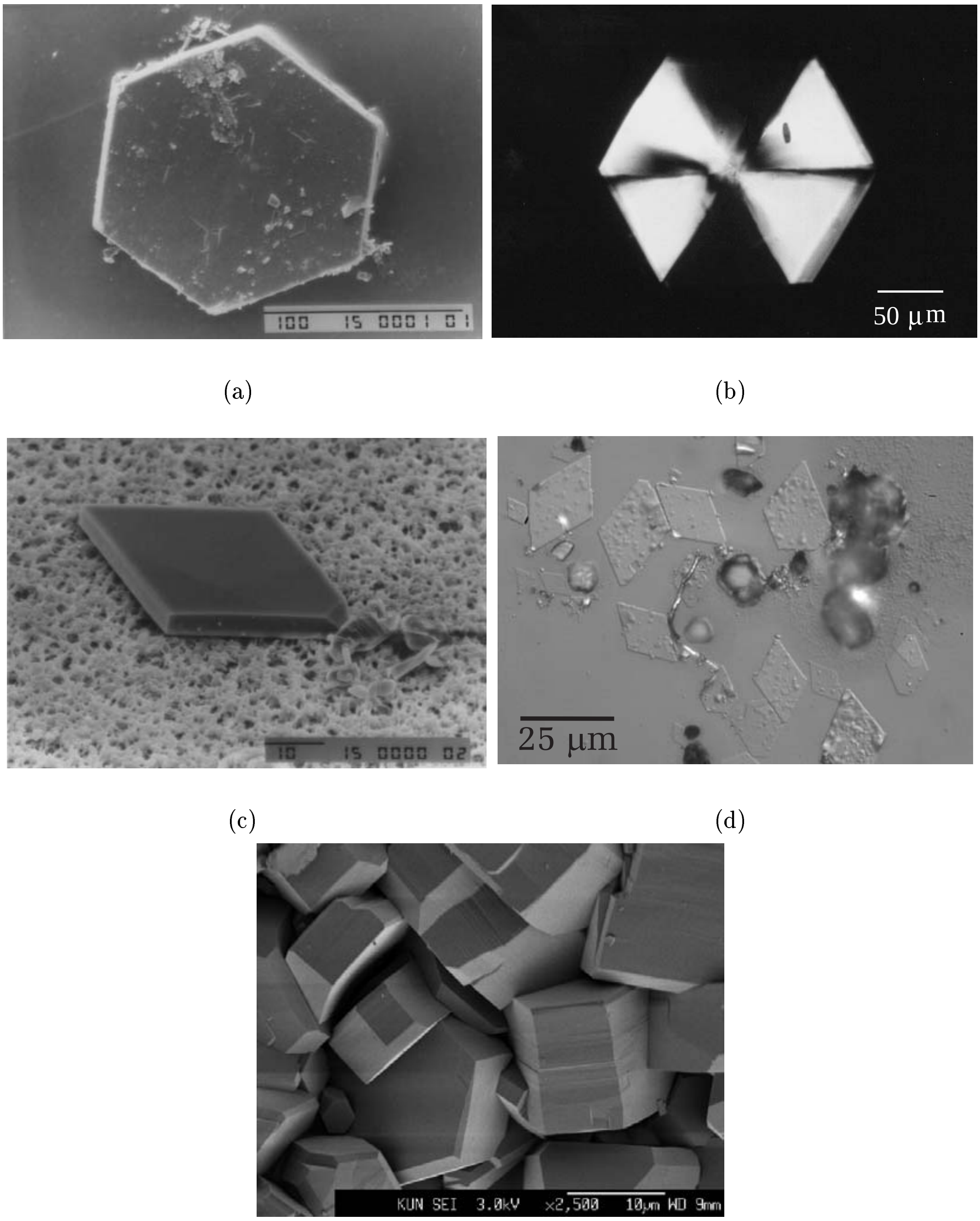

(a) (b)

(c) (d)

(e)

Figure 3.1: Micrographs of different crystal morphologies of gibbsite, γ-Al(OH)$_3$: (a) SEM image (scale bar is 100μm) and (b) optical polarisation micrograph of a sixfold twinned hexagon, (c) SEM image of a *thicker* lozenge, showing a small {101} face (scale bar is 10 μm), (d) optical micrograph of *ultra thin* lozenges, and (e) block-shaped crystals (SEM).

3.3.2 Lozenges

AFM studies of the *ultra thin* lozenges of figure 3.1d showed reasonably smooth basal {001} faces. Neither steps nor growth hillocks were detected with AFM, which means that no step generating defects were present. Height measurements revealed that the thickness of these ultra thin lozenges was only 20-50 nanometers, corresponding to 20-50 unit cells perpendicular to the crystal surface. The lateral sizes were similar to those of the other crystals. The aspect ratio of these crystals is > 1000 and is the result of the extremely small growth rate of the {001} faces compared to that of the prismatic faces. This is explained with the weak bonding interaction present along the crystallographic $\boldsymbol{c}$ direction between adjacent layers in the packing of the gibbsite structure. The bonding between these layers consists of hydrogen bonds while within the layers stronger Al-O covalent/ionic interactions are present. Because of the strong bonds within each layer and the weak association between successive layers, the step free energy is high and, hence, the 2D nucleation rate on the {001} face is extremely low.

It was not possible to determine the exact orientation of the side faces of the ultra thin lozenges. For thicker lozenges, the prismatic faces were determined to be {110}. Therefore, the side faces of the ultra thin lozenges are believed to be {110} as well. Very often the thin lozenges were truncated with small {100} or other faces in the $\{10l\}$ zone. The relative occurrence of these side faces indicates that the growth rate ratio of $\{10l\}$ and $\{11l\}$, i.e. $R_{\{10l\}}/R_{\{11l\}}$, is at least 2. It is also possible that the relatively small $\{10l\}$ faces appeared due to impurity inhibition or suppression by a local decrease in supersaturation.

Many of the *thicker* lozenges (5-7μm thickness, aspect ratio 4-10) showed weakly bunched steps on the basal face which originate from a growth hillock near the centre of the crystal. Typical examples of such growth hillocks are given in figures 3.2a and b. In figure 3.2b, also some defects can be observed which led to a distortion of the habit. Figure 3.2c shows the basic pattern of the growth hillocks, reconstructed from many micrographs of growth hillocks on lozenge-shaped crystals. The growth hillocks had straight steps along two of the <110> directions, i.e. [110] and $[1\bar{1}0]$ in the regions A of figure 3.2c. The steps in opposite directions, i.e. $[\bar{1}\bar{1}0]$ and $[\bar{1}10]$ in region B, were more rounded. The angle between the two ridges separating the A regions from B was mostly somewhat less than 120°. This results from a two times larger step propagation velocity in regions B as compared to those of regions A. The growth hillocks had very small terrace widths, i.e. far beyond the resolution of the optical microscope used, and therefore only some bunched steps could be detected with optical microscopy. Sometimes, a weak ridge was detected in region B, separating the rounded steps roughly parallel to $[\bar{1}\bar{1}0]$ and $[\bar{1}10]$. This fourth ridge was only occasionally observed. The symmetry of the growth hillocks is conform the space group symmetry of the gibbsite structure $P2_1/\mathrm{n}$, which means that the two-dimensional point group of the {001} face is **m**, with its mirror plane perpendicular to $\boldsymbol{b}$. It is likely that the growth hillocks on the thicker lozenges are composed of a step train generated by a central screw dislocation. This leads to spiral growth and explains the enhanced thickness growth as compared to the ultra thin lozenges which grow by a slow 2D nucleation mechanism.

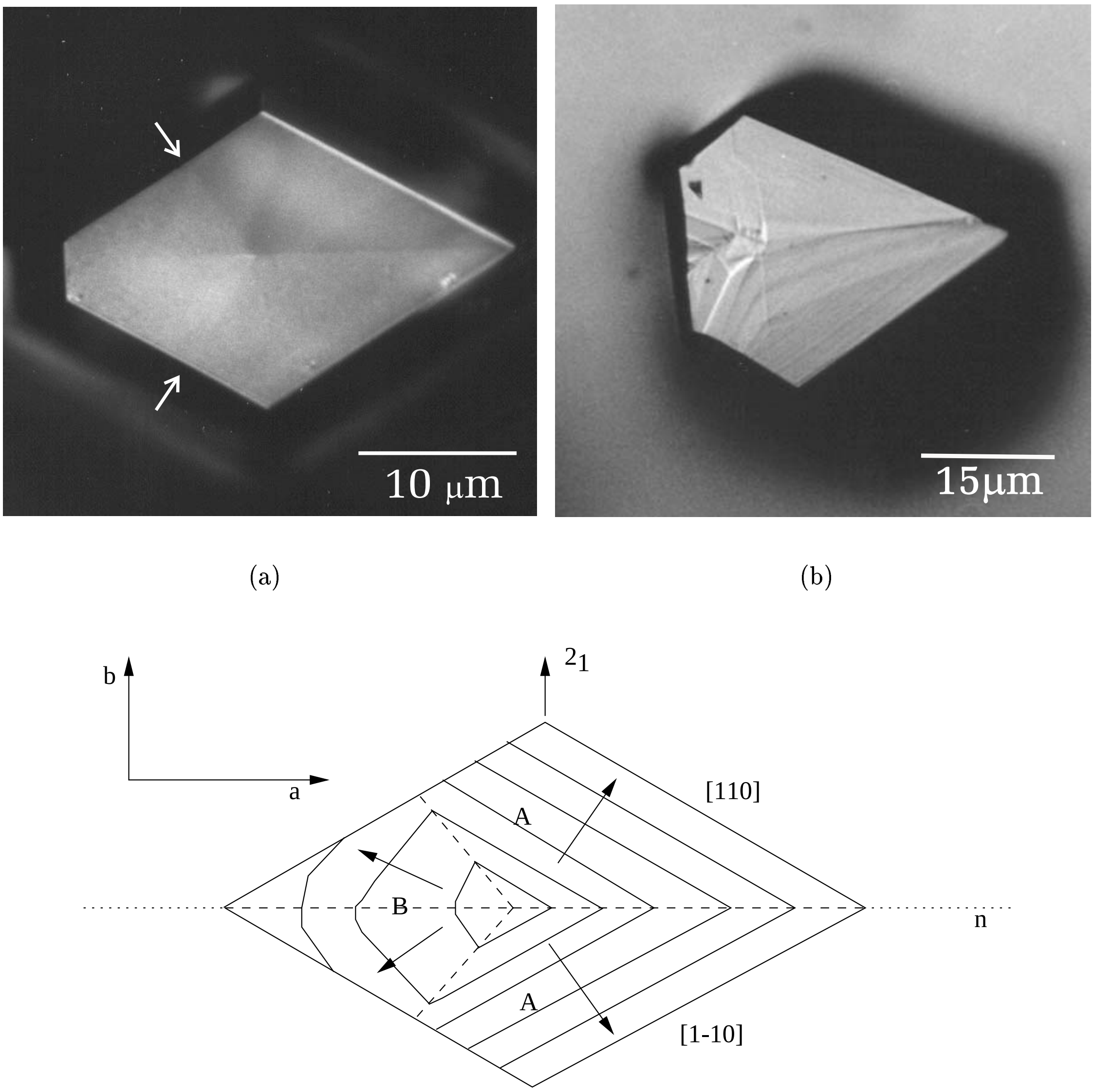

(a)

(b)

(c)

Figure 3.2: (a), (b) Growth hillocks on thicker lozenge-shaped gibbsite crystals imaged with DICM. In micrograph (a) the ridges of the growth hillock can be seen; very low steps are present which were undetectable with optical microscopy. In (b) some weakly bunched steps can be seen. Defects led to the distortion of the crystal. (c) Schematic presentation of step movement from growth hillocks on lozenges. The step propagation directions are indicated by arrows and the ridges of the growth hillock are indicated by dashed lines. The symmetry elements of the space group $P2_1/\mathrm{n}$ are also indicated. The areas A and B are referred to in the text.

Detailed observation of the basal face of the thicker lozenges revealed a rough surface on a nanometer scale (figure 3.3). The roughness was caused by hemi-spherical particles or 2D nuclei which varied from a few nm to 50 nm in diameter. Their height was 1-10 nm. The particles did not adsorb preferentially at specific sites, but appeared to be randomly distributed on the terraces. These particles could have been introduced during separation of the crystals from the mother liquor, i.e. due to a shut-off effect. Another possible explanation can be the overlapping plates as observed by Lloyd et al. [21]. These features should then be the spreading {001} plates acting as a growth mechanism. However, the present AFM micrographs as in figure 3.3 show hemi-spherical particles with a habit very different from the overlapping plates observed by Lloyd. Another possibility to explain the surface roughness observed is a continuous birth and spread mechanism as suggested by Freij et al. [22]. This 2D nucleation mechanism occurs simultaneously with the dislocation growth mechanism. The origin of these 2D and/or 3D particles is still not clear.

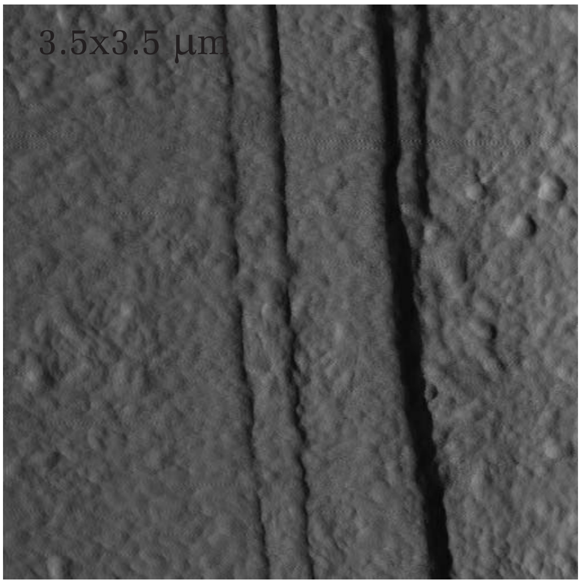

Figure 3.3: Hemi-spherical particles or 2D nuclei which appeared on the basal {001} face of lozenge-shaped gibbsite crystals (AFM).

The prismatic faces, {110} and {100} of the lozenges, were too small to examine with optical microscopy or AFM. Using SEM, most of the faces showed surfaces which were relatively flawless. Neither steps nor hillocks were detected on these thin faces. However, it must be realised that SEM is not capable of detecting steps lower than a few nanometers. It is not probable, that the growth of these faces of the ultra thin lozenges was dominated by a spiral growth mechanism, as for geometrical reasons the screw dislocations would leave these surface during growth. It is likely, that these planes grew by a 2D nucleation mechanism. Moreover, the thicker lozenges have similar lateral sizes as the ultra thin lozenges, suggesting that the prismatic faces of these thicker lozenges grow by the same 2D nucleation mechanism.

3.3.3 Hexagons

Most of the surface topographic observations described in this chapter were obtained from the {001} basal faces of the relatively large, hexagonal, twinned crystals. The large size of these faces made them more accessible for investigation. The surface morphology of these {001} faces strongly deviated from the lozenge-shaped crystals described above. Some observations of the prismatic {100} faces will also be described in this section.

Step patterns

Step patterns were briefly discussed in the previous section, where straight steps were found to be present on lozenges along two <110> directions, and rounded steps were observed to propagate in opposite directions. Similar, but also different patterns were observed on the twinned hexagons.

Very low steps were detected on the {001} basal faces. In figure 3.4, very low straight steps imaged by AFM are shown. They were present on relatively smooth parts of the {001} basal faces. The height of these steps was about 0.4 nm, which is half the size of the unit cell along the *c*-axis. This means that the gibbsite surface grows with d_{002} layers, corresponding to single AB stacking layers, in accordance with the selection rule l=2n for {00l} for the monoclinic space group $P2_1/\mathrm{n}$. Often, two of those low steps collided and formed a double growth step, i.e. d_{001}, with a height of about 0.9 nm, equal to the unit cell dimension.

Furthermore, macro steps were commonly observed on the {001} crystal surfaces. Figure 3.5a gives an example of such steps on the {001} faces. Here, the crystals are part of an agglomerate. The surface show straight macro steps along the <110> and <100> directions. Both step directions, <110> and <100>, correspond to Periodic Bond Chain

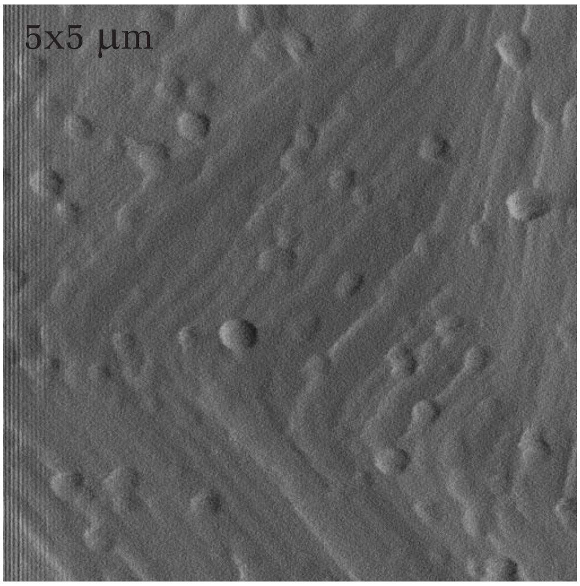

Figure 3.4: Very low steps, observed on the {001} basal face of hexagonal gibbsite crystals (AFM).

(PBC) directions which are strong bonding directions in the crystal structure (see chapter 6). The <110> steps were, in general, the most prominent ones. The height of the macro steps ranged from a few unit cells to hundreds of nm or even one or a few μm. The accumulation of somewhat higher steps to macro steps is shown in the AFM micrograph of 3.5b.

Figure 3.5c shows characteristic macro step patterns which were observed on the convex top face of perfectly twinned hexagons. Macro steps emanated from the edge of the crystal and, more specific, from the corner of a particular twin domain. They were oriented at an angle of 30° ± 10° relative to the {100} side faces. This suggests that the direction of these steps is <130> which is a - somewhat less stable - PBC direction in the monoclinic gibbsite structure. Closer examination of these <130> macro steps using SEM revealed that they were zig-zag shaped, being composed of parts of <110> and sometimes <100> steps (figure 3.5d). The step flow mostly stopped near the centre of the hexagon, due to the presence of stress. Lower steps in the <130> direction were more rounded and showed many cusps, but also these steps were composed of <110> step segments. In most cases, the <130> steps changed their overall growth direction when passing a twin boundary, and again obtained an overall <130> direction on the next crystal domain.

As was observed for the lozenges, also the basal faces of the hexagons were usually rough on a nanometer scale as a result of small hemi-spherical particles and/or 2D nuclei. Large particles, more than tens of nm in height, were superimposed on the step trains as step decoration or randomly lying on the surface. Smaller particles or 2D nuclei, less than 10 nm in diameter, were also observed. As was discussed in the previous section, these particles can be 2D nuclei, competing with the steps during growth or they might be the result of a shut-off effect.

In addition, impurity blocking of steps was observed on surfaces of some batches, figure 3.5e. The shape of these steps is quite rough. This suggests that the impurities adsorbed on the terraces are almost immobile and disturb the step motion.

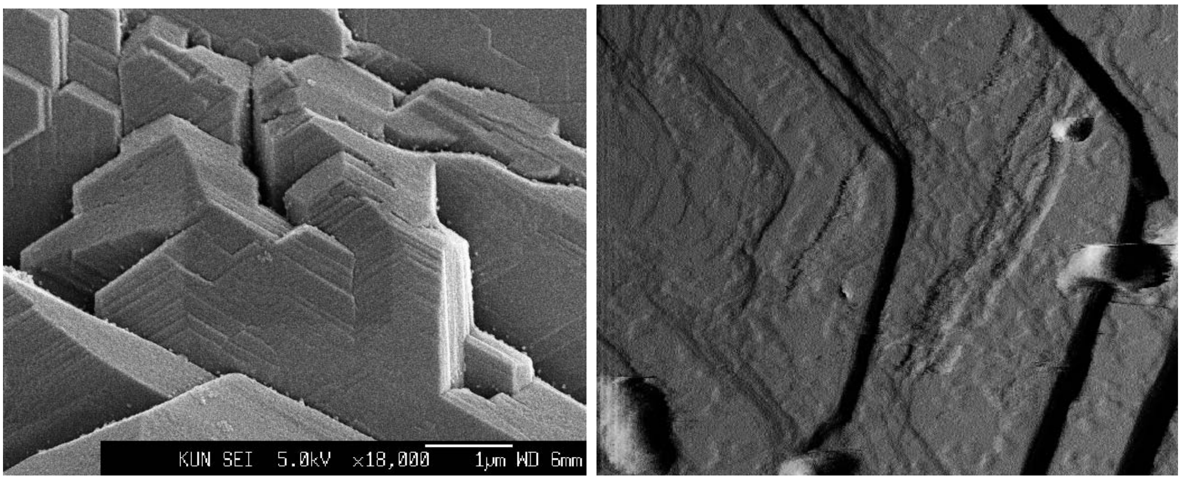

(a) (b)

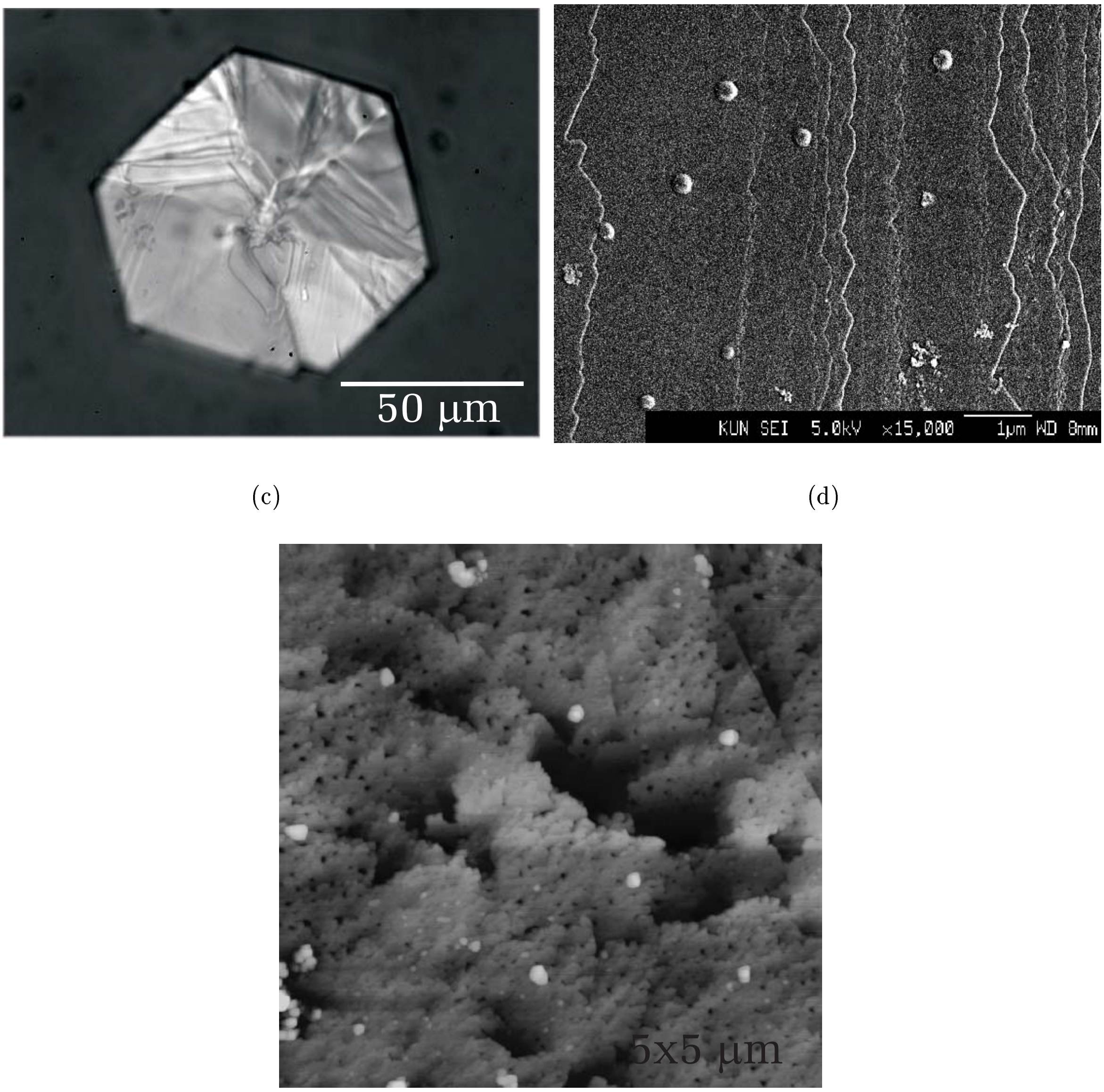

(c) (d)

(e)

Figure 3.5: In this figure, step patterns on hexagonal sixfold twinned gibbsite crystals are shown: (a) Agglomerate showing step patterns at the {001} basal face with <110> and <100> steps (SEM), (b) step bunching (AFM, x-size is 2 μm), (c) optical image of typical <130> step patterns on the convex top face of a perfectly sixfold twinned gibbsite hexagon, (d) <130> steps composed of small <110> and sometimes <100> steps (SEM), and (e) steps blocked by impurities (AFM).

Growth hillocks

The typically shaped growth hillocks found on the thicker lozenges were also observed on the basal face of many twinned hexagons. Examples are shown in figures 3.6a and b. The centre of such a hillock with low step height is shown in figure 3.6c. The step height as deduced from this AFM micrograph is 0.47 nm which, again, corresponds to half a unit cell. It is not possible to verify whether the steps follow a spiral pattern, due to a minimal shut-off effect. Many rounded growth hillocks with very low step heights were also observed on the basal gibbsite surfaces (figure 3.6d).

Another group of growth hillocks was observed which have their growth centre in the vicinity of another crystal or at the crystal edge as is shown in figures 3.6e and f. These hillocks were very steep with straight, bunched steps in the <110> direction. The inclination of these elevations is about 23° which is roughly 7 times more than the shallow growth hillocks on the lozenges and the hexagons, described above. This suggests that here growth has not been induced by a single dislocation but apparently by a group of dislocations, by intense 2D nucleation on edges or via contact nucleation, induced by contacting crystallites. Judged from the steepness of these hillocks, the mechanism must be very effective. Furthermore, it was observed that the steep growth hillocks were capable of passing a twin boundary without changing their direction or step height.

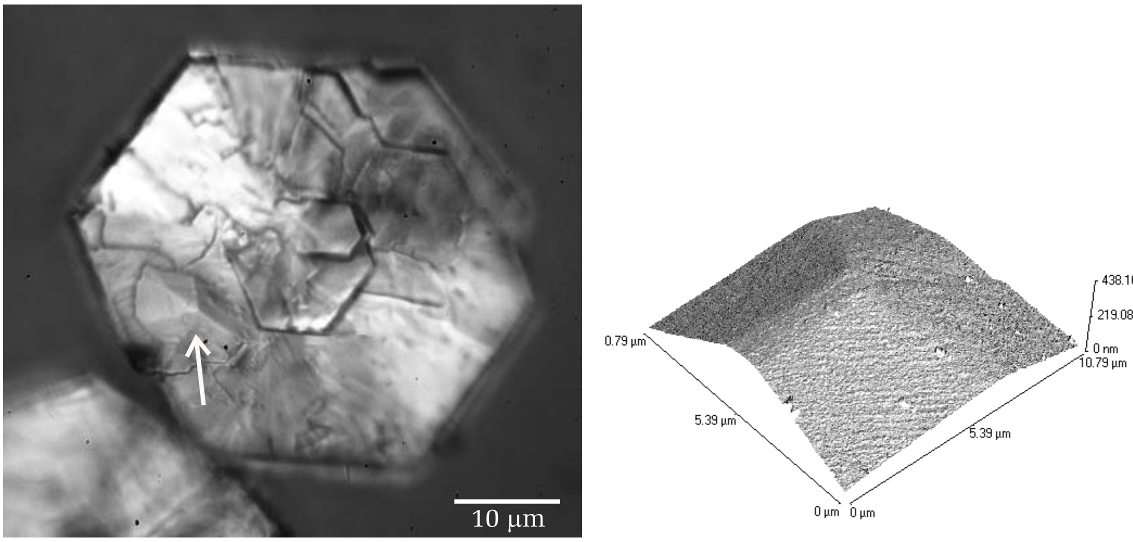

(a) (b)

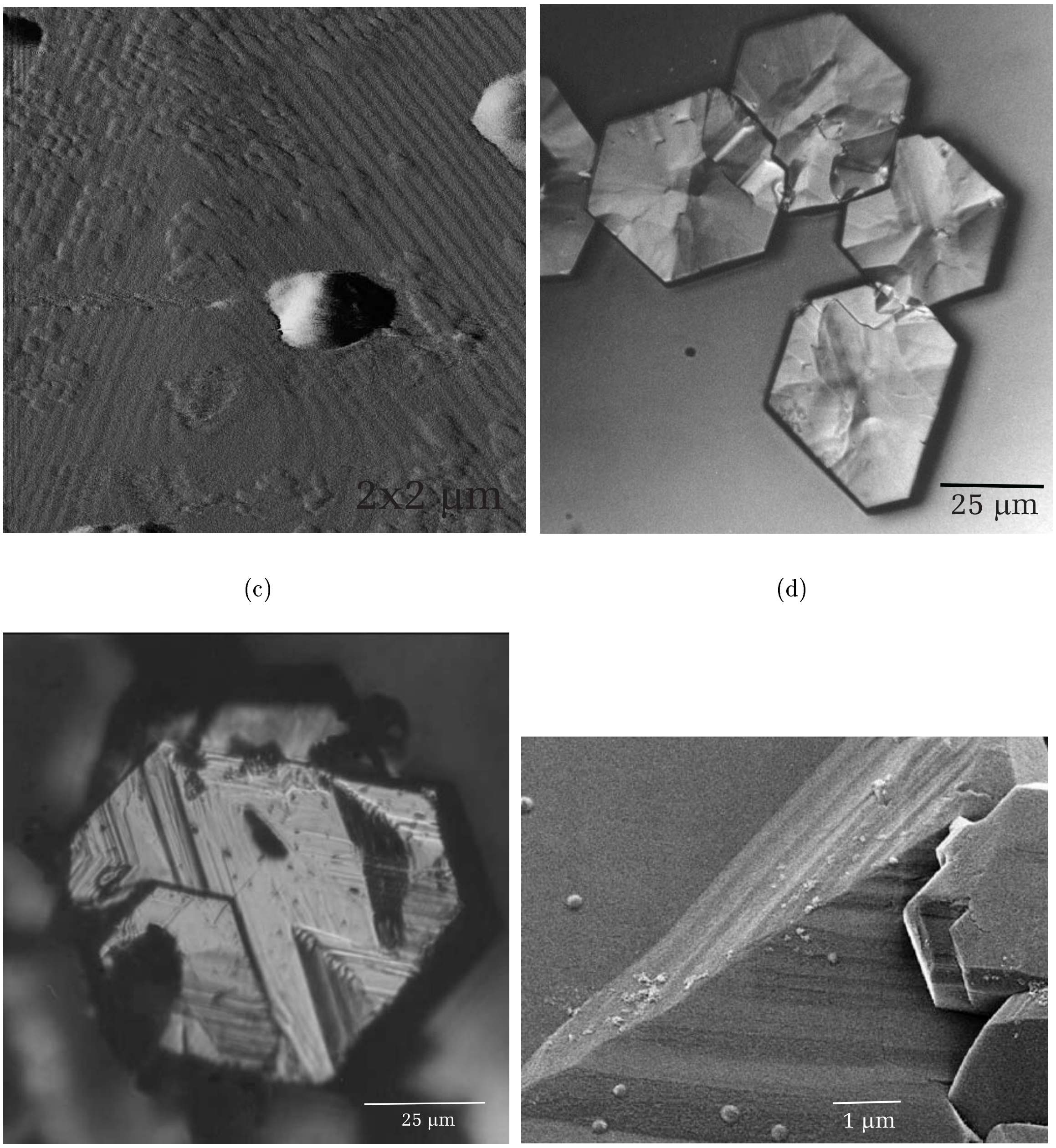

(c) (d)

(e) (f)

Figure 3.6: Growth hillocks on the basal face of hexagonal sixfold twinned gibbsite crystals: (a) Optical micrograph of a triangularly shaped growth hillock indicated by an arrow, (b) AFM topograph of a triangularly shaped growth hillock, (c) step pattern of a growth hillock (AFM), the step height is 0.47 nm, (d) hexagonal crystals with rounded growth hillocks (DICM) (e) large, steep growth centres in the vicinity of the crystal edge (DICM), and (f) detail of a growth centre of the type as shown in (e) (SEM).

Contact nucleation

In the previous section, steep hillocks in the vicinity of crystal edges are described. These indicate a group of dislocations as a step source or an enhanced formation of 2D nuclei via contact nucleation. Contact nucleation was often observed in the case of an agglomerate. The edges of two adjacent crystals were in contact and in many cases they acted as step sources by lowering the activation barrier for 2D nucleation (figure 3.7).

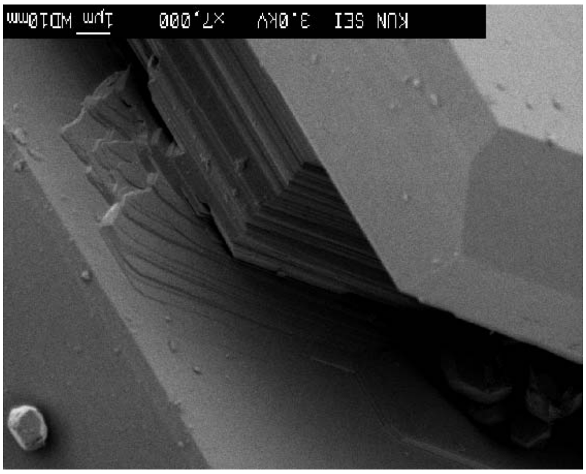

Figure 3.7: Steps generated by contact nucleation (SEM).

Crystallites

On the basal faces of the twinned hexagons many small crystallites, both lozenge and hexagonal in shape, were found to adhere on the surface, especially near the centre (figure 3.9). The thickness of the crystals varied from tens of nm to several hundreds of nm. Occasionally, the crystallites adsorbed had a height of several μm. The crystallites had characteristic shapes for gibbsite. They showed well-defined hexagonal as well as lozenge-shaped morphologies. The possible origin of these crystallites might be from subcritical nuclei in the solution which have transformed into a crystalline state upon interaction with the crystalline lattice of the underlying mother crystal and have developed upon growth to well-faceted crystallites. It is also possible that small gibbsite nuclei floated in the liquid and sedimented onto the surfaces of the crystals. Most crystallites were misoriented with respect to the mother crystal, possible due to formation on a dislocation site emerging at the surface of the mother crystal as suggested before [17–19]. In other cases, their orientation with the underlying mother crystal was more or less the same with respect to the crystallographic $\boldsymbol{a}$ and $\boldsymbol{b}$ directions, which suggests reorientation during formation or deposition.

Many of the crystallites were incorporated into the mother crystal. This can be explained with a difference in growth rate between the crystallites and the underlying mother crystal. The small crystallites probably continued to grow after adsorption on the surfaces. However, with a smaller growth rate than that of the growth rate of the mother crystal. This can be explained by the higher amount of defects in the mother crystal and, consequently, their larger probability to have step sources of higher strength. In that case, steps covered the surface much faster than the 2D nucleation or low strength spiral mechanism which was probably active on the small crystallites. In chapter 5, it will be shown that larger gibbsite crystals indeed possess more defects than smaller crystals.

Sometimes, clefts were formed around the misoriented crystallites as a consequence of the growing mother crystal. In other cases, the crystallites were overgrown without clefts. This introduced low angle grain boundaries when the crystallites were misaligned, due to the inelasticity of the crystal structure. These low angle grain boundaries could become step sources themselves. This category of faults did not deeply penetrate the bulk crystal. Large crystallites on the basal face could also serve as step sources by contact nucleation.

Planar faults

Planar faults in gibbsite were found as striations on the basal face of the crystals. They were strictly parallel to the crystallographic <110> and <100> directions and penetrated the crystal deeply as was verified with optical microscopy. It was shown that these planar faults continued through the crystal, perpendicular to the basal face within a few degrees. Figure 3.8b shows a part of a sixfold twinned hexagon with the outcrops of many of these planar faults at the {001} surface which are indicated by arrows. Besides these striations, strong line features could be observed which were probably the result of misoriented microcrystals partly grown-in, as discussed in the previous section. It is clear that also these relatively large grain boundaries have crystallographic directions.

The planes did not generate steps; often steps passed these faults, as is shown in figure 3.8c. This led to a particular bunched pattern, the height of which was about hundred nanometer. With optical microscopy, it was found that the planar faults indeed sometimes

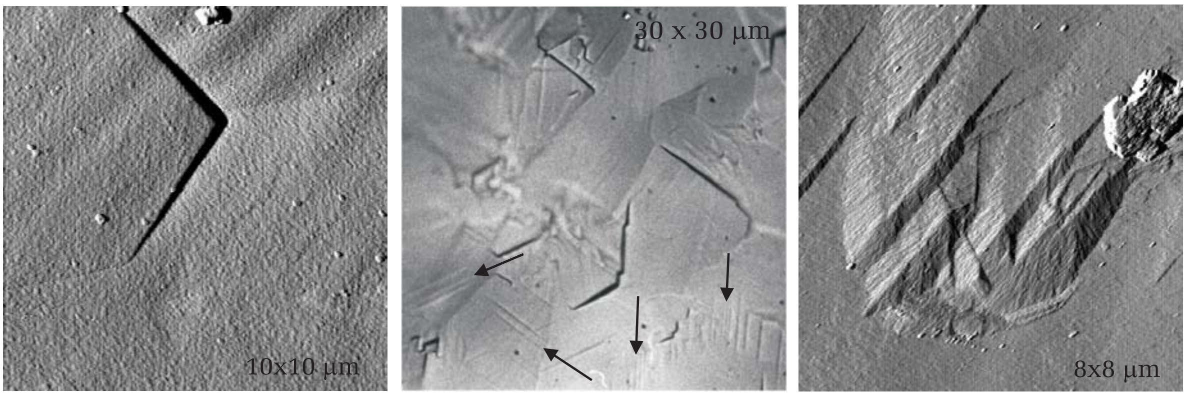

(a) (b) (c)

Figure 3.8: Planar defects in gibbsite: (a) Outcrops of low angle grain boundaries introduced by an ingrown crystallite on top of a basal face (AFM), (b) stacking faults indicated by arrows (OM), and (c) steps passing stacking faults (AFM), with a step propagation towards the left upper corner.

stopped just below the surface, which means that a layer grew over the crystal surface covering the defects just before the end of the crystal growth process.

Twin boundaries

The angle between the basal surfaces of adjacent twin domains of the hexagon is about 178° instead of 180° for a perfect hexagonal crystal. This generates a very shallow reentrant corner between the faces on the concave top surface of the hexagons (see chapter 2). These and other twin boundaries were not important step sources. Occasionally, 2D nuclei were arranged along a twin boundary. The fact that twin boundaries hardly affect the growth of the basal faces also follows from the fact that many macro steps passed a twin boundary without changing their growth directions.

Concave and convex

The gibbsite crystals that were twinned in a very regular way, often had a convex top and concave bottom face. Several of these twinned crystals possessed different surface features on the concave and the convex crystal sides. The convex side was characterised by straight macro steps in the <110> and overall <130> directions. This side also showed large, more or less polygonised growth hillocks with their centres in the vicinity of the crystal edge. The concave side showed many misoriented crystallites, as elaborated in the previous section, which resulted in a more irregular surface. In addition, rounded growth hillocks were observed on this side. In figure 3.9, typical AFM images of both the convex and the concave side of a sixfold twinned crystal are shown.

Following the point group 2/m as deduced from the space group $P2_1/\mathrm{n}$ of the crystals, the two opposite surfaces (001) and $(00\bar{1})$ should exhibit an identical morphology. Therefore, the observations suggest the occurrence of hypomorphism, or more specific the absence of the two-fold axis, as was also found for $K_2Cr_2O_7$ crystals [28] and $NH_4H_2PO_4$ [29]. On the other hand, the concave side of sixfold twinned crystals contains reentrant corners between adjacent crystal domains. Therefore, nuclei are expected to nucleate on these faces more easily than on the convex faces. In the latter case, the hypomorphism is explained as the result of twinning. The differences between the surface characteristics of the two opposite sides of the twinned crystals were not always clear. No differences were found for the opposite {001} faces of the lozenge shaped crystals.

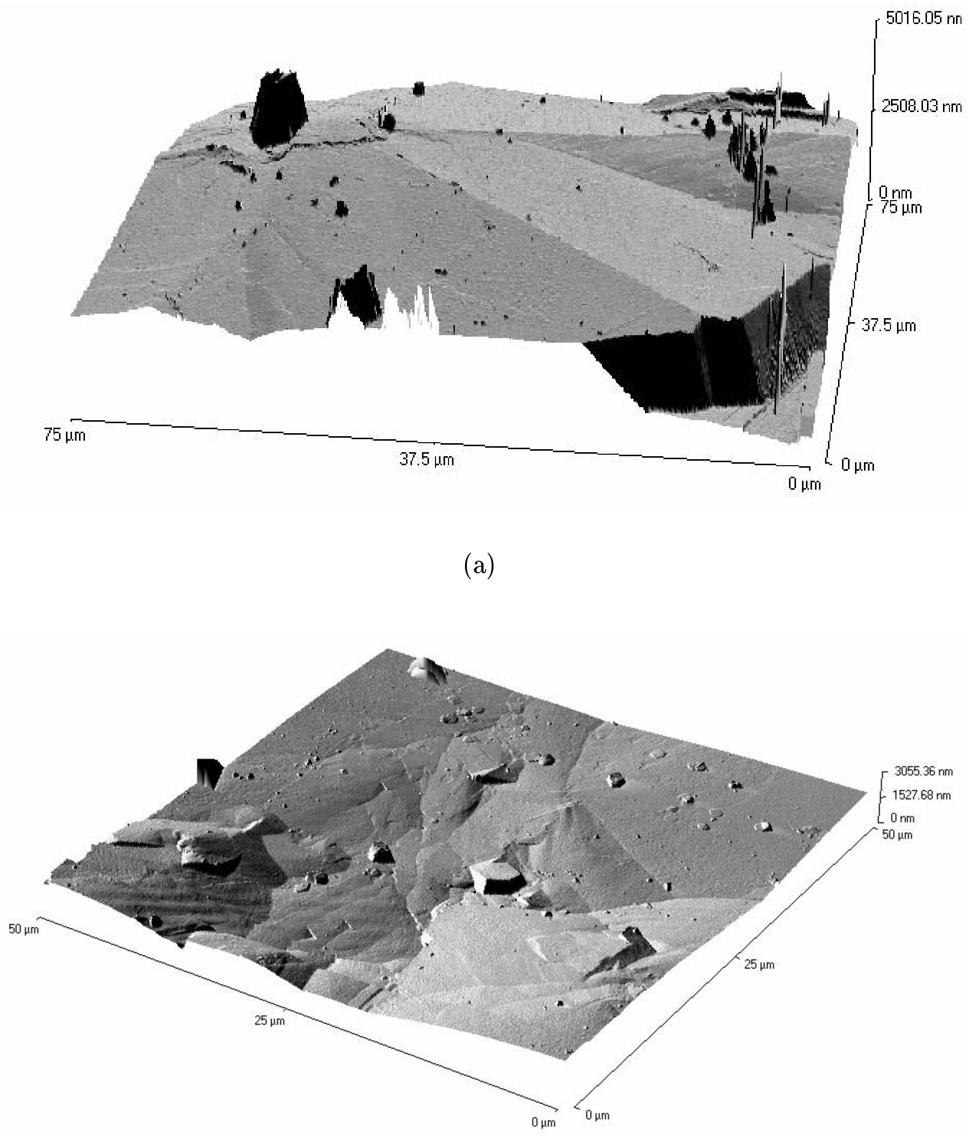

(a)

(b)

Figure 3.9: (a) Convex and (b) concave side of a hexagonal twinned crystal (AFM).

Prismatic faces

The {100} side faces of the sixfold twinned hexagons sometimes appeared relatively flawless, but were mostly characterised by a striated structure (figure 3.10a). The thickness of the layers varied from less than 50 nm up to a few microns, on which no steps were observed, moreover, they appeared rather rough. The striations can be the outcrops of planar faults, like stacking faults or multiple twinning perpendicular to $\boldsymbol{c}$. Furthermore, the deposition and subsequent lateral growth of a 3D nucleus poorly oriented on the basal face can also result in a slightly misoriented layer and hence in a layer structure. The striations can not be the result of growth bands due to a non-uniform incorporation of impurities during growth. Then the striations should not be visible on the side faces, but only on cross sections of the crystals [30].

In the case that, the striations are the outcrops of stacking faults, the packing of certain $Al(OH)_3$ layers is according to the bayerite sequence. Sufficiently high densities of stacking faults can be confirmed with X-ray powder diffraction. However, the XPD-data obtained were similar to the XPD-data of gibbsite from the literature [27]. This means that the density of the planar faults was too small, the packing was not according to the bayerite sequence, or the literature XPD-data are based on gibbsite crystals highly striated as well.

In the case that, the striations are due to the existence of twin lamellae perpendicular to $\boldsymbol{c}$, it can be detected using polarisation microscopy with crossed polarisers. However, no dark and bright lamellae were revealed, which was possibly due to the 'small' thickness, i.e. less than the resolution of the optical microscope, of the layers.

The occurrence of a 3D (or 2D) nucleus poorly oriented on the basal face, leading to a poorly oriented layer by lateral growth, is shown in figure 3.10b. Here, the upper part of the 'crystal sandwich' has a slightly different orientation than the lower part.

Conclusive evidence, whether these layers were formed by stacking faults, multiple twinning or poorly oriented nuclei which subsequently grew were not been obtained in this study.

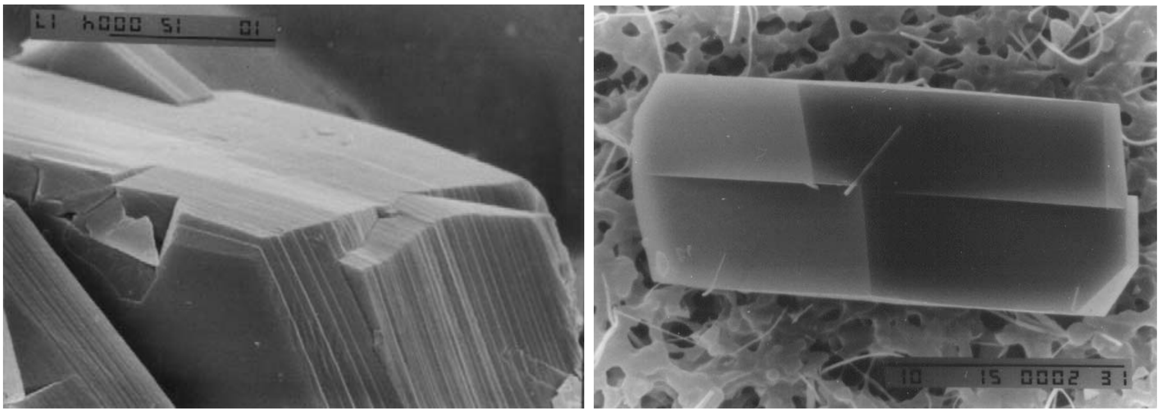

(a) (b)

Figure 3.10: SEM images of prismatic faces: (a) Prismatic faces with a layered structure (scale bar is 10μm), and (b) a twist crystal (scale bar is 10μm),

Many of the side faces also showed a layer structure in the reentrant corners at the outcrops of the sixfold twin domain boundaries. Some of the reentrant corners were curved as is shown in figure 3.11, indicating the activity of the reentrant corner as a step source.

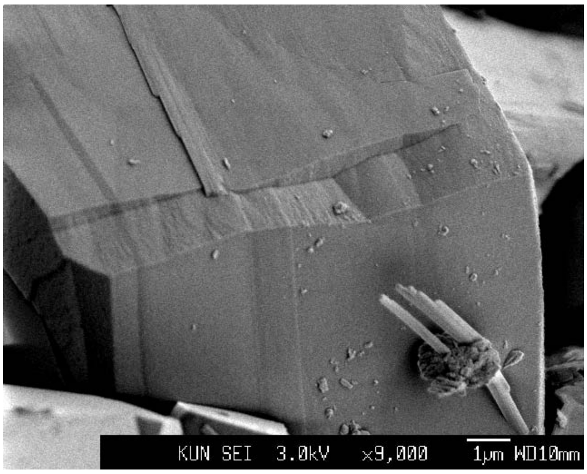

Figure 3.11: Curved reentrant corner as a result of step generation (SEM).

In addition to the striated structure, several hexagonal sixfold twinned crystals showed a planar fault parallel to {001} traversing the crystal halfway between top and bottom faces. It is likely that these hexagons were mirror twinned perpendicular to the *c*-axis at the early nucleation stage, as was described for prisms in chapter 2 and in section 3.3.4. This mirror twinning could not be confirmed with polarisation microscopy, since it was too difficult to view these crystals from their side face. It was also not possible to verify this mirror twinning by examining the basal face, the two separate domains have the same extinction direction. Hexagons with such a twin boundary did not have the clear layer structure as shown in figure 3.10a, suggesting that here the multiple planar faults did not occur.

3.3.4 Prisms

The different growth characteristics, which are described above for the lozenges and hexagons, were mostly also observed on the block-like and prismatic gibbsite crystals. On the basal {001} faces of the prisms, also straight macro steps parallel to one of the crystallographic directions <110> or <100> were observed. Step growth at growth hillocks and generated by contact nucleation were also imaged on these faces. Overgrown crystallites were occasionally observed. These features were revealed with optical microscopy and SEM. AFM was not used, because the prisms were too small to handle for examination.

Most of the prismatic surfaces showed striations parallel to the basal face, in a similar way as for the twinned hexagons. Steps were never observed on the striated structures. Occasionally macro steps were found on non-striated prismatic surface areas. An example is shown in figure 3.12. The steps were curved and mainly directed parallel to the basal face. Although the large number of defects as well as the mosaic structure discussed below would suggest that growth of the prismatic faces proceeds by contact nucleation or macro spirals, steps on these faces were observed in only a few cases. Growth hillocks were not observed. This implies a 2D nucleation growth mechanism.

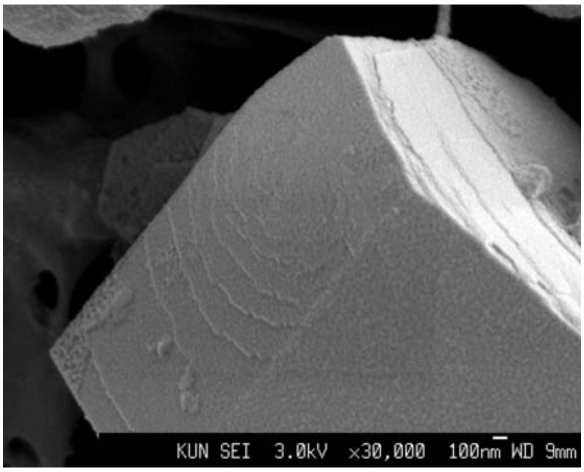

Figure 3.12: Step patterns on prismatic faces (SEM).

In many cases, protruding block patterns developed on the prismatic surfaces, as is shown in figures 3.13a and b. These block patterns probably reflect a mosaic structure of these gibbsite crystals. Mosaicity and cracks in growing crystals may be caused by stresses resulting from a substantial thermal gradient or the inhomogeneous distribution of point defects [31]. The stress centres induce lattice distortions. Consequently, misfit dislocations will be nucleated and spread in the crystal. In brittle crystals, like gibbsite, where dislocations cannot move, the continuous variations in lattice spacing induced by growth may be resolved by cracking if the crystals grow large enough [31]. Another possibility for the creation of misoriented blocks is a dendritic nucleation phase at high supersaturation. Upon further growth, the dendrite branches might meet and stick one to another with a mismatch, giving rise to mosaic blocks. Furthermore, the appearance of misoriented 2D or 3D nuclei and the sedimentation of little crystals floating in the liquid onto the surface can induce cracking, splitting and twisting of the crystals.

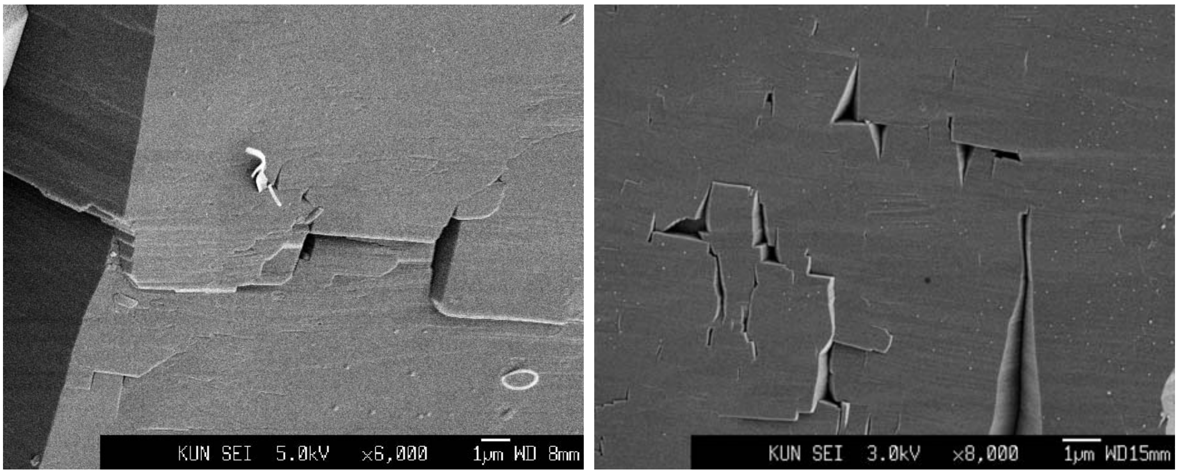

(a) (b)

Figure 3.13: (a), (b) Block patterns on prismatic faces of a mosaic prism (SEM).

Since the crystallisation of gibbsite has been performed under isothermal growth conditions, and the appearance of mosaicity immediately after or during its nucleation was never observed, the distribution of point defects and the corresponding internal stress and dislocations due to misfit nuclei or a nucleation mechanism which facilitates the appearance of misaligned 2D and 3D nuclei are expected to be the main courses of the mosaic structure. Mosaicity has been reported for numerous solution grown crystals in the mineralogical literature which relates this phenomenon also to the presence of impurities [31]. The cause of internal stress, dislocations and grain boundaries is not completely clear for gibbsite crystals grown from sodium aluminate solution.

Many prisms were inclined along $\boldsymbol{c}$, reflecting a mirror twin perpendicular to the c-axis (see chapter 2). In general, the mirror twin was half-way the prism, indicating that twinning occurred during the nucleation phase of gibbsite crystallisation. In figure 3.14a, it is shown that such a twin boundary is not confined to one single plane, but includes many layers. Often many adjacent, parallel twin planes led to prismatic faces with numerous inclinations, giving a shallow zig-zag pattern. In case that the spacing between the lamellae was very small, this could result in the striated structure as described above.

Some of the prisms had chamfered faces, {112} and/or {101} (figure 3.14b). Using high magnification, the surfaces of these facets usually appeared rather rough with very small, irregular cone-shaped features parallel to the c-axis. Because of their limited size, these features could not be well resolved with SEM.

It is shown that the prismatic faces of prisms were very often irregular in appearance. The many irregularities and the mosaic structure should act as many sources for step growth, but steps were only occasionally observed. It is not clear why the growth rate of these irregular faces is not that large that the prisms develop into plate-like crystals. Apparently, the blocking activity of impurities plays a role.

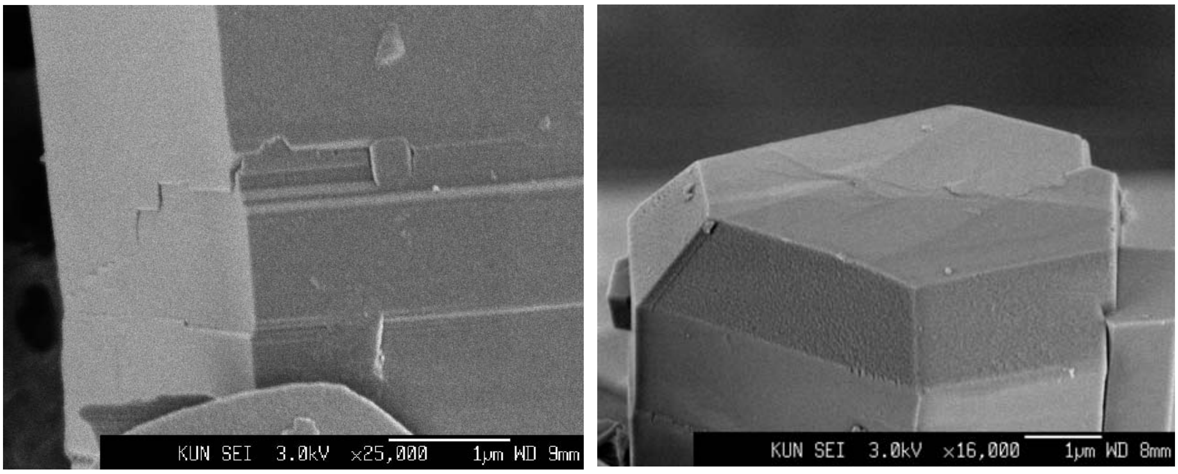

(a) (b)

Figure 3.14: SEM images: (a) a prism mirror twinned along {001}, and (b) chamfered faces.

3.4 Conclusions

In this chapter, attention was focused on the surface topography of the three main types of gibbsite crystals - i.e. lozenges, hexagons and prisms - of which each revealed a different surface structure. Growth of the {001} basal and {110} side faces of the ultra thin lozenges proceeds exclusively by 2D nucleation and subsequent step advancement. No dislocation sources were found on any of these lozenges examined. This means that the ultra thin lozenges are the basic growth morphology of gibbsite, and growth is completely determined by 2D nucleation. However, most gibbsite crystals contain many dislocations and other defects. Single crystals with only one or a few screw dislocations ending on the basal face grow to somewhat thicker lozenges. Hexagonal and block-shaped crystals are sixfold twinned and show a complex surface topography. The different growth features on the {001} faces, such as step patterns, growth hillocks, planar faults, partly grown-in crystallites and steps generated by contact nucleation are shown to be the result of different defects in the crystals and inhomogeneities in their environment. Low steps are about 5 Å high, which is equal to half of the unit cell dimension along $\boldsymbol{c}$ in accordance with the selection rules of the space group. The surfaces of prismatic faces are characterised by striations parallel to {001}. These layers are the outcrops of planar faults or slightly misoriented growth layers. Steps sources were not resolved on the prismatic faces, which suggests that growth is according to a 2D nucleation mechanism. In chapter 2, steps generated at reentrant corners were mentioned as a source for accelerated growth in lateral direction for twinned crystals. Such steps in reentrant corners were indeed observed. Mosaicity, observed for many prisms, was related to the presence of impurities or a non-coherent 2D and 3D nucleation mechanism.

In brief, the growth of gibbsite crystals is largely determined by its defect structure, formed during the nucleation phase and during growth. This explains the large variety in habit and size of crystals grown under identical conditions. However, there is still the question why the lateral growth rate of prisms is lower than that of plates and lozenges.

References

[1] C. Misra and E.T. White, J. Cryst. Growth 8 (1971) p. 172.

[2] W.R. King, Light Metals (1973) p. 551.

[3] N. Brown, J. Cryst. Growth 29 (1975) p. 309.

[4] P.J. The, Light Metals (1980) p. 119.

[5] A. Packter and H. Daill, Crystal Res. and Technol. 17 (1982) p. 931.

[6] D. Ilievski and E.T. White, Chemeca '90 (1990) p. 1156.

[7] D. Ilievski and E.T. White, Chem. Eng. Sc. 49 (1994) p. 3227.

[8] D. Ilievski and E.T. White, AIChE Journal 41 (1995) p. 518.

[9] H. Nagai, S. Hokazono and A. Kato, Br. Ceram. Trans. J. 90 (1991) p. 44.

[10] S. Veesler and R. Boistelle, J. Cryst. Growth 130 (1993) p. 411.

[11] S. Veesler and R. Boistelle, J. Cryst. Growth 142 (1994) p. 177.

[12] S. Kumar and R.G. Bautista, Light Metals (1994) p. 47.

[13] P.G. Smith, H.R. Watling and P. Crew, Colloids and Surf. A 111 (1996) p. 119.

[14] I. Seyssiecq, S. Veesler, G. Pèpe and R. Boistelle, J. Cryst. Growth 196 (1999) p. 174.

[15] I. Seyssiecq, S. Veesler, R. Boistelle and J.M. Lamérant, Chem. Eng. Sci. 53 (1998) p. 2177.

[16] H.R. Watling, S.D. Fleming, W. van Bronswijk and A.L. Rohl, J. Chem. Soc. Dalton Trans. (1998) p. 3911.

[17] O.I. Arakelyan and A.A. Chistyakova, Sov. J. Non-ferrous Metals (1959) p. 6.

[18] V.A. Derevyankin and S.I. Kuznetsov, Sov. J. Non-ferrous Metals 2 (1961) p. 47.

[19] B. Gnyra, R.F. Jooste and N. Brown, J. Cryst. Growth 21 (1974) p. 141.

[20] N. Brown, J. Cryst. Growth 12 (1972) p. 39.

[21] S. Lloyd, S.M. Thurgate, R.M. Cornell and G.M. Parkinson, J. Cryst. Growth 135 (1998) p. 178.

[22] S. Freij, M.-Y. Lee, M. Reyhani and G. Parkinson, Proc. of the Fifth International Alumina Quality Workshop (1999) p. 41.

[23] J. Addai-Mensah, Min. Eng. 10 (1997) p. 81.

[24] B.N. McCoy and J.L. Dewey, Light Metals (1982) p. 173.

[25] H. Saalfeld and M. Wedde, Z. für Kristall. 139 (1974) p. 129.

[26] W.A. Deer, R.A. Howie and J. Zussman, An Introduction to Rock Forming Minerals (Longman Scientific & Technical, 1992) 2^{nd} edition.

[27] K. Wefers and C. Misra, Oxides and Hydroxides of Aluminium, Technical Report Technical Paper no. 19, revised Alcoa Research Laboratories, Pittsburgh, Pennsylvania (1987).

[28] A. J. Derksen, W.J.P. van Enckevort and M.S. Couto, J. Phys. D: Appl. Phys. 27 (1994) p. 2580.

[29] M.A. Verheijen, L.P.J. Vogels and H. Meekes, J. Cryst. Growth 160 (1996) p. 337.

[30] K. Sangwal and K.W. Benz, Prog. in Cryst. Growth and Char. of Mat. 32 (1996) p. 135.

[31] A.A. Chernov, J. Cryst. Growth 196 (1999) p. 524.

Chapter 4

Growth rate analysis of gibbsite single crystals growing from aqueous sodium aluminate solutions

C. Sweegers, W.J.P. van Enckevort, H. Meekes,
I.D.K. Hiralal and A. Rijkeboer [1]

Abstract

In-situ optical microscopy was used to measure the growth rate of gibbsite single crystals growing from aqueous sodium aluminate solutions. The growth rate was measured for various crystal faces, i.e. {100} and {001} faces in case of twinned hexagons and {110} faces for single crystalline lozenges. A considerable dispersion in crystal growth rate was measured: the growth rates varied from crystal to crystal within the same experiment as well as from experiment to experiment. They also fluctuated in time. The origin of this dispersion in growth rates is discussed. The results of the growth rates measured as function of the driving force which were averaged over several crystals were fitted with growth rate equations for various growth mechanisms. It is shown that the birth and spread-type growth rate equation defined by Nielsen [1] as well as an equation derived in this chapter for contact nucleation growth at the intersection line of contacting crystallites can be used to describe the growth rates of gibbsite in all crystallographic directions.

---

[1] The work in this chapter has been submitted to *J. Cryst. Growth.*

4.1 Introduction

In the Bayer process which is industrially used to extract aluminium oxide from bauxite, gibbsite is the mineral recovered from the crystallisation of aluminium hydroxide from aqueous sodium aluminate solutions [2].

Gibbsite growth proceeds very slow, typically 1-2 μm/h, and despite a lot of research the effects of crystallisation conditions and impurities are still not well established. Detailed knowledge of the crystallisation process is necessary to obtain proper insight and a quantitative description. The possibility of predicting the gibbsite growth behaviour under various conditions will be very useful, especially for practical purposes.

From earlier work on gibbsite crystallisation using batch crystallisers [3–6], general growth rate equations were obtained, which are based on:

$$\boldsymbol{R} = k_0 \exp\left(\frac{-E}{RT}\right) * S^2. \tag{4.1}$$

Here, k_0 is a kinetic coefficient, E the activation energy for 2D nucleation, T the crystallisation temperature and S the crystallisation driving force. Several definitions have been given for the driving force, S. From the fits of the corresponding expression (4.1) to experimental growth rates, the growth rate constants k_0 and E were obtained. The exact values of these parameters were strongly dependent on the definition of the driving force used. A proper definition for the driving force for crystallisation is, therefore, necessary to obtain a realistic description of the growth rate. This will be the subject of section 4.2.

The square dependence of the growth rate on the driving force in eq. 4.1 suggests that gibbsite crystallisation is controlled by a screw dislocation growth mechanism as was deduced for many crystals growing at low supersaturation in aqueous systems [7,8]. When applying the spiral growth theory to these systems, the rate determining step is assumed to be the integration of atoms, molecules or ions into the kink sites of the spiral steps. In case of ions, they enter from an adsorption layer consisting primarily of constituent ions in an equivalent (electroneutral) ratio. The growth rate equation of gibbsite crystallisation based on eq. 4.1 was not based on actual growth mechanisms, but was the result of semi-empirical data fit procedures, and therefore this does not reveal the actual growth mechanism. Still, the relation between the growth rate and driving force according to this equation is generally accepted in the literature.

In batch and bulk experiments, the growth rates can be distorted by nucleation, agglomeration and attrition. Moreover, the growth behaviour of different types of crystals and different crystal faces can not be studied in such experiments. These problems are avoided in experiments where individual crystals are followed in time to measure their linear growth rate, i.e. the growth rate in well-defined crystallographic directions. Only a few studies have been reported in which the linear growth rate of individual gibbsite crystals was determined. In 1973, King reported measurements on the growth rate of isolated gibbsite crystals attached to a polyacrylate film on a glass slide in various pure sodium aluminate solutions at 80°C [4]. He derived a growth rate equation:

$$\boldsymbol{R} = k_0 \left(\frac{c - c_{eq}}{FC}\right)^2, \tag{4.2}$$

where c and c_{eq} are the actual and the equilibrium $Al(OH)_3$ concentration of the solution at the crystallisation temperature T, and FC is the free caustic, which is the total amount of sodium hydroxide minus the amount required to convert aluminium hydroxide to the aluminate ion, $Al(OH)_4^-$.

Lee et al. [9] carried out an *in-situ* microscopic study on the growth of isolated gibbsite crystals. In this study, the phenomenon of growth rate dispersion was observed. The growth rate was found to vary not only from experiment to experiment, but also from crystal to crystal within the same experiment as well. To determine the effect of supersaturation on the gibbsite crystal growth rate, the growth was measured relative to that of seed crystals. This means that the growth rate was related to the growth rate of the seeds grown under standard conditions. This method was validated because changing the conditions affected the different crystals by the same relative amounts. It was concluded that growth of the prismatic faces occurs via a spiral growth mechanism [9]. The basal faces grow, above a certain relative supersaturation, by a birth and spread mechanism, while spiral growth is the major mechanism operating below this value of relative supersaturation.

In this study, the linear growth rates of individual faces of different types of gibbsite crystals measured *in-situ* as a function of the driving force are presented. The {001} basal and {100} side faces of sixfold twinned hexagons, the {110} faces of single crystalline lozenges, and the {001} and side faces of prisms were examined. The indexing of these faces in case of single crystalline and twinned gibbsite crystals has been described in chapter 2. A schematic presentation of the different crystal types is shown in figure 4.1. The results will be interpreted using several growth rate equations from the literature in combination with the conclusions derived from surface topographic studies, described in chapter 3. Furthermore, a new model involving multiple contact nucleation at the intersecting line of two contacting crystals is introduced to describe gibbsite crystal growth. The growth rate equation is derived in the appendix. From this, the relevant growth mechanisms for the individual faces of individual gibbsite crystals are proposed.

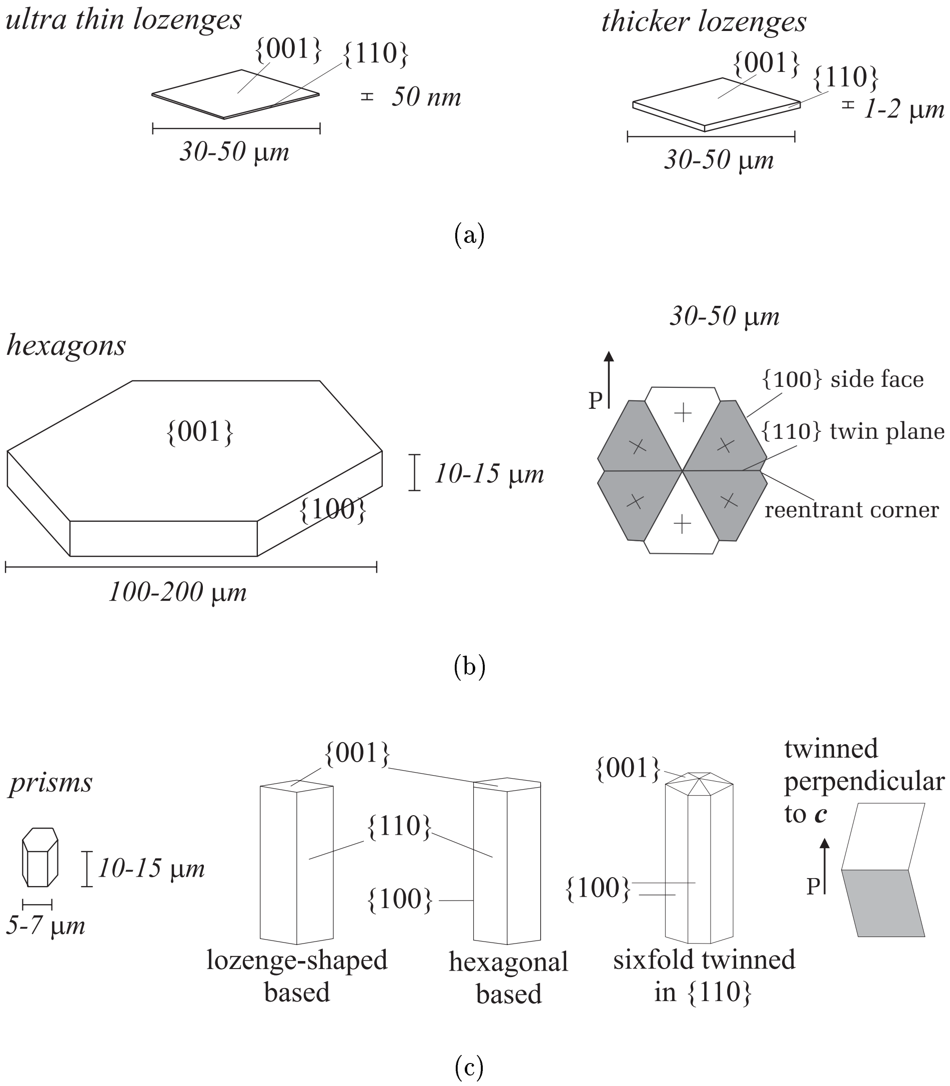

Figure 4.1: Morphologies of different types of gibbsite, γ-Al(OH)$_3$, crystals grown from sodium aluminate solutions under various conditions. For the hexagons also the top view between crossed polarisers is given, showing sixfold twinning.

4.2 Driving force for gibbsite crystallisation

In the literature, several definitions are given for the crystallisation driving force, S, as used in equation 4.1. Some authors [3, 5] proposed to use the difference in the actual aluminium hydroxide concentration in the solution and the equilibrium value, i.e. c-c_{eq}. Veesler et al. [10, 11] suggested to use the normalised supersaturation ratio $\frac{c}{c_{eq}}$ or $\frac{c-c_{eq}}{c_{eq}}$ as a measure for the driving force. These expressions should normalise the supersaturation with respect to the solubility of aluminium hydroxide for different caustic concentrations.

Table 4.1: Definitions for driving forces, S, used in the literature. c and c_{eq} are the actual aluminium hydroxide concentration and the equilibrium value, respectively, expressed in g/l Al_2O_3, C is the caustic concentration expressed in g/l Na_2CO_3 and FC is the free caustic, that is, the total amount of sodium hydroxide minus the amount required to convert aluminium hydroxide to the aluminate ion.

S	Reference
$c - c_{eq}$	[3, 5]
$\frac{c}{c_{eq}}$	[10, 11]
$\frac{c-c_{eq}}{c_{eq}}$	[10, 11]
$\frac{c-c_{eq}}{C}$	[2]
$\frac{c-c_{eq}}{FC}$	[4]
$\sqrt{\frac{\frac{c}{C}-\frac{c_{eq}}{C}^{2}}{C^{0.5}}}$	[6]

More attempts to improve the growth rate relation with respect to the driving force led to definitions of the driving force as presented in table 4.1. In the last three definitions of this table, the driving force is corrected for the presence of active hydroxide ions, which would result in growth rate relations that are independent of the caustic concentration [2, 4, 6]. We will derive an alternative, improved expression for the driving force in this section.

The dimensionless driving force for crystallisation is defined as $\frac{\Delta\mu}{kT}$, where $\Delta\mu$ is the difference in chemical potential of the growth units in the mother phase and in the solid phase, and kT is the thermal energy. The chemical potential of species i is defined as:

$$\mu_i = \mu_i^o + RT \ln a_i, \tag{4.3}$$

where a_i is the activity of the units of species i in the solid or the mother phase. The activity, a_i, is the product of the activity coefficient, γ_i, and the molality of species i, m_i.

For a simple crystallisation process, involving one species i and considering that the activity in the solid equals one, the driving force for crystallisation is given by:

$$\frac{\Delta\mu}{kT} = \ln\frac{a_i}{a_{i,eq}} = \ln\frac{\gamma_i m_i}{\gamma_{i,eq} m_{i,eq}} \approx \ln\frac{\gamma_i c_i}{\gamma_{i,eq} c_{i,eq}}, \tag{4.4}$$

since for the molality m the concentration can be used for not too high concentrations. However, if crystallisation involves a chemical reaction:

$$\mathrm{A_1 + A_2 + ... + A_n \rightleftharpoons S_{cr} + B_1 + B_2 + ... + B_m}, \tag{4.5}$$

with A_i the starting components, B_j the reaction products and S_{cr} the crystalline phase, then:

$$\frac{\Delta\mu}{kT} = \sum_{i=1}^{n} \ln\frac{a_{A_i}}{a_{A_i,eq}} - \sum_{j=1}^{m} \ln\frac{a_{B_j}}{a_{B_j,eq}}. \tag{4.6}$$

Dissolution of gibbsite in caustic solutions leads to the formation of several ions and soluble complexes [12–14]. Single aluminium complexes, like AlO_2^- and $AlO(OH)_2^-$, dialuminium complexes, like $Al_2O(OH)_6^{2-}$ or the double hydroxy complex $Al_2(OH)_8^{2-}$, but also even higher aluminium complexes, like $Al_6(OH)_{24}^{6-}$, are supposed to be formed in sodium aluminate solutions. The driving force for gibbsite crystallisation is determined by the activity of all these possible species related to the crystallisation process. Recent studies showed that most of the dissolved aluminium is present as the aluminate ion, $Al(OH)_4^-$ [15]. Depending on the caustic concentration, this ion is hydrated at low caustic concentration or forms an ion pair with sodium at high caustic concentration [15, 16]. Significant concentrations of other single aluminium complexes, like AlO_2^-, were found to be negligible, although $Al_2O(OH)_6^{2-}$ dimers might be present in the solution [15]. Here, it is assumed that besides $Al(OH)_4^-$, the concentration of all these species is negligible, so that the overall crystallisation process corresponds to the reaction:

$$\mathrm{Al(OH)_4^-(aq)} \rightleftharpoons \gamma\text{–}\mathrm{Al(OH)_3(s)} + \mathrm{OH^-(aq)}. \tag{4.7}$$

Using equation 4.6, it follows that the driving force for gibbsite crystallisation equals:

$$\frac{\Delta\mu}{kT} = \ln\frac{a_{Al(OH)_4^-}}{a_{Al(OH)_4^-,eq}} - \ln\frac{a_{OH^-}}{a_{OH^-,eq}} = \ln\frac{a_{Al(OH)_4^-}}{a_{Al(OH)_4^-,eq}}\frac{a_{OH^-,eq}}{a_{OH^-}} \approx \ln\frac{\frac{\gamma_{Al(OH)_4^-}[Al(OH)_4^-]}{\gamma_{OH^-}[OH^-]}}{\frac{\gamma_{Al(OH)_4^-,eq}[Al(OH)_4^-]_{eq}}{\gamma_{OH^-,eq}[OH^-]_{eq}}}. \tag{4.8}$$

Note that for the molality the concentration is used. Since the activity coefficients of the different ions in the Bayer liquor are not measured and the Debye-Hückel expression is not applicable for these concentrated ionic Bayer liquors, it is assumed that in the region of interest the ratio of the activity coefficients does not change with concentration, i.e. $\frac{\gamma_{Al(OH)_4^-}}{\gamma_{OH^-}} \approx \frac{\gamma_{Al(OH)_4^-,eq}}{\gamma_{OH^-,eq}}$. Then, the driving force is given by:

$$\frac{\Delta\mu}{kT} = \ln\frac{\frac{c}{[OH^-]}}{\frac{c_{eq}}{[OH^-]_{eq}}}, \tag{4.9}$$

where c and c_{eq} are the actual and the equilibrium $Al(OH)_4^-$ concentration of the solution at the crystallisation temperature T, respectively.

Only if $\frac{c}{[OH^-]}/\frac{c_{eq}}{[OH^-]_{eq}}$ is close to unity, the driving force can be approximated by

$$\frac{\Delta\mu}{kT} \approx \sigma = \frac{\frac{c}{[OH^-]} - \frac{c_{eq}}{[OH^-]_{eq}}}{\frac{c_{eq}}{[OH^-]_{eq}}}, \tag{4.10}$$

which is the relative supersaturation. In this relation, the assumption is made that $\ln(1+\sigma) \approx \sigma$, which actually is only valid if σ is small, i.e. if it does not exceed 10%. However, in case of gibbsite crystallisation the supersaturation can exceed 100%.

Since no better information is available on neither the activities nor the relevance of all minor species present in the solution, participating in gibbsite crystal growth, the driving force defined by eq. 4.9 is suggested to be the best possible definition of the gibbsite crystallisation driving force, despite the fact that some assumptions have been made.

4.3 Experimental

4.3.1 ***In-situ*** cell

The *in-situ* growth experiments were done in a growth cell as is represented in figure 4.2. To avoid corrosion by the caustic solution, the cell consists of two, optically flat, sapphire windows 1.5 mm separated by a precise, chemically resistant EPDM O-ring. The windows are clamped by stainless steel flanges, leaving an aperture of 2 cm. The volume of the cell is about 0.5 ml. The cell is heated from its outer wall, in which a coaxial resistance wire, connected to a power supply is mounted.

The temperature for all experiments was 80°C. The temperature of the cell was controlled by a thermocouple mounted on the upper window just below the stainless steal flange, combined with a temperature controller with a stability of ± 0.1°C. Unfortunately, it was not possible to measure the temperature inside the cell during the experiments, since the high caustic concentration of the Bayer liquors would destroy the thermocouple. Using the same set-up filled with water, the temperature in the cell was determined to be almost similar to the temperature measured by the thermocouple. A small difference of less than one degree was present. It is supposed that there is also a temperature difference between the periphery and the centre of the cell. Measurements outside the cell between these two points revealed a difference of less than two degrees, which is explained by the relatively high thermal conductivity of the sapphire windows. This radial temperature gradient is expected to be lower inside the cell, because the heat is more stabilised. As a result of this small temperature difference, some convection is expected to occur in the cell.

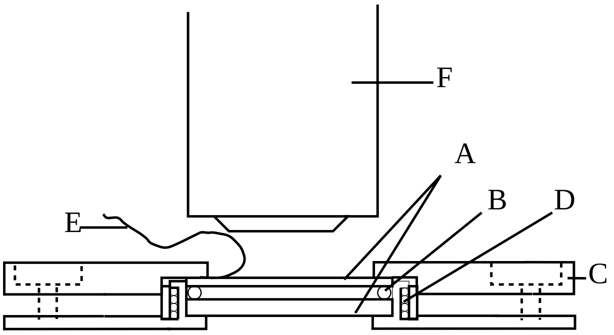

A = Sapphire windows
B = EPDM precise O-ring
C = Stainless steal flange
D = Heater
E = Thermocouple
F = Microscope objective

Figure 4.2: Experimental setup of the *in-situ* cell.

At the beginning of each experiment 0.4 ml Bayer liquor at a temperature of about 60°C was put on the lower sapphire window which was preheated. Here, care was taken that the solution did not contact the O-ring, enabled by the high surface tension of the liquid. After this, the upper window was placed on top. The amount of liquor was chosen such that after closing the cell the liquor contacted both sapphire windows, allowing for a small air bubble to be present. In this way, light scattering from a liquid-air boundary otherwise present was prevented and, in addition, pressure changes, due to the volume changes as a result of the crystallisation process and due to the heating of the liquor, were suppressed by the air bubble. After closing the cell, it took only a few minutes to reach the desired temperature. It is estimated that a temperature difference of ± 2° introduced an error in the driving force calculation of ± 0.06.

4.3.2 Bayer liquors

Pure Bayer liquors were prepared by dissolving aluminium (purity 99.999%) in about 50 ml concentrated sodium hydroxide (p.a.) solutions at 90-100°C in a teflon vessel. After complete dissolution of the aluminium, the solutions were filtered through a Millipore HVLP 0.45 μm filter and diluted with de-ionised water to obtain the desired caustic and aluminate concentration.

Different conditions for gibbsite nucleation and growth were obtained by varying the caustic concentration and the sodium aluminate concentration. Three different caustic concentrations were used, namely $C = 100$, 200 and 300 g/l Na_2CO_3 in terms of the alumina refinery notation. These values correspond to a NaOH molarity of 1.89, 3.77 and 5.66 mol/l respectively. The aluminate to caustic ratio A/C varied from 0.5 - 0.8, where A represents the aluminate concentration expressed in g/l Al_2O_3. The liquor specifications of all experiments are given in table 4.2. For a conversion between the conventional and alumina refinery notation see, e.g., reference [17].

The equilibrium caustic and alumina concentrations were determined using a computer algorithm, which is based on an equation derived by McCoy et al. [18], relating the equilibrium solubility of gibbsite to the temperature, caustic concentration and impurity concentrations of sodium aluminate liquors. The error in the driving force, due to errors in weighing the NaOH and Al pellets, is ± 0.01. This is far less than the ± 0.06 error introduced by an error in temperature in the *in-situ* cell due to a possible temperature gradient between the periphery and the centre of the cell. The series of experiments are referred to their C and A/C values.

4.3.3 Seeds

Both seeded and unseeded growth experiments were done. Seed material was prepared in the *in-situ* cell under similar conditions as the experiments. Crystallites nucleated on the sapphire windows and remained stuck to the window after opening the cell. These crystals were immediately used as seeds in a fresh solution, without washing, drying and without coming into contact with air. In this way, possible effects of surface restructuring (measurable as an induction period prior to nucleation and growth) were reduced to a minimum. As a result of this preparation method, a thin liquid layer remained on the sapphire window and seeds which could have slightly affected the actual aluminate supersaturation. However, the amount of this liquid was so small that its influence is negligible.

Table 4.2: Liquor specifications for the *in-situ* experiments. C is the caustic concentration expressed in g/l Na_2CO_3 and A is the aluminium hydroxide concentration expressed in g/l Al_2O_3. c and c_{eq} are the actual aluminium hydroxide concentration and the equilibrium value, respectively. The temperature for all experiments is 80°C.

C_i g/l Na_2CO_3	$(A/C)_i$	C_{eq} g/l Na_2CO_3	$(A/C)_{eq}$	$\frac{\Delta\mu}{kT} = \ln \frac{\frac{c}{[OH^-]}}{\frac{c_{eq}}{[OH^-]_{eq}}}$ (eq. 4.9)	$\sigma = \frac{\frac{c}{[OH^-]} - \frac{c_{eq}}{[OH^-]_{eq}}}{\frac{c_{eq}}{[OH^-]_{eq}}}$ (eq. 4.10)
100.13	0.500	101.57	0.311	0.82	1.27
103.31	0.597	105.64	0.313	1.22	2.40
100.22	0.599	102.45	0.311	1.24	2.45
100.99	0.679	103.91	0.312	1.61	3.99
101.06	0.683	104.01	0.312	1.63	4.09
104.44	0.694	107.67	0.314	1.68	4.35
100.01	0.698	103.03	0.312	1.71	4.52
100.00	0.700	103.04	0.312	1.72	4.58
96.03	0.714	98.96	0.309	1.80	5.06
197.32	0.479	200.29	0.368	0.47	0.60
197.35	0.515	201.32	0.369	0.62	0.85
198.81	0.529	203.21	0.370	0.67	0.96
201.99	0.592	208.38	0.374	0.93	1.52
200.29	0.599	206.83	0.373	0.96	1.61
205.96	0.628	213.67	0.377	1.07	1.91
205.96	0.628	213.67	0.377	1.07	1.91
198.01	0.692	207.51	0.373	1.40	3.05
198.54	0.697	208.07	0.373	1.42	3.15
199.91	0.699	209.61	0.374	1.43	3.18
200.37	0.699	210.11	0.375	1.43	3.18
200.13	0.701	209.91	0.375	1.44	3.22
207.28	0.738	218.91	0.380	1.62	4.04
200.44	0.796	213.49	0.377	2.01	6.47
200.00	0.800	213.12	0.377	2.04	6.68
200.00	0.801	213.16	0.377	2.05	6.74
298.87	0.487	301.69	0.438	0.21	0.23
300.24	0.598	309.81	0.444	0.65	0.92
299.34	0.697	315.65	0.448	1.11	2.02
298.41	0.697	314.69	0.447	1.11	2.03
303.97	0.701	320.8	0.452	1.11	2.03
300.00	0.700	316.56	0.449	1.12	2.06
302.52	0.783	325.56	0.455	1.58	3.87
300.88	0.799	325.03	0.455	1.70	4.47
300.09	0.800	324.21	0.454	1.71	4.52
300.00	0.800	324.13	0.454	1.71	4.52
298.41	0.806	322.85	0.453	1.76	4.80

4.3.4 Observations and measurements

The growth of the crystals was followed in time using a transmission optical microscope (Olympus Vanox), fitted with a long working distance objective corrected for observation through the window and liquid. Crystal growth rates were determined by capturing images at selected time intervals (typically 10-30 minutes, depending on the growth rate) with a digital video camera connected to a computer. The linear growth rate of the crystal faces was calculated from the increase in crystal size after each time interval, which was measured by determining the distance between two opposite faces of the same type.

For all experiments given in table 4.2 the growth rates of seeds and spontaneously formed nuclei were measured, distinguishing the individual crystal faces. For the single crystalline lozenges, it was shown that the {110} faces dominate the growth morphology, while for the sixfold twinned hexagons, the {100} faces are the most prominent side faces (chapter 2). Therefore, the {100} and basal {001} faces of sixfold twinned hexagons, the {110} and some {100} faces of lozenges and the {001} and side faces of prismatic crystals were examined. For the prisms it was not clear whether the {100} or {110} faces were the side faces. After completing the growth experiments, the crystals were separated from the solution and the occurrence of twinning was verified with polarisation microscopy. This was not possible during the experiments, because the use of single crystalline, birefringent sapphire windows prevented observation of twinning with polarisation microscopy. As expected, this revealed that the larger hexagons were twinned sixfold along the {110} faces. For the prisms, sixfold twinning parallel to the c-axis could not be detected, because viewing the prisms perpendicular to $\boldsymbol{c}$ the separate crystal domains have the same extinction direction. Single twinning parallel to {100} and twinning perpendicular to the c-axis were not observed for prisms in the *in-situ* cell.

In each experiment, usually three to ten crystals of one kind (twinned hexagons, single crystalline lozenges or prisms) were measured in all possible crystallographic directions. It was found that the growth rates of crystal faces were more or less identical for the symmetry equivalent crystal faces of one crystal, but varied a lot between different crystals. The growth rate of each single crystal was, therefore, determined by averaging the growth rates in these equivalent directions. In this way, the error in growth rate for each experiment was estimated from the errors in growth rates of each individual crystal. The error in measuring the increase in size of each crystal was ± 0.35 μm. Depending on the time between each measurement of the crystal sizes, this leads to an error in growth rate of 0.4 - 2.0 μm/h. The measurements perpendicular to the c-axis were somewhat less precise since the crystal boundaries were slightly out of focus. It was found that the dispersion in growth rate of the individual crystals gives rise to fluctuations in growth rate larger than the experimental error. The final growth rates of each type of face were, nevertheless, obtained by averaging over all crystals growing in the same experiment, thus, averaging the effect of growth rate dispersion.

Since the cell consisted of a closed compartment, the overall supersaturation of the solution decreased as nucleation and crystal growth proceeded. As a consequence, the crystal growth rate decreased in time. Because of the small volume of the *in-situ* cell, it was not possible to carry out liquor analysis during and after the experiment. Therefore, only the initial liquor specification was known. The average growth rate at the beginning of each experiment, that is after a short induction period, is used as the actual growth rate corresponding to the growth conditions chosen. As a result of an increase in growth rate at the beginning of the experiments, which will be further described in section 4.4, this value will be slightly too low. It is, however, expected that this deviation is only small and that its effect on the growth rate is less than the other errors of the experiments. The growth rates measured as a function of the driving force are fitted to various growth rate equations using a least square fit method.

4.4 Results

4.4.1 Growth velocity measurements

A typical seeded growth sequence, imaged by *in-situ* optical microscopy, is shown in figure 4.3. The conditions were C = 200 g/l Na_2CO_3, A/C = 0.8 and T = 80°C. The sequence clearly shows the increase in size of the seed crystals in time and simultaneously the formation and growth of new nuclei. The seeds as well as the nuclei formed have either a hexagonal or a lozenge-shaped morphology. The crystals are viewed both parallel and perpendicular to the *c*-axis.

Following these crystals in time and measuring the linear growth rates resulted in typical growth curves as shown in figure 4.4. The error bar is estimated to be about 2 μm/h for each measurement. This diagram represents the growth rates of the {100} faces of two hexagons measured in time in three equivalent <100> directions. From these curves it is clear that the three different <100> directions of each hexagon have more or less identical growth rates, although they fluctuate in time and the crystals mutually vary a lot in growth rate. The thicker curve represents the mean value of measurements of six hexagons of the same experiment, either seeded or freshly nucleated. It should be noted, that on the average the growth rates of the seeds and freshly nucleated crystals did not differ. In general, the growth rate decreased in time, which is expected since the supersaturation decreased in the closed cell system.

During most experiments, after an initial increase the growth rate became maximal and then decreased slowly. This initial increase was observed for seeds as well as for the nuclei formed immediately at the beginning of an experiment. The time of increase depends on the driving force: the higher the driving force the shorter its length. It was independent of the warming-up time of the *in-situ* cell, which took maximally 2 minutes. However, also for this dependency a large dispersion was found. The occurrence of an induction period prior to growth is sometimes explained by surface restructuring of the seed crystals [19]. In that case, however, nuclei freshly formed should not show this effect. One may speculate, therefore, that the induction period corresponds with the time of solution restructuring, necessary for growth, which still takes place after raising the temperature of the cell to the experimental value.

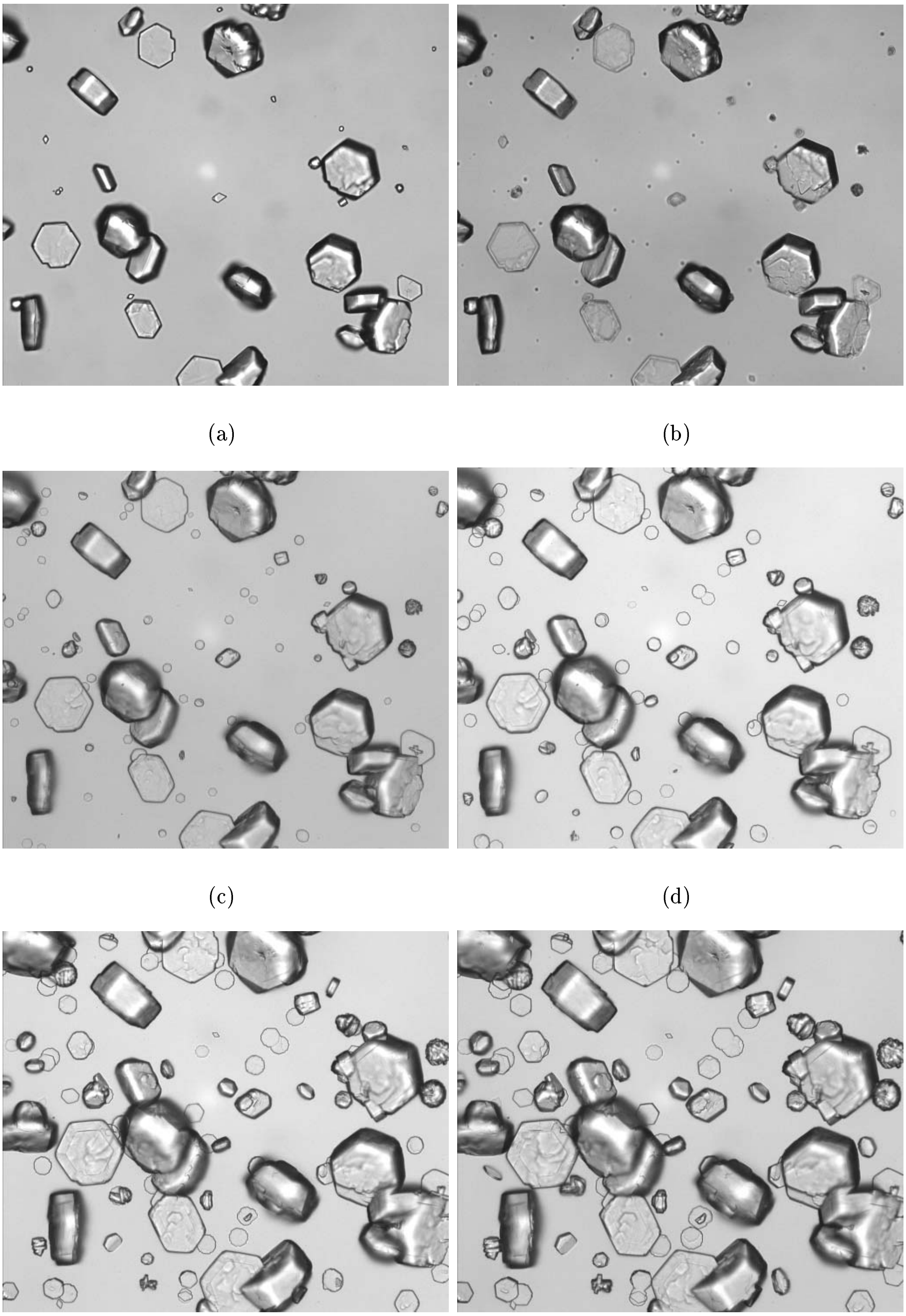

(a) (b)

(c) (d)

(e) (f)

Figure 4.3: Growth sequence of gibbsite crystals for conditions C = 200 g/l Na_2CO_3 and A/C = 0.8. The linear size of the images is 400 μm and Δt= 10, 20, 35, 55, 95 and 135 minutes, relative to the starting time t_0. In this sequence, seed crystals grow to larger crystals. The seeds are mainly hexagonally shaped, but also lozenges are observed. In addition, the formation of new nuclei can be seen. These nuclei are also hexagonal as well as lozenge shaped.

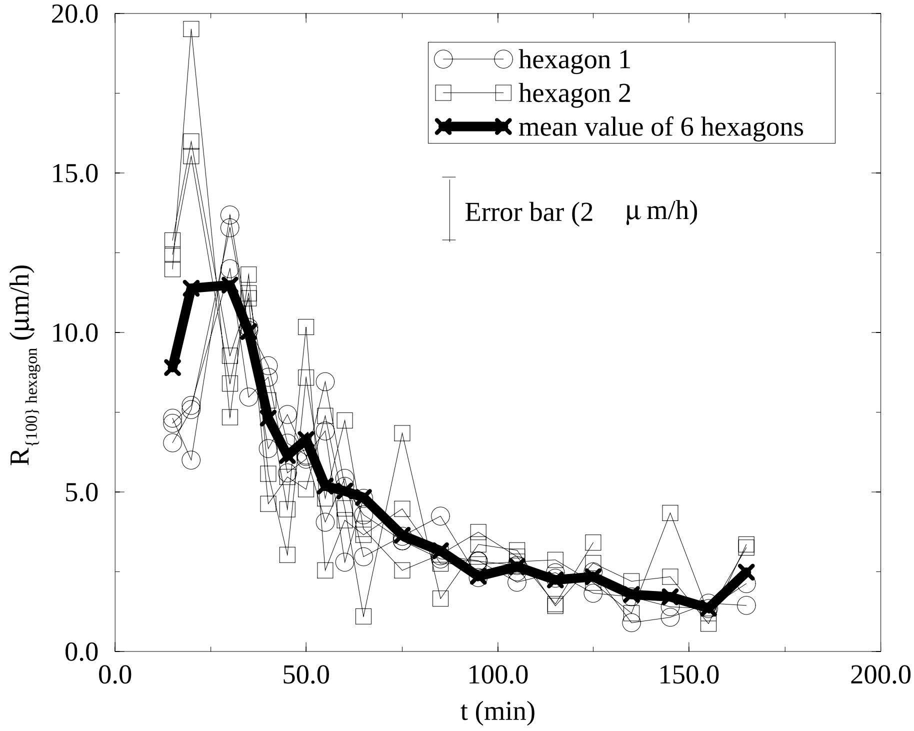

Figure 4.4: Typical growth rates of {100} side faces of hexagons in one experiment versus time for C = 200 g/l Na_2CO_3 and A/C = 0.8. The numbers 1 and 2 refer to the growth rates of two hexagons each measured along the three equivalent <100> directions. The thick line refers to the mean value of six hexagons, either seeded or freshly nucleated. The growth rate decreases in time, although at the beginning of the experiment an increase can be seen. Another characteristic is that the three faces of each hexagon show similar fluctuations of the growth rate in time.

Figure 4.5 shows the average linear growth rates of individual faces of the gibbsite single crystal faces as a function of the driving force, expressed as $\frac{\Delta\mu}{kT} = \ln\frac{\frac{c}{[OH^-]}}{\frac{c_{eq}}{[OH^-]_{eq}}}$ (eq. 4.9). Each point corresponds with an individual *in-situ* run. As was explained in the experimental section, the maximum value of the average growth rate curve of each run was chosen as the actual growth rate belonging to the growth conditions concerned. In fig. 4.5d and e the growth rate data of King for which C varied from 120 - 220 g/l Na_2CO_3 are also presented [4].

Some general trends can be recognised. The figure indicates that higher growth rates are obtained at higher supersaturation. Further examination of the growth rates shows that large variations in average crystal growth rates are obtained for different gibbsite crystals under identical conditions, but in different experiments. In general, the growth rate for the different faces follows the sequence: $R_{\{100\},hexagon} > R_{\{110\},lozenge} > R_{\{001\},hexagon}$. This behaviour in growth rate of faces corresponds to the results of chapter 2, in which the morphological importance of the faces was found to follow $\mathrm{MI}_{\{001\}} > \mathrm{MI}_{\{110\}} > \mathrm{MI}_{\{100\}} > \mathrm{MI}_{\{112\}} \approx \mathrm{MI}_{\{101\}}$. The growth rates of the {100} and side faces of prismatic crystals measured by King are similar to our growth rates measured for the {100} faces of the hexagons. However, the growth rates obtained for prismatic crystals in the <001> and lateral directions were smaller in our case. The results obtained by Lee et al. [9] differ from our results, which is possibly due to the fact that they measured relative growth rates.

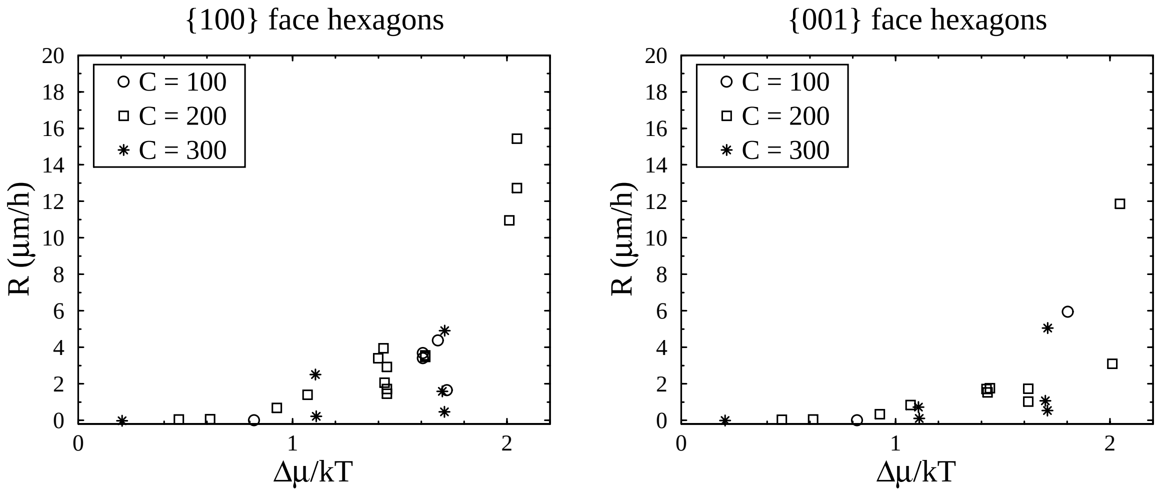

(a) (b)

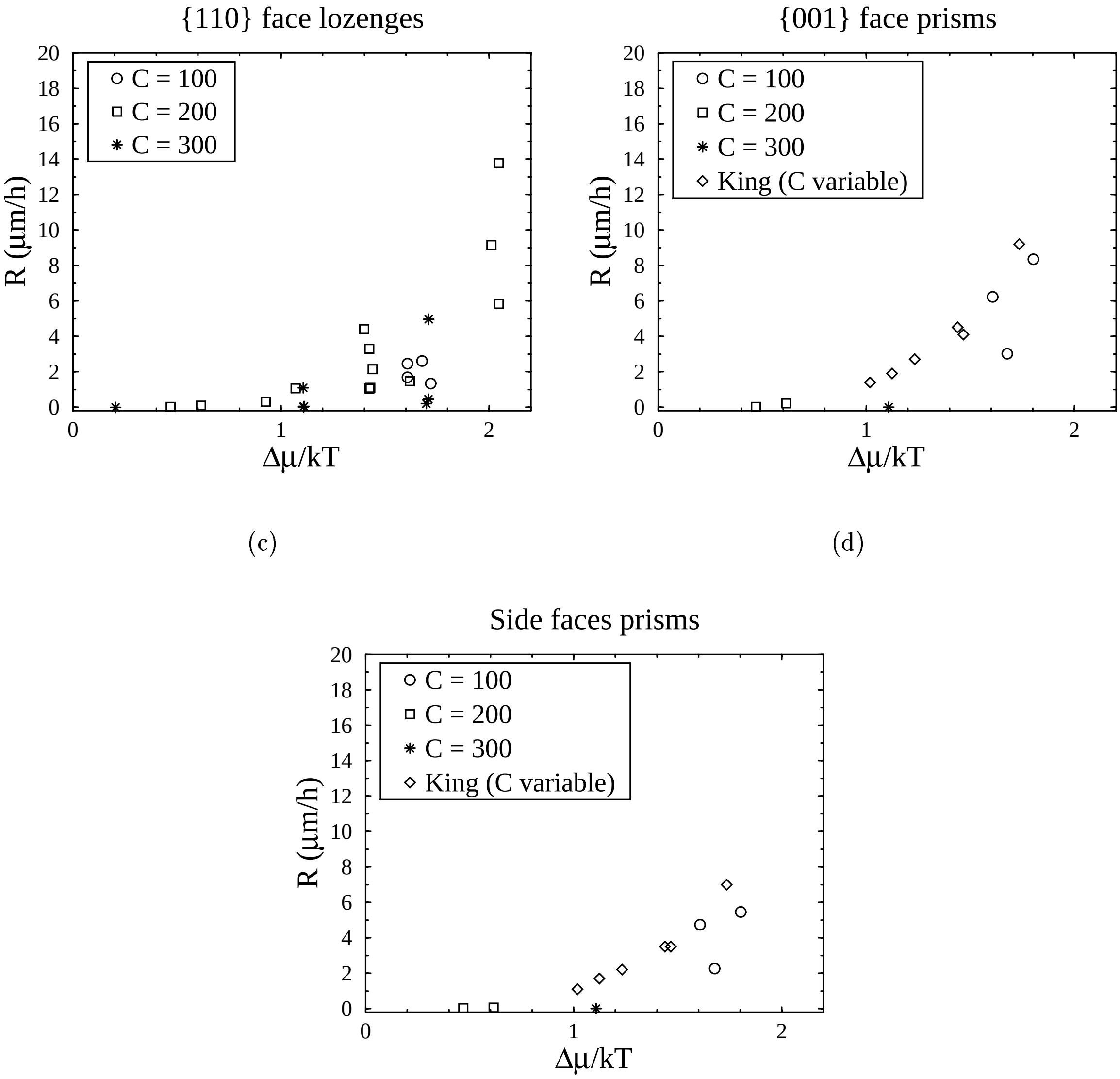

(c)

(d)

(e)

Figure 4.5: The linear growth rates of gibbsite crystal faces versus $\frac{\Delta\mu}{kT}$ as defined in eq. 4.9, for (a) the {100} and (b) the {001} faces of hexagons, (c) the {110} faces of lozenges, and (d) the {001} and (e) the side faces of prisms. It is not clear whether the side faces of the prisms were {110} or {100} faces. It should be noted that each point in the graphs does not correspond with the growth rate of a particular crystal, but is the growth rate of the face in a given crystallographic direction averaged over several crystals in one experiment. In graphs (d) and (e) the data of King [4] are also represented.

4.4.2 Characteristic features

Observations reveal that at low driving force lozenge-shaped crystals became truncated by the appearance of small {100} faces. At high driving force these faces grew relatively faster and lozenges were formed again. This implies that at low driving force the linear growth rate of the {100} faces is slightly smaller than $\sqrt{3}$ times the linear growth rate of the {110} faces, while at higher driving force the linear growth rate of {100} becomes dominant. The formation of non-twinned hexagonal crystals is the result of equal growth rates in the <110> and <100> directions. Such crystals have been observed, but were rare. A cross-over point at low driving force for the growth rates of {100} and {110} faces as sketched in figure 4.6 is theoretically possible, resulting in hexagons elongated along ***b***.

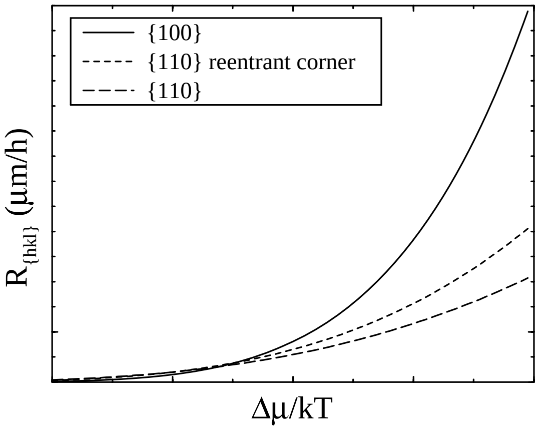

Figure 4.6: Schematic view showing the linear growth rate as a function of the driving force in the [110] and [100] direction of single crystalline gibbsite crystals, as deduced from the changing morphology of lozenge-shaped crystals at different supersaturation. The growth rate curve for the {110} faces at the reentrant corners of the sixfold twinned hexagons is also presented.

Another interesting growth phenomenon is shown in figure 4.7. It shows a sixfold twinned hexagonal seed with reentrant corners. The growth mechanism of such twinned hexagons is the combination of fast growing {100} faces and a twin plane reentrant corner induced 2D nucleation growth of the adjacent {110} faces (see chapter 2). In this sequence, it is shown that the reentrant corners become smaller in time. Hence, at the beginning, when the supersaturation is higher, the growth rate of the {100} faces is faster than the growth rate of the {110} faces induced by 2D nucleation growth at the reentrant corners. Later on in the experiment, when the supersaturation is decreased, the growth rate of the {100} side faces becomes comparable to that of the adjacent {110} faces. When the reentrant corner is almost vanished, the growth rate ratio of the {100} side faces and the advancement rate of the reentrant corner is exactly 2:$\sqrt{3}$, as concluded from geometrical considerations. In other words, the growth rate of the associated {110} faces is identical

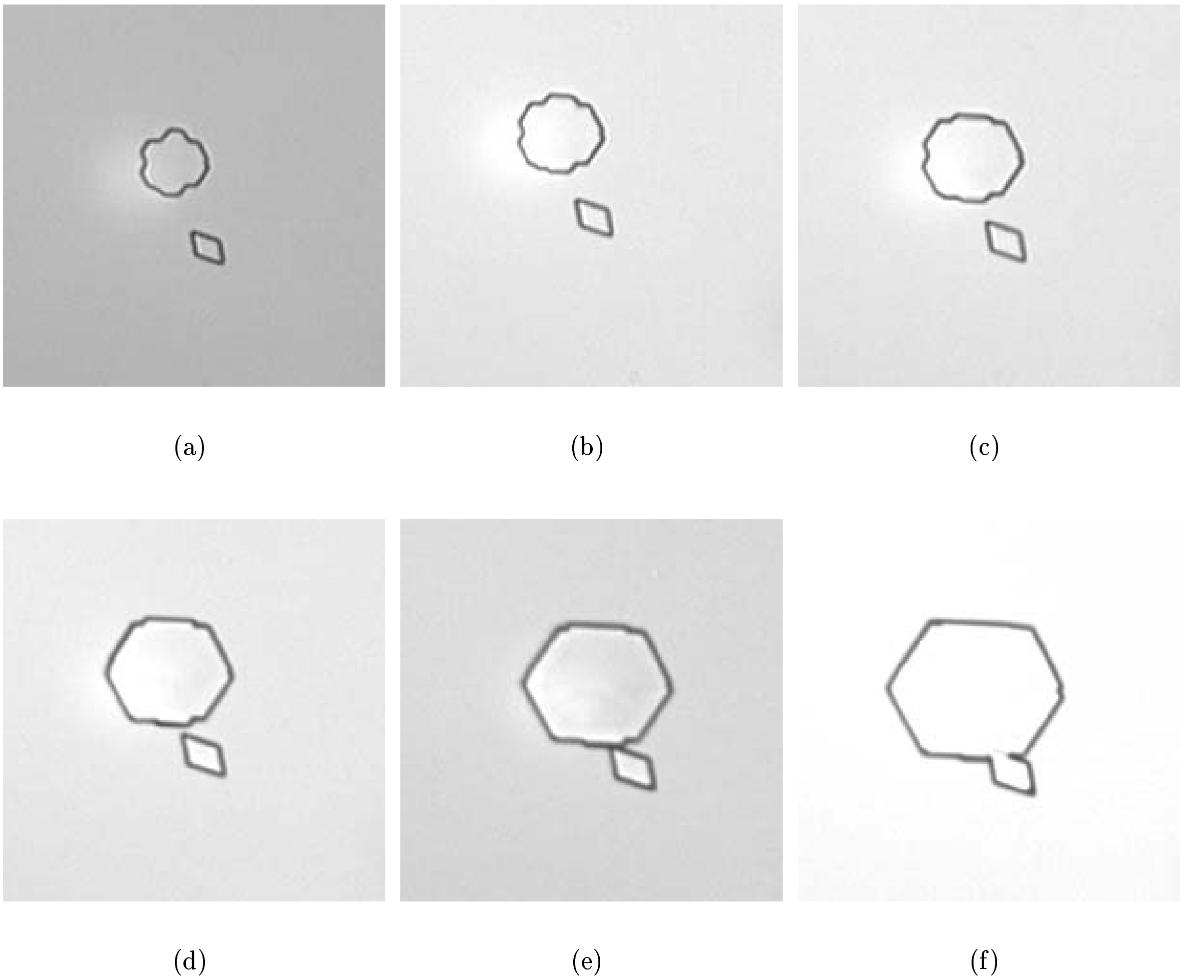

(a) (b) (c)

(d) (e) (f)

Figure 4.7: Growth sequence of a sixfold twinned hexagon with reentrant corners at C = 200 g/l Na_2CO_3 and A/C = 0.8. The time sequence is (a) 0h, (b) 1h, (c) 2h, (d) 4h, (e) 6h, and (f) 9h. The width of the reentrant decreases in time. This suggests that at lower supersaturation, i.e. after longer time, the crystal growth mechanism induced by the reentrant corner becomes more important relative to the growth at the {100} side faces. The size of the pictures is 80x80 μm.

to that of the {100} faces. In figure 4.6, a possible growth rate curve of the {110} faces adjacent to reentrant corners relative to the growth rate of the {100} and 'normal' {110} faces is also presented.
Note that the {110} side faces of the adjacent lozenge grow at a much reduced rate. This remarkable difference in growth rate between the {100} and {110}, i.e. 1.0 versus 0.1 μm/h respectively, was not observed in other experiments.

4.5 Discussion

4.5.1 Crystal growth rate dispersion

The aim of this study is to find the relation between the growth rate of a gibbsite crystal face and the driving force. In general, it is assumed that the crystal growth rate is only determined by the driving force, and that there is an unambiguous relationship between crystal growth rates and the driving force for each face $\{hkl\}$. However, in case of the crystallisation of gibbsite it is observed that the crystal growth rates can differ as much as 100% for crystals in the same experiment and that these fluctuate fairly in time, despite the fact that the temperature of the cell is constant. This can also not be explained by a local fluctuation in driving force due to heat or mass transport, since it is supposed that gibbsite crystal growth is surface reaction controlled [3, 20] and the overall driving force is supposed to be constant everywhere in the cell, only decreasing in time. Furthermore, the average crystal growth rates differ a lot under apparently identical crystallisation conditions. A small part of the variation in growth rate can be explained by errors in determining $\frac{\Delta\mu}{kT}$ and in measuring the crystal sizes; the remaining part must be real variations in growth rates of crystals. It is estimated that the error in determining the driving force is ± 0.06, which is mainly caused by a temperature gradient in the cell. The error in crystal growth rate measurements is 0.4-2 μm/h. The variation in growth rate of different crystals and in time within one and different experiment(s) is clearly larger than 2 μm/h, indicating that the dispersion of crystal growth is not induced by the inaccuracy of the measurements, but indeed is related to physical properties of the crystals or of the solution. The observation of crystal growth dispersion as an intrinsic characteristic of the material is supported by other studies of crystallising compounds including gibbsite [7, 9]. These variations seem to increase at higher temperature and higher driving force [7], which is also the case in our experiments.

According to classical theories [7], crystal growth rate dispersion can be explained by (1) size-dependent growth related to a Gibbs-Thomson effect, (2) the variation in number and activity of dislocation step sources at the crystal surface, (3) the overall lattice strain of crystals, or (4) impurity effects.

The Gibbs-Thomson effect suggests that if growth is controlled by a surface integration mechanism, small crystals grow more slowly than larger crystals. This effect is explained by a difference in solubility [7]. According to this model, the size dependent growth is only relevant for crystals with sizes close to the size of a critical nucleus, because the effective driving force experienced by the crystals is given by:

$$\Delta\mu_{eff} = \Delta\mu_{app}\left(1 - \frac{r_c}{r}\right). \tag{4.11}$$

In this equation, $\Delta\mu_{app}$ is the applied driving force, r the size of a crystal and r_c the size of a 3D critical nucleus. If the size of a critical nucleus is about 1.2 nm, as suggested by Rossiter et al. [21], the observed crystals larger than 1 μm lead to a $\Delta\mu_{eff}$ that approximates $\Delta\mu_{app}$ and, thus, this size effect is negligible for gibbsite crystal growth. Screw dislocation growth and other step generating defects can also induce size dependent growth. If the surface area is larger, the probability of the occurrence of defects on the surface – specifically the probability of dislocations with a high burgers vector – is also larger and this will result in higher growth rates. Both these size-dependent growth mechanisms suggest that the growth rate is constant for crystals of the same material, same size and under identical growth conditions. Some authors proposed a size-dependent growth mechanism for gibbsite crystallisation [9], whereas others did not observe any size dependent growth [3]. The latter corresponds with our observations, where also crystals of the same size have different growth rates which, in addition, fluctuate in time.

The cause of growth rate dispersion for gibbsite possibly lies in the changing activity of dislocations or of a group of dislocations emerging at the surface during crystal growth. An alternative may be the deposition of micro crystallites on the crystal surface leading to varying rates of step generation by contact nucleation. On the other hand, it is observed that the faces of one crystal have the same fluctuation behaviour which would suggest that the growth rate dispersion is more related to local solution specifications. One may speculate that solvent restructuring as part of the growth mechanism leads to dispersions in growth rates [14,19]. Another factor influencing crystal growth is the presence of small amounts of impurities at the growing interface. These particles can adsorb on the surface and influence the step flow on crystal surfaces. This can finally lead to discontinuous growth, even followed by periods of stagnation. In addition, point defects may result in microscopic lattice stress centres which may cause disorder (mosaicity) of crystals and retardation or cessation of growth. The study described in chapter 3 have shown that in gibbsite crystals many defects are present which also result in different step sources on crystal surfaces, stress and even mosaicity. It was also proposed in chapter 2 that impurities have a large influence on the gibbsite growth mechanism. However, the results of the present study can not lead to a decisive conclusion concerning the cause of the growth rate dispersion.

4.5.2 Relevant growth rate equations

Influence of caustic concentration on growth rate

In figure 4.5 the results of the average growth rates are plotted versus the applied driving force defined by $\frac{\Delta\mu}{kT} = \ln\frac{\frac{c}{[OH^-]}}{\frac{c_{eq}}{[OH^-]_{eq}}}$. Using this definition, there is still no independence of the growth rate on the caustic concentration. The data suppose that the caustic concentration is still involved, despite the fact that its effect is taken into account in the driving force as defined in eq. 4.9. If the driving force would be expressed as $\frac{\Delta\mu}{kT} = \ln\frac{c}{c_{eq}}$, the scatter in the experimental data points would become larger. Deviations are particular present for the linear growth rates measured at C = 300 g/l Na_2CO_3 as compared to lower caustic concentration, but there is no systematic trend. These deviations can be due to errors at high caustic concentration and high driving force. Firstly, massive nucleation took place in the cell, making it impossible to determine the growth rates of individual crystals properly. This problem also prevented growth rates measurements when the driving force exceeded $\frac{\Delta\mu}{kT} = 0.76$ at C= 300 g/l Na_2CO_3. Secondly, the equilibrium concentrations for the aluminate ion and sodium hydroxide are not well known at high caustics, since the equation predicting these equilibrium concentrations is based on intermediate concentrations and extrapolation to higher or lower concentrations may lead to apparent errors. More important is the expected change in activity and ionic strength of the solution species at varied caustic concentrations. This may be accompanied by a change in solution species present in the solution. Compared to the very high caustic concentrations, the data points for the low C (100 g/l Na_2CO_3) are better. The growth rates measured in this study are the most reliable for the {100} faces of the hexagons and the {110} faces of the lozenges at C = 200 g/l Na_2CO_3. Therefore, these data are used to determine the crystal growth mechanism in the next section. The data points measured for the prisms were not used, because of the little amount. Instead, the data points of King [4] are used to analyse the growth mechanism for prisms.

Relevant growth mechanisms

In the field of industrial crystallisation, the $\boldsymbol{R}(\frac{\Delta\mu}{kT})$ dependence is usually approximated by the power law form:

$$\boldsymbol{R} = k_0 S^p, \tag{4.12}$$

where p is the kinetic order and k_0 is the kinetic coefficient. If the results presented in figure 4.5 are fitted to this equation with $S = \frac{\Delta\mu}{kT} = \ln \frac{\frac{c}{[OH^-]}}{\frac{c_{eq}}{[OH^-]_{eq}}}$, then the kinetic order p varies from 4.5 to 6.7. The values of p and k obtained for the different faces are presented in table 4.3. If for S $\sigma = \frac{\frac{c}{[OH^-]} - \frac{c_{eq}}{[OH^-]_{eq}}}{\frac{c_{eq}}{[OH^-]_{eq}}}$ is used, for the {100} faces of the hexagons, the {110} faces of the lozenges and the {001} and {side} faces of Kings crystals p is about 2. This would suggest that spiral growth is the plausible mechanism for gibbsite crystallisation. However, the equation $\boldsymbol{R} = k_0 S^2$ for spiral growth is only valid at low supersaturation, which is usually not applied in gibbsite crystallisation. Furthermore, the growth mechanism can not be described by the above quadratic equation, since the definition of the driving force $\sigma = \frac{\frac{c}{[OH^-]} - \frac{c_{eq}}{[OH^-]_{eq}}}{\frac{c_{eq}}{[OH^-]_{eq}}}$ is not the correct one, as concluded the previous section. Moreover, the growth rate as described by eq. (4.12) is semi-empirical and does not necessarily describe any realistic growth mechanism.

It is well-known that the growth rate of crystals can be controlled by transport processes, i.e. mass transport of growth units from the solution towards the crystal surface. In case of gibbsite crystallisation this is not the rate limiting crystallisation step, because of the slow growth rates of gibbsite even if the solution is agitated well. In addition, diffusion controlled growth is proportional to the difference between the actual and equilibrium solute concentration, c-c_{eq}, which is certainly not the case regarding the curves in figure 4.5. Therefore, surface integration rather than mass transport is expected to control gibbsite crystal growth. This agrees with the conclusions as reported in the literature, which were deduced from the very low growth rate (a few μm/h), the square law relationship between the growth rate and supersaturation (i.e. if $S = \sigma$), the high activation energy for growth and the negligible effect of agitation on the growth rate [3, 20]. If transport

Table 4.3: Values of k in [μm/h] and p in the function $\boldsymbol{R} = kS^p$ obtained from a standard fit procedure, where S is $\frac{\Delta\mu}{kT} = \ln \frac{\frac{c}{[OH^-]}}{\frac{ceq}{[OH^-]_{eq}}}$, or is $\sigma = \frac{\frac{c}{[OH^-]} - \frac{ceq}{[OH^-]_{eq}}}{\frac{ceq}{[OH^-]_{eq}}}$.

Face {hkl}	$\frac{\Delta\mu}{kT}$		σ	
	k	p	k	p
{100} hexagon	0.14	6.37	0.16	2.32
{001} hexagon	0.10	6.14	0.02	3.16
{110} lozenge	0.08	6.65	0.18	2.09
{001} prism	0.30	5.57	0.77	7.80
{side} prism	0.36	4.54	0.07	1.58
King {001} prism	1.11	3.80	0.42	1.99
King {side} prism	1.00	3.51	0.40	1.84

is not relevant, mononuclear and polynuclear two-dimensional (2D) nucleation can dominate gibbsite growth, but also a dislocation mechanism is possible. Examination of the surfaces of gibbsite crystals by optical and atomic force microscopy reported in chapter 3 demonstrated that the {001} faces of sixfold twinned hexagons grow by a combined dislocation and contact nucleation mechanism as do the {001} faces of prisms. In that study, two kinds of lozenges have been distinguished: *ultra thin* lozenges and *thicker* lozenges of which {001} basal faces grow by a 2D nucleation and a dislocation mechanism, respectively. The {110} side faces of both types of lozenges turned out to grow by a polynuclear birth and spread mechanism. The {100} side faces of the hexagons and prisms grow by a polynuclear birth and spread mechanism, while the growth of the side faces of prisms was suggested to be related to impurities or stress due to mosaicity formation. A mononuclear birth and spread mechanism is very unlikely in the above cases, because the surfaces are relatively large and the AFM topographic studies indicated polynuclear birth and spread.

Growth rate equations

If growth is controlled by a polynuclear birth and spread mechanism, according to Nielsen the growth rate equation at higher driving force $\Delta\mu$ is given by [7,8]:

$$\boldsymbol{R}_p = A_1 \left(\exp \left(\frac{\Delta\mu}{kT} \right) \right)^{7/6} \left(\exp \left(\frac{\Delta\mu}{kT} \right) - 1 \right)^{2/3} \left(\frac{\Delta\mu}{kT} \right)^{1/6} \exp \left(\frac{-A_2}{\Delta\mu/kT} \right), \quad (4.13)$$

with A_1 and A_2 constants that are independent of the driving force. If growth of a crystal face is associated with crystal dislocations, the rate of growth is expressed by [22]:

$$\boldsymbol{R}_d = B_1 \left(\exp \left(\frac{\Delta\mu}{kT} \right) - 1 \right) \frac{\Delta\mu}{kT} \tanh \left(\frac{B_2}{\Delta\mu} \right), \quad (4.14)$$

with B_1 and B_2 independent of $\frac{\Delta\mu}{kT}$. If the driving force for crystallisation is small then the tanh-term equals 1, the term $\left(\exp\left(\frac{\Delta\mu}{kT}\right) - 1\right)$ approximates $\frac{\Delta\mu}{kT}$ and R_d becomes proportional to the square of the driving force. This parabolic law is only valid at low supersaturation, where the surface diffusion fields of adjacent spiral steps do not overlap.

An important step source for gibbsite crystallisation is contact nucleation introduced by misoriented crystallites at the surface. In order to derive an expression for growth by contact nucleation, the theory for multiple birth and spread nucleation is applied to a linear edge, which presents the intersection line of the foreign crystallite and the growing crystal surface. The complete derivation is given in the appendix. The main result is the equation:

$$\boldsymbol{R}_c = C_1 \left(\exp\left(\frac{\Delta\mu}{kT}\right) - 1 \right)^{1/2} \exp\left(\frac{\Delta\mu}{kT}\right) (\Delta\mu)^{-1/2} \exp\left(\frac{-C_2}{\Delta\mu}\right), \qquad (4.15)$$

where C_1 is a constant and $C_2 = \frac{\gamma_s^2 \Omega^{2/3}}{2(kT)} \left(\theta - \frac{1}{2}\sin(2\theta)\right)$. The explicit expressions of the constants used in this section are given in the list of symbols at the end of this chapter.

4.5.3 Fit procedure and discussion

The growth rate expressions for crystal growth determined by a birth and spread mechanism, dislocation growth and contact nucleation, as given by the equations 4.13, 4.14 and 4.15, were used in order to find which growth mechanism is most plausible for the individual faces of gibbsite crystal growth. In figure 4.8 the curve fitting results for the three growth mechanism equations are presented for the {100} faces of hexagons, {110} faces of lozenges and the {001} and side faces of King's prismatic crystals. The data fit to some extent to the spiral growth mechanism, but a far better fit was found for the birth and spread mechanism according to equation 4.13 and the equation for the contact nucleation growth mechanism (eq. 4.15) derived in this chapter. For the faces of different crystal types, the curves have roughly the same pattern. Some data points deviate from the curve. Besides crystal growth rate dispersion, this can also be the result of the occurrence of a different growth mechanism for a few individual cases. The results are compatible with the surface topography data available for the different faces. The {001} faces of the sixfold twinned hexagons and prisms were found to grow by a multiple dislocation and a contact nucleation mechanism. The curve fitting suggests that the latter controls the overall growth rate. As the fits suggests, the {110} side faces of the lozenges, the {100} side faces of the sixfold twinned hexagons and the side faces of prisms are controlled by a polynuclear birth and spread or contact nucleation mechanism. This agrees with the conclusions from our previous AFM study.

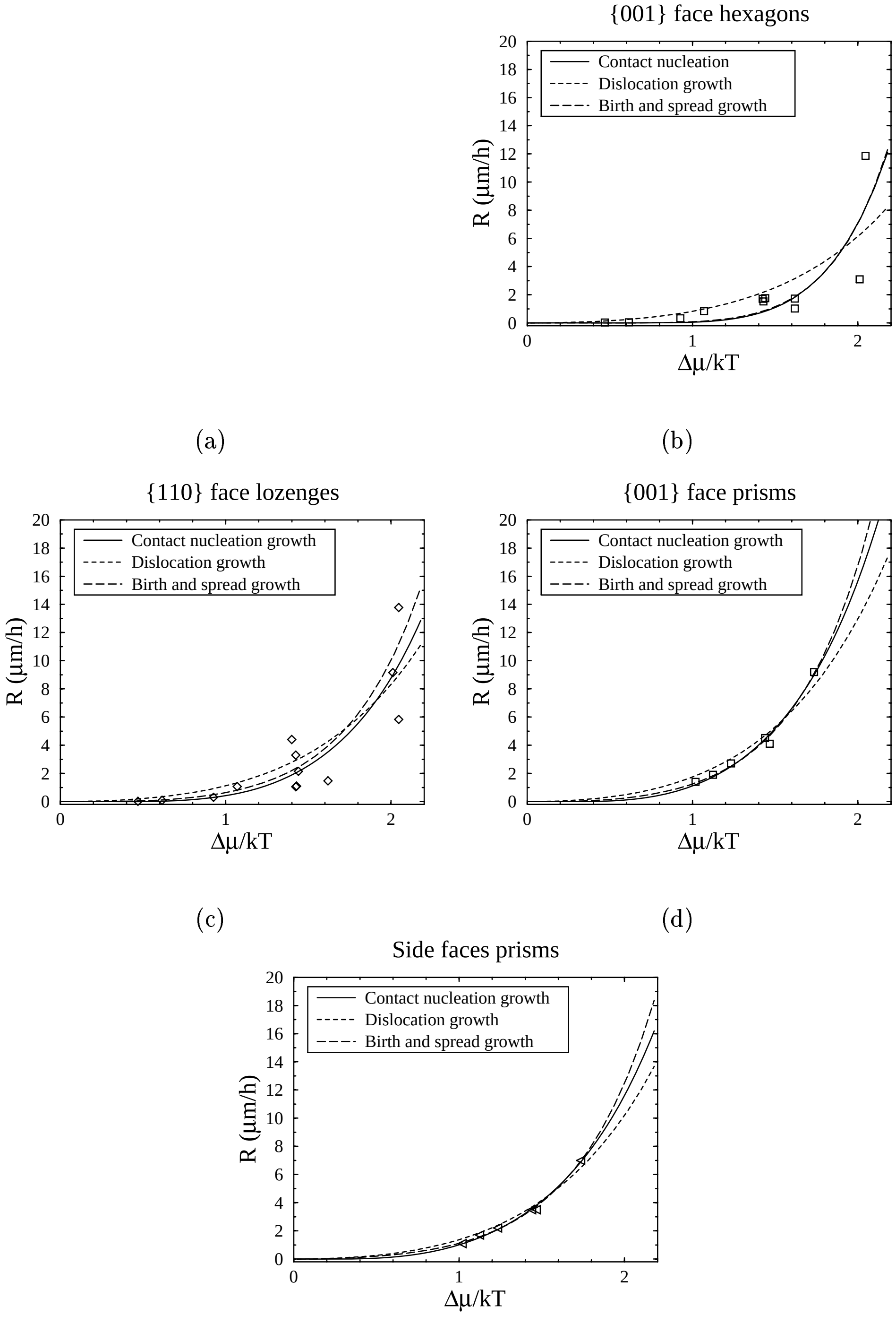

(a) (b) (c) (d) (e)

Figure 4.8: Curve fitting for (a) the {100} and (b) the {001} faces of hexagons, (c) the {110} faces of lozenges, and (d) the {001} and (e) the side faces of prisms. In all cases, C = 200 g/l Na_2CO_3 and T = 80°C. The best fits are contact nucleation growth at linear step edges and birth and spread growth mechanism. For the curve fitting of prismatic gibbsite crystals ((d) and (e)), the data of King [4] are used.

4.5.4 Estimation of the edge free energy, γ_s

Analysing the dependence of the growth rates R of crystals as a function of the driving force $\frac{\Delta\mu}{kT}$ does not lead to a definite conclusion on the actual growth mechanism of gibbsite. The edge free energy estimated from the fits may reveal which of the two mechanisms, 2D birth and spread or 2D contact nucleation, is plausible. The edge free energy is related to the growth rate $\boldsymbol{R}_d$ and $\boldsymbol{R}_c$ through the constants A_2 and C_2. The relationship between A_2, C_2 and γ_s is described by

$$A_2 = \frac{\beta\gamma_s^2\Omega^{4/3}}{3(kT)^2}, \tag{4.16}$$

and

$$C_2 = \frac{\gamma_s^2\Omega^{4/3}}{2(kT)^2}\left(\theta - \frac{1}{2}\sin(2\theta)\right). \tag{4.17}$$

In both equations, γ_s is in [J/m^2]. The values of A_2 and C_2 were obtained from the fit procedure. The volume of the growth unit, Ω, was calculated as $\frac{1}{8}$ of the unit cell volume and the geometrical factor, β, is taken equal to one. Further, it is assumed that $\left(\theta - \frac{1}{2}\sin(2\theta)\right) \approx 1$, or $\theta \approx 73°$, which agrees with the hemi-spherical step patterns introduced by contact nucleation, as imaged with AFM (chapter 3). The calculated edge free energies γ_s at 80°C for the {100} and the {001} faces of the hexagons, the {110} faces of the lozenges, the {001} and side faces of King's crystals, and the {001} and side faces of Lee's crystals are listed in table 4.4. For all faces, the γ_s values are in the order of 0.03-0.1 J/m^2. The order is similar to that estimated by Lee et al. [9] (6.0 ± 1.5 kJ/mol). Table 4.4 also shows that γ_s is higher for {001} than for {110} and {100}. This means that the basal {001} face is the most stable, since γ_s is supposed to be proportional to the slice energy of the crystal. This agrees with the relative Morphological Importance of gibbsite faces found in chapter 2 and 3. Given these data, the order of the {100} and {110} faces would, however, be reversed. It is still not possible to conclude which growth mechanism controls gibbsite growth.

Table 4.4: Edge free energies [J/m^2], calculated from the constants A_2 and C_2, obtained by fitting the measured growth rates.

Face {hkl}	γ_s, A_2	γ_s, C_2
hexagon {100}	0.081	0.102
hexagon {001}	0.125	0.130
lozenge {110}	0.058	0.090
{001} King	0.031	0.073
side faces King	0.059	0.079
{001} Lee	0.050	0.057
side faces Lee	0.079	0.079

4.6 Conclusions

In this study, *in-situ* optical microscopy was used to measure the growth rate of individual crystal faces – i.e. {001}, {110}, and {100} – of different types of gibbsite crystal. A significant growth rate dispersion was observed for similar {*hkl*} faces of crystals of the same type within one experiment, in time and between experiments, despite the fact that they were grown under the same external conditions.

To determine the dependence of the – average – growth rate of the different forms {*hkl*} of crystals of the same type on the driving force, we have derived a definition of the driving force adapted for gibbsite crystallisation from caustic aluminate solution. Furthermore, besides the well-known crystal growth models for birth and spread and spiral growth, a new analytical model for contact nucleation is introduced.

Fits of the growth rates observed using the analytical expressions for birth and spread, spiral growth and contact nucleation revealed that for all different faces, birth and spread and contact nucleation are the most probable growth mechanisms. This is in accordance with earlier surface topography studies.

From the fitted data, the edge free energies have been determined. They are consistent with the morphological importance of the several faces, i.e. $\mathrm{MI}_{001} > \mathrm{MI}_{side faces}$ as observed in chapter 2 and 3 and as will be calculated in chapter 6.

List of symbols

a_i	activity of species i
A	alumina concentration expressed in g/l Al_2O_3
A_1	$D\Omega^{1/3} c_{i,eq}^{2/3}$, eq. (4.13)
A_2	$\frac{\beta\gamma_s^2\Omega^{4/3}}{3(kT)^2}$ with γ_s in [J/m^2], eq. (4.13)
A_i	starting components, eq. (4.7)
B_1	$\frac{h_{st}^2 v_0}{4\pi\gamma_s\Omega}$, eq. (4.14)
B_2	$\frac{\pi\gamma_s\Omega}{h_{st}^2\chi_s}$, eq. (4.14)
B_j	reaction products, eq. (4.7)
c	actual $Al(OH)_3$ concentration in solution at crystallisation temperature T
c_{eq}	equilibrium $Al(OH)_3$ concentration in solution at crystallisation temperature T
c_i	actual concentration of species i in solution at crystallisation temperature T
$c_{i,eq}$	equilibrium concentration of species i in solution at crystallisation temperature T
C	caustic concentration expressed in g/l Na_2CO_3
c_{r^*}	concentration of critical nuclei along a critical edge, eq. (4.24)
C_1	$h_{st}c_{eq}\left(2\theta\gamma_2\Omega^{2/3}v_0 g(\theta)\frac{kT}{h}\exp\left(\frac{\Delta G^{\neq}}{kT}\right)\right)^{1/2}$, eq. (4.15)
C_2	$\frac{\gamma_2^2\Omega^{4/3}}{2(kT)}\left(\theta - \frac{1}{2}\sin(2\theta)\right)$, eq. (4.15)
C_A	$\left(\theta - \frac{1}{2}\sin 2\theta\right)$, eq. (4.19)
C_B	$2\gamma_2\theta + 2(\gamma_1 - \gamma_3)\sin(\pi - \theta)$, eq. (4.19)
C_C	$2\theta\gamma_2\Omega^{\frac{2}{3}}c_{eq}\left(\frac{kT}{h}\right)\exp\left(\frac{\Delta G^{\neq}}{kT}\right)$, eq. (4.26)
D	surface diffusion coefficient
E	activation energy for 2D nucleation
FC	free caustic: total amount of sodium hydroxide minus the amount required to convert aluminium hydroxide to the aluminate ion
$g(\theta)$	geometrical factor
ΔG^*	critical free activation energy, eq. (4.23)
$\Delta G^{\neq}$	free activation energy
ΔG_{tot}	total free energy
$\Delta G_{surface}$	free energy of the surface
ΔG_{edge}	free energy of the edge
h	Planck's constant
h_{st}	height of a monomoleculair step
I	rate of formation of critical nuclei per site along a linear edge, eq. (4.25)
k	Boltzmann constant in J/K
k_0	kinetic coefficient
kT	thermal energy
L	length of the linear edge covered by a 2D nucleus, eq. (4.28)
m_i	molality of species i

N	possible positions for nuclei along the linear edge
p	kinetic order, eq. (4.12)
r	radius of a crystal or nucleus
r_c	critical radius of a 3D nucleus
r^*	critical radius of a 2D nucleus, eq. (4.22)
R	gas constant in [J/K mol]
$\boldsymbol{R}$	crystal growth rate
$\boldsymbol{R}_c$	crystal growth rate resulting from contact nucleation at linear edges, eq. (4.15) and derived in the appendix
$\boldsymbol{R}_d$	crystal growth rate according to a dislocation mechanism, eq. (4.14)
$\boldsymbol{R}_p$	crystal growth rate according to a polynuclear birth and spread mechanism, eq. (4.13)
S	crystallisation driving force
S_{cr}	crystalline phase, eq. (4.7)
t	time
T	crystallisation temperature
v_0	$\frac{2f_0 D\beta c_{i,eq}}{kT\chi_s}$
$v_{st,//}$	step velocity parallel to the linear edge
β	geometrical factor
γ_1	edge free energies of the boundary between nucleus and edge
γ_2	edge free energies of the boundary between nucleus and mother phase
γ_3	edge free energies of the boundary between edge and mother phase
γ_i	activity coefficient of species i
γ_s	step energy
σ	relative supersaturation, eq. (4.10)
θ	contact angle of a 2D nucleus with a linear edge
μ_i	chemical potential of species i
μ_i^o	standard chemical potential of species i
$\Delta\mu$	difference in chemical potential of the growth units in solution and in solid phase
$\Delta\mu_{app}$	applied driving force
$\Delta\mu_{eff}$	driving force experienced by the crystals
Ω	volume of a growth unit
χ_{st}	mean path length of surface diffusion
τ	time, eq. (4.29)
v_c	probability of adding a growth unit to an existing critical nucleus

Appendix

In this appendix, we derive an expression for the growth of a crystal face, for which the steps are generated by multiple 2D contact nucleation at the intersection line of a foreign body with the crystal surface. The essentials of the model are shown in figure 4.9. It is assumed that individual nuclei are constantly formed along the contact line, because of a lowering of the 2D nucleation barrier. These nuclei coalescence to steps that propagate away from this linear edge. We first derive the frequency of 2D nucleation per edge site, followed by calculation of the rate of step creation using a one-dimensional version of the birth and spread nucleation model.

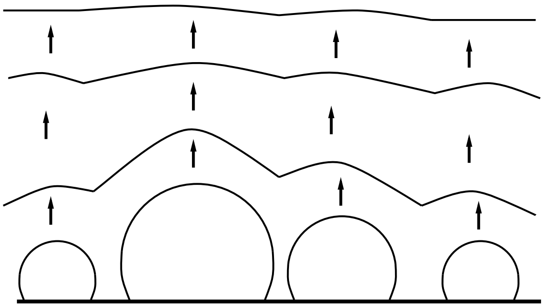

Figure 4.9: Step generation by 2D contact nucleation from a linear edge.

Consider a 2D nucleus contacting a linear edge with an angle θ, as is shown in figure 4.10. The total free energy for creating this nucleus equals

$$\Delta G_{tot} = \Delta G_{surface} + \Delta G_{edge}, \tag{4.18}$$

or

$$\Delta G_{tot}(r) = -\frac{\Delta\mu}{\Omega^{2/3}} r^2 C_A + rC_B, \tag{4.19}$$

with $C_A = \left(\theta - \frac{1}{2}\sin 2\theta\right)$ and $C_B = 2\gamma_2\theta + 2(\gamma_1 - \gamma_3)\sin(\pi - \theta)$. In this equation γ_1, γ_2 and γ_3 are the edge free energies of the boundaries between nucleus-edge, nucleus-mother phase and edge-mother phase, respectively. $\Delta\mu$ is the driving force for growth and Ω is the volume of a growth unit. Using Young's equation (see also figure 4.10),

$$\gamma_3 = \gamma_1 + \gamma_2 \cos\theta, \tag{4.20}$$

C_B becomes equal to $2\gamma_2\left(\theta - \frac{1}{2}\sin 2\theta\right)$, or $C_B = 2C_A\gamma_2$. Now equation (4.19) becomes

$$\Delta G_{tot}(r) = C_A\left(-\frac{\Delta\mu}{\Omega^{2/3}} r^2 + 2\gamma_2 r\right). \tag{4.21}$$

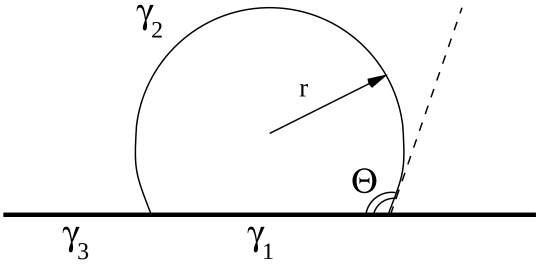

Figure 4.10: 2D nucleus in contact with a linear edge on a crystal surface. The symbols γ_1, γ_2 and γ_3 are the edge free energies of a the nucleus-edge, nucleus-mother phase and edge-mother phase boundary, respectively.

Differentiating $\Delta G_{tot}(r)$ with respect to r and putting this equal to zero gives the critical radius for 2D nucleation,

$$r^* = \frac{\gamma_2 \Omega^{2/3}}{\Delta\mu}, \tag{4.22}$$

which is identical to the critical radius for homogeneous nucleation. Subsequently, the barrier for 2D nucleation, which corresponds to the maximum value of $\Delta G_{tot}(r)$, can be evaluated as

$$\Delta G^* = \frac{\gamma_2^2 \Omega^{2/3}}{\Delta\mu}\left(\theta - \frac{1}{2}\sin 2\theta\right). \tag{4.23}$$

Now, we assume that a 2D nucleus only expands if its radius exceeds the critical nucleus r^*. Using Boltzmann statistics, it follows that the concentration of critical nuclei along the critical edge is given by

$$c_{r^*} = c_{eq}\exp\left(\frac{\Delta\mu}{kT}\right)\exp\left(\frac{-\Delta G^*}{kT}\right), \tag{4.24}$$

where c_{eq} is the equilibrium concentration of the solute in the liquid. If one growth unit is added to a critical nucleus, it becomes supercritical and will expand. From this, it follows that the rate of nucleation per site along the linear edge equals

$$I = v_c c_{r^*}. \tag{4.25}$$

Here, v_c is the probability of adding a growth unit to an existing critical nucleus. The probability is given by the product of the concentration of growth units in the liquid, $c_{eq}\exp\left(\frac{\Delta\mu}{kT}\right)$, their probability of entering to the step of the nucleus, $\left(\frac{kT}{h}\right)\exp\left(\frac{\Delta G^{\neq}}{kT}\right)$, and the circumference of the nucleus, excluding the contact line with the linear edge, $2\theta r^*$. This leads to

$$v_c = C_C \exp\left(\frac{\Delta\mu}{kT}\right)(\Delta\mu)^{-1}, \tag{4.26}$$

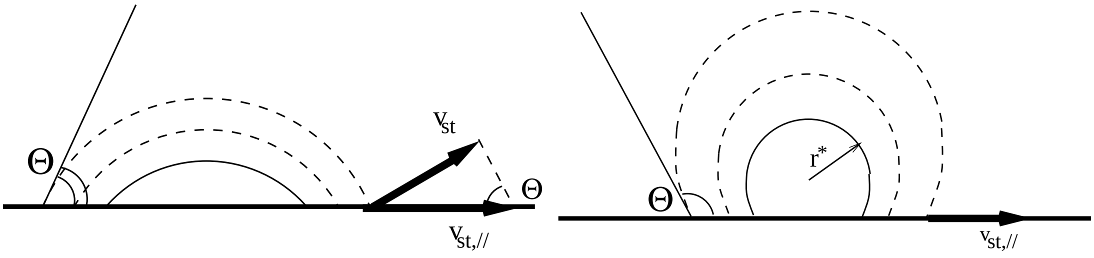

(a) (b)

Figure 4.11: Step movement from a supercritical nucleus along a linear edge; (a) $\theta < 90°$: $v_{st,//} = \frac{v_{st}}{\sin\theta}$, (b) $\theta > 90°$: $v_{st,//} \approx v_{st}$.

with $C_C = 2\theta\gamma_2\Omega^{\frac{2}{3}}c_{eq}\left(\frac{kT}{h}\right)\exp\left(\frac{\Delta G^{\neq}}{kT}\right)$. Combining (4.24), (4.25) and (4.26) gives the rate of nucleation

$$I = C_C c_{eq}\left(\exp\left(\frac{2\Delta\mu}{kT}\right)\right)(\Delta\mu)^{-1}\exp\left(\frac{-\Delta G^*}{kT}\right). \tag{4.27}$$

Using the 2D nucleation frequency per step site as derived above, we now calculate the rate of step generation using a one-dimensional version of the birth and spread model. The length of coverage of the linear edge by a 2D nucleus formed at time t_1 is at time t_2 equal to

$$L_{t_2} = 2v_{st,//}(t_2 - t_1), \tag{4.28}$$

with $v_{st,//} = g(\theta)\,v_{st}$, the step velocity parallel to the linear edge. The geometrical factor, $g(\theta)$, depends on the contact angle θ. As shown in figure 4.11a, for $\theta < 90°$ $v_{st,//} = \frac{v_{st}}{\sin\theta}$, i.e. $g(\theta) = \frac{1}{\sin\theta}$. For $\theta > 90°$, the situation is more complex, but as shown in figure 4.11b, $g(\theta)$ can be approximated to 1.

If there are N positions along the linear edge, a new, complete step is generated at time τ, which satisfies

$$\int_0^{\tau} NIL(\tau - t)dt = N. \tag{4.29}$$

Here, NI is the formation frequency of critical nuclei on the total length of the linear edge. Combining (4.28) with (4.29) and solving the integral, one obtains

$$\tau = \left(Iv_{st,//}\right)^{-1/2}. \tag{4.30}$$

The growth rate, R_d, induced by contact nucleation is the product of the frequency of step generation, τ^{-1}, times the step height, h_{st}, or

$$R_c = h_{st}\left(Iv_{st,//}\right)^{1/2}, \tag{4.31}$$

with $v_{st,//} = v_0\left(\exp\left(\frac{\Delta\mu}{kT}\right) - 1\right)g(\theta)$. Finally, combining equations (4.23), (4.27) and

(4.31) an explicit expression for the growth rate induced by contact nucleation is obtained,

$$R_c = h_{st}\left(C_C c_{eq}\exp\left(\frac{2\Delta\mu}{kT}\right)(\Delta\mu)^{-1}\exp\left(\frac{-\Delta G^*}{2kT}\right)\right)^{1/2}\left(v_0\left(\exp\left(\frac{\Delta\mu}{kT}\right)-1\right)g\left(\theta\right)\right)^{1/2}, \tag{4.32}$$

or more compact

$$R_c = C_1\left(\exp\left(\frac{\Delta\mu}{kT}\right)-1\right)^{1/2}\exp\left(\frac{\Delta\mu}{kT}\right)(\Delta\mu)^{-1/2}\exp\left(\frac{-C_2}{\Delta\mu}\right), \tag{4.33}$$

with C_1 and C_2 constants, independent of the driving force, equal to $C_1 = h_{st}c_{eq}\left(2\theta\gamma_2\Omega^{2/3}v_0 g(\theta)\frac{kT}{h}\exp\left(\frac{\Delta G^{\neq}}{kT}\right)\right)^{1/2}$, and $C_2 = \frac{\gamma_s^2\Omega^{2/3}}{2(kT)}\left(\theta - \frac{1}{2}\sin\left(2\theta\right)\right)$. If the edge free energy is expressed as J/m^2 instead of J/m, then C_2 becomes $C_2 = \frac{\gamma_s^2\Omega^{4/3}}{2(kT)}\left(\theta - \frac{1}{2}\sin\left(2\theta\right)\right)$.

References

[1] A.E. Nielsen, J. Cryst. Growth 67 (1984) p. 289.

[2] T.G. Pearson, The chemical background of the aluminium industry (Royal Institute of Chemistry, London, Monograph no. 3, 1955).

[3] C. Misra and E.T. White, Chem. Eng. Prog. Symp. Series 110 67 (1971) p. 53.

[4] W.R. King, Light Metals (1973) p. 551.

[5] A. Halfon and S. Kaliaguine, Can. J. Chem. Eng. 54 (1976) p. 160.

[6] E.T. White and S.H. Bateman, Light Metals (1988) p. 157.

[7] O. Söhnel and J. Garside, editors, Precipitation (Butterworth-Heinemann, Oxford, 1992).

[8] A.E. Nielsen, Theory of electrolyte crystal growth, In S.J. Jančić and P.A.M. Grootscholten, editors, *Industrial Crystallization* p. 35–52, Delft University Press (1984).

[9] M.-Y. Lee and G. Parkinson, J. Cryst. Growth 198/199 (1999) p. 270.

[10] S. Veesler and R. Boistelle, J. Cryst. Growth 130 (1993) p. 411.

[11] S. Veesler and R. Boistelle, J. Cryst. Growth 142 (1994) p. 177.

[12] J. Zambo, Light Metals (1986) p. 199.

[13] P. Sipos, S.G. Capewell, P.M. May, G. Hefter, G. Laurenczy, F. Lukács and R. Roulet, J. Chem. Soc. Dalton Trans. (1998) p. 3007.

[14] C. Vernon, G. Parkinson and D. Lau, Proc. of the Fifth International Alumina Quality Workshop (1999).

[15] T. Radnai, G.T. Hefter and P. Sipos, J. Phys. Chem. 102 (1998) p. 7841.

[16] J.A. Tossell, Am. Min. 84 (1999) p. 1641.

[17] S. Veesler, S. Roure and R. Boistelle, J. Cryst. Growth 135 (1994) p. 505.

[18] B.N. McCoy and J.L. Dewey, Light Metals (1982) p. 173.

[19] P. Smith and G. Woods, Light Metals (1993) p. 113.

[20] N. Brown, J. Cryst. Growth 12 (1972) p. 39.

[21] D.S. Rossiter, P.D. Fawell, D. Ilievski and G.M. Parkinson, J. Cryst. Growth 191 (1998) p. 525.

[22] W.K. Burton and N. Cabrera, J. Physics, U.S.S.R. 9 (1945) p. 392.

Chapter 5

Morphology, evolution and other characteristics of gibbsite crystals grown from pure and impure aqueous sodium aluminate solutions

C. Sweegers, H.C. de Coninck, H. Meekes, W.J.P. van Enckevort
I.D.K. Hiralal and A. Rijkeboer [1]

Abstract

The effect of external conditions on the growth morphology of gibbsite, γ-Al(OH)$_3$, grown under a range of conditions has been studied. The results show that during growth the morphology of gibbsite crystals evolves from thin, rounded hexagons and faceted lozenges into faceted plates and blocks with well-formed basal, prismatic and chamfered faces. This morphology evolution shows only a weak dependence on the growth conditions. Moreover, increasing the driving force or the caustic concentration leads to larger crystals, up to tens to a hundred μm in size. The influence of small amounts of inorganic impurities on the growth of gibbsite crystals turns out to be negligible. Different growth morphologies are obtained from potassium and cesium hydroxide solutions. This indicates that the alkali ions of the solution have a major influence on the morphology of gibbsite. The twinning behaviour is similar for gibbsite crystals grown from sodium, potassium or cesium aluminate solutions.

---

[1] The work in this chapter has been submitted to *J. Cryst. Growth.*

5.1 Introduction

The growth morphology of gibbsite agglomerates is an important topic in the industrial crystallisation of this material, because it has a large impact on a number of properties related to the slurry and the dry product. Gibbsite is industrially crystallised in a complicated system involving high caustic concentrations and the presence of many impurities. In crystal growth research, most attention is usually paid to ideal model systems, neglecting 'difficult' systems such as gibbsite growth. Therefore, the study of the morphology and, especially, the cause of habit modification of these crystals is of interest for both industry and crystal growth science.

5.1.1 Gibbsite morphology

In general, gibbsite shows a very large dispersion in growth morphology and crystal size when grown from synthetic caustic soda solutions. In previous studies (chapter 2 and 3), three major gibbsite crystal morphologies were distinguished, which were even found simultaneously in the same experiment. Their shape and their twinning characteristics are presented in figure 4.1. The first group of morphologies are the single crystalline lozenges bounded by {001} top and {110} side faces. The ultra thin lozenges exhibit the basic growth morphology of defect free gibbsite, which is completely determined by a 2D nucleation mechanism. The thicker ones grow by a spiral mechanism on the {001} faces. The two other growth morphologies – the large tabular hexagons parallel to the {001} basal face and the prismatic crystals – are formed as a result of twinning, impurities or defects generated during the nucleation phase and subsequent growth. For the description of the twinning and the indices of the faces we refer to chapter 2, for the growth characteristics to chapter 3 and 4. The previous studies established that the morphological importance of the gibbsite crystal faces follows the sequence: $\mathrm{MI}_{\{001\}} \gg \mathrm{MI}_{\{110\}} > \mathrm{MI}_{\{100\}} > \mathrm{MI}_{\{101\}} \approx \mathrm{MI}_{\{112\}}$. The aberrant width of the prismatic form is probably due to a retardation of growth by mosaicity and impurity blocking.

As will be described in this chapter, also other gibbsite habits were found in addition to the three main groups. Theses are truncated lozenges, block-shaped crystals intermediate between plates and rods and crystals with {101} and {112} chamfered faces.

5.1.2 Impurities

Impurities can play an important role in the poisoning of surfaces by blocking the active growth sites and, thus, inhibiting their growth. In chapter 2, it was suggested that the growth of the side faces of gibbsite prisms is inhibited by impurity blocking, resulting in a rod-like morphology. Gibbsite crystal growth is known to be inhibited by compounds derived from the humic matter in the starting bauxite ore [1]. Furthermore, these organic compounds can cause surface roughening, loss of chamfered faces, thinning of crystals to form plates or elongating to form prisms. Therefore, many studies have been reported on the nature of specific organic compounds in Bayer liquors and their effect on the different stages in gibbsite crystallisation from synthetic sodium aluminate solutions [2–11].

Only a few studies have been devoted to the influence of inorganic impurities on the crystallisation of gibbsite from sodium aluminate solutions. Brown [12] studied the effect of copper ions on the gibbsite crystallisation using scanning electron microscopy. He found that copper ions preferentially adsorb on the {001} faces of the seed crystals and further induce secondary nucleation, mainly on the prismatic faces. The roughened seed surfaces and the tiny crystallites thereon would promote agglomeration during the crystallisation process. He also studied the effect of calcium ions on the agglomeration of gibbsite and concluded that small amounts of calcium ions in the caustic aluminate solution can lead to enhanced agglomeration of gibbsite particles [13]. The effect of iron atoms was studied by Veesler et al. [14]. The authors suggested that gibbsite growth is blocked at low supersaturations by impurity adsorption without specifying specific surfaces, resulting in a dead zone.

The solvent used profoundly affects the gibbsite crystal habit. Elongated pseudo-hexagonal prisms are formed by growth from potassium aluminate solutions [15]. These morphologies were also found by Lee et al. [16]. The reason for this change in morphology is not well understood.

5.1.3 Aim of this study

In previous chapters, the growth phenomena leading to the rich variety of morphologies and the large dispersion in growth rate of gibbsite crystals grown from caustic aluminate solutions were described. Particularly, the influence of the defect structure was mentioned. This led to a broad investigation of gibbsite growth for a wide range of driving forces, caustic concentrations and growth times, to study the effect of external conditions on the occurrence of different growth mechanisms and, thus, on the morphology and size of gibbsite crystals. Special attention was given to the effect of external conditions on the dispersion in morphology and growth rate. The appearance of possible polymorphs was also taken into account. A second objective is to characterise the influence of inorganic impurities as well as the replacement of sodium by potassium and cesium in the caustic solutions used on the growth morphology and purity of gibbsite crystals.

5.2 Experimental

5.2.1 Crystal growth and *ex-situ* characterisation

To examine the growth morphology of gibbsite, crystals were nucleated and grown from concentrated sodium aluminate solutions for different caustic concentrations and driving forces in stainless steel or teflon crystallisation vessels, similar as was described earlier in chapter 2. The aqueous sodium aluminate solutions, referred to as synthetic Bayer liquors, were prepared by dissolving pure aluminium (purity 99.999%) into a 300 ml hot, caustic soda solution (p.a.) in a teflon beaker under continuous stirring. After filtration through a Millipore HVLP filter (0.45 μm), the solutions were diluted with de-ionised water to the desired volume and then divided into 6 growth vessels, each with an equal volume of 50 ml. The vessels were closed and placed into a thermostatic bath at a temperature of 80°C, while stirring. The axial rotator with 30 rpm ensured that the solutions were agitated well. No seed crystals were used in the experiments.

The crystallisation conditions were varied by changing the caustic concentration and the driving force. The specifications of the starting liquors are given in table 5.1. The caustic concentration was varied between C = 100, 200 and 300 g/l Na_2CO_3, corresponding with 1.89, 3.77 and 5.66 mol/l NaOH, respectively. The aluminate to caustic ratio A/C varied from 0.4 - 0.8, with A representing the aluminate concentration expressed in g/l Al_2O_3. For a conversion between the conventional and alumina refinery notation (A, C) see, e.g., reference [14]. The solutions presented in this table were all free from high levels of impurities, normally present in plant liquors, to determine properly the dependence of the morphology on the growth conditions.

The driving force for crystallisation is defined by the equation (chapter 4):

$$\frac{\Delta\mu}{kT} = \ln \frac{\frac{c}{[OH^-]}}{\frac{c_{eq}}{[OH^-]_{eq}}}, \tag{5.1}$$

where c is the actual concentration and c_{eq} the equilibrium concentration of gibbsite in the caustic soda solution at the crystallisation temperature. $[OH^-]$ and $[OH^-]_{eq}$ are the actual sodium hydroxide and equilibrium concentrations, respectively. The equilibrium concentrations were calculated using the computer algorithm 'Molal', which is based on an equation derived by McCoy et al. [17], fitted to the solubility curve of Misra [18].

To monitor the crystallisation process in time, gibbsite growth was allowed to take place for different growth times for each of the six vessels, as indicated in table 5.1. This

Table 5.1: Liquor specification for the gibbsite crystallisation experiments from pure solutions. C is the caustic concentration expressed in g/l Na_2CO_3 and A is the aluminium hydroxide concentration expressed in g/l Al_2O_3. c and c_{eq} are the actual aluminium hydroxide concentration and the equilibrium value, respectively. The temperature for all experiments was 80°C.

C_i g/l Na_2CO_3	$(A/C)_i$	C_{eq} g/l Na_2CO_3	$(A/C)_{eq}$	$\frac{\Delta\mu}{kT} = \ln \frac{\frac{c}{[OH^-]}}{\frac{c_{eq}}{[OH^-]_{eq}}}$ (eq. 5.1)	Growth time h
100	0.4	100.67	0.31	0.40	6.5, 12.25, 24, 48, 96, 168
100	0.5	101.43	0.31	0.82	6, 12, 24, 48, 72, 192
100	0.6	102.22	0.31	1.24	6, 19, 24, 48, 96, 168
100	0.7	103.04	0.31	1.72	5, 10, 24, 48, 96, 166
200	0.53	204.45	0.37	0.67	6.5, 12, 24, 48, 96, 168
200	0.6	206.55	0.37	0.96	6, 12, 24, 48, 96, 168
200	0.7	209.73	0.37	1.43	15, 24, 48, 72, 96, 168
200	0.8	213.12	0.38	2.04	3, 5.5, 12, 24, 45.5, 95
300	0.5	303.53	0.44	0.25	12, 24, 48
300	0.6	309.69	0.44	0.66	3.4, 9, 24, 53, 99, 168
300	0.7	316.56	0.45	1.12	12, 24, 48
300	0.8	324.13	0.45	1.71	3, 5.5, 22, 29.5, 50, 96

was achieved by stopping crystal growth for the six vessels of one experiment each at a different time. It has to be noted that the induction period prior to crystallisation can be different for the different vessels. A difference in induction period leads to a difference in actual crystal growth time, which gives errors when analysing the crystallisation process in time. Furthermore, the driving force for crystallisation decreases upon continued crystallisation, which rate is apparently different for the different vessels. The reason for the different induction periods is unclear. Therefore, one should be careful in comparing the results of the six vessels of one experiment.

After termination of growth, the crystals were carefully separated from the supersaturated solution, according to the procedure described earlier in chapter 3 to minimise any shut-off effect. The crystals were examined *ex-situ* using scanning electron microscopy (SEM, High Resolution Jeol 600F) and optical differential interference contrast microscopy (DICM). X-ray powder diffraction and Raman spectroscopy were used to verify whether gibbsite or another $Al(OH)_3$ polymorph was formed.

5.2.2 Impurity addition

Additional experiments were done to determine the influence of inorganic impurities on the gibbsite morphology. Small amounts of metal hydroxides (Cu^{2+}, Pb^{2+}, Ba^{2+} and Mg^{2+}) were added to aluminate solutions of C = 200 g/l Na_2CO_3 and A/C = 0.65. Sodium salts of SO_4^{2-}, NO_3^-, CO_3^{2-} and PO_4^{3-} were added to determine the influence of negatively charged impurities. The influence of iron ions on the growth morphology of gibbsite was also investigated: it turned out that experiments done in stainless steel vessels resulted in orange coloured solutions, clearly indicating the leaching of Fe^{2+} from the vessel walls. In table 5.2, the kind and amount of impurities used are given. The impurities were added to the solution before filtration to remove possibly undissolved impurity compounds from the solution. In the case of $Cu(OH)_2$, black insoluble copper oxide was removed, leaving the blue-coloured cuprate II ion, $Cu(OH)_4^{2-}$. For all impurity experiments, the growth time was 48 hours. To determine the amount of impurities present in the crystalline material, analytical methods like Ion Coupled Plasma (ICP) and Atomic Absorption Spectroscopy (AAS) were used to measure the bulk concentration, and Electron Dispersive X-ray Spectroscopy (EDS or Edax) was used to determine the presence of impurities with a resolution of 1 μm^3 just below the surface of the crystals. In calculating the driving force, the influence of impurities on the solubility of gibbsite and consequently on the driving force was not taken into account.

The influence of alkali atoms on the growth morphology of gibbsite was investigated by growing crystals from potassium and cesium aluminate solutions. These solutions were prepared by dissolving aluminium in potassium hydroxide or cesium hydroxide solutions. The preparation method was the same as described above. The alkali concentrations are C = 200 expressed in equivalent g/l Na_2CO_3 and A/C 0.4 and 0.6, with the aluminium hydroxide concentration in g/l Al_2O_3. The temperature for all experiments was 80°C. The equilibrium concentration of gibbsite in potassium and cesium hydroxide solutions are not known; as an approximation it is assumed that these are the same as for the sodium solutions. The growth time was 24h.

Table 5.2: Specification of the kind and amount of impurities added to the sodium aluminate solutions of C = 200 g/l Na_2CO_3 and A/C = 0.65. The temperature for all experiments is 80°C, the driving force $\frac{\Delta\mu}{kT} = 1.20$. The growth time is 48h. The amount of iron ions added was not known since its source was the stainless steel growth vessel.

Impurity	Amount in mg/l
$Cu(OH)_2$	180, 635
$Pb(OH)_2$	160
$Ba(OH)_2$	300, 390
$Mg(OH)_2$	420
Fe^{3+}	?
Na_2SO_4	440, 565
$NaNO_3$	240
Na_2CO_3	335, 515
Na_3PO_4	200, 485

5.3 Morphology evolution

Nucleation and subsequent growth of gibbsite crystals from pure sodium aluminate solutions was found to occur at all driving forces, even at the lowest values. Once nucleation had taken place, crystal growth resulted in a range of shapes and sizes within one experiment. The crystalline material consisted of hexagonal and lozenge-shaped crystals. The presence of prisms and chamfered faces was also observed. In figure 5.1, a SEM image of gibbsite crystals of different morphologies is shown. These crystals were grown simultaneously in the same experiment.

The diversity in morphology is in accordance with our previous studies, in which it was related to growth rate dispersion, defect structure and apparently the presence of impurities. A continuous formation of new nuclei during the growth process, as was revealed in the *in-situ* study of chapter 4, also leads to a variation in crystal size. Furthermore, different induction times for different experiments carried out at the same conditions induces additional differences in crystal growth history. Now the question arises whether the dispersion in morphology is also related to the 'age' of the crystals.

Many individual crystal morphologies were monitored and, despite the fact that the morphologies and sizes of gibbsite crystals were so different within one experiment, a significant general evolution in growth morphology could still be observed. A schematic representation is given in figure 5.2. The morphology evolution was more or less identical for all growth experiments done with caustic concentrations of 100, 200 and 300 g/l Na_2CO_3 and different driving forces. It was found that only the time scale of the occurrence of the different stages of growth was different. For experiments at low driving force the evolution in morphology was slower and the individual crystals remained smaller, as compared to growth experiments at high driving force. At high driving force, much larger

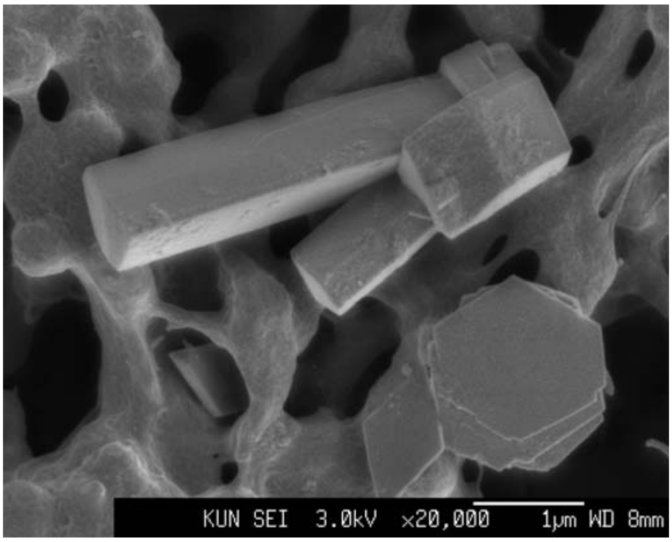

Figure 5.1: SEM image of gibbsite crystals with different morphologies obtained from the same experiment. The crystals are lying on a filtration paper. In this micrograph, a hexagonal and lozenge-shaped plate crystal are shown as well as a block-like crystal and two prismatic crystals.

crystals up to 100 μm were obtained. Here, the solid phase nucleated relatively fast and passed the different stages in the process of crystal growth quickly.

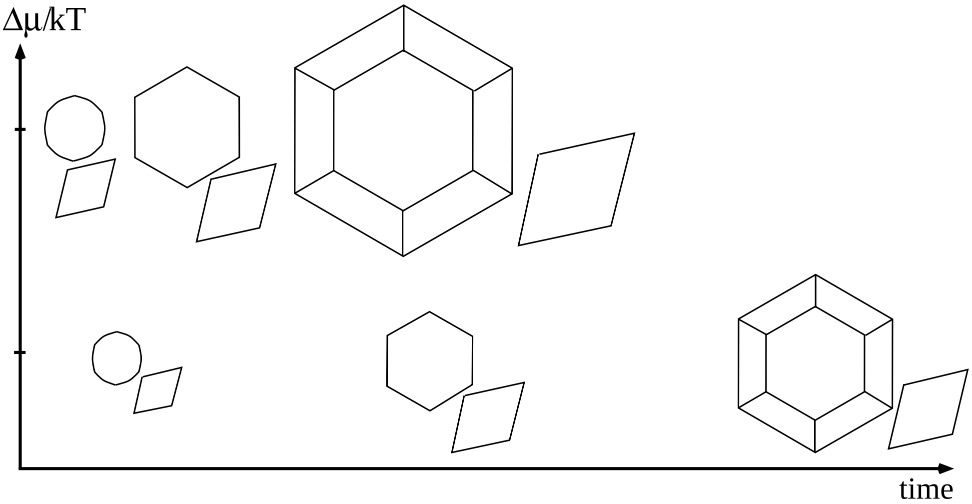

Figure 5.2: The evolution of gibbsite crystals in time. The crystallisation starts with the formation of small rounded hexagons and faceted lozenges. The hexagonal crystals develop to large plates and upon further growth to large prismatic crystals with chamfered faces. At higher driving force, the morphology evolution proceeds faster in time and the crystals develop to a larger size.

At the beginning of the gibbsite crystallisation process tiny, platy crystals were generally found. The size of these crystals was typically a few (2-4) μm in diameter and only 50-100 nm thick. Most of these crystals had a rounded hexagonal morphology, but lozenge shapes as well as faceted hexagons of the same size were also observed. Figure 5.3 shows examples of the different kinds of these tiny crystals. At this stage of the crystal growth process, little or no growth occurred in the <001> direction. The very small crystals were mainly found in the vessels of short growth time (i.e. 6h) and occasionally in vessels of longer growth time (i.e. 24h). It is possible that these latter tiny crystals were formed immediately at the start of the crystallisation process, but that they were unable to grow due to a lack of any defects. It is more likely that they were formed by nucleation at a later stage of the experiment.

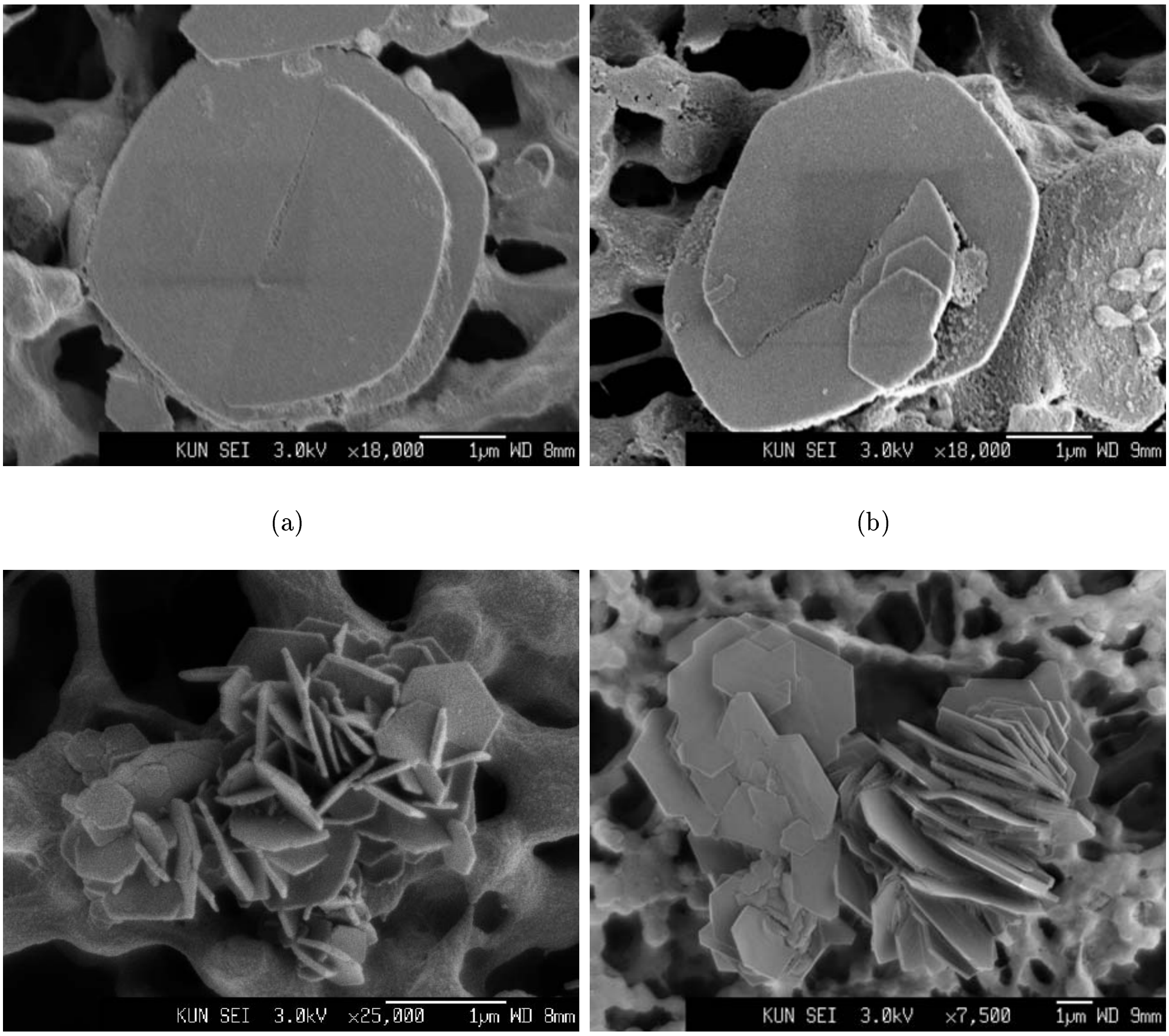

(a) (b)

(c) (d)

Figure 5.3: SEM images of tiny gibbsite crystals formed at an early stage of growth with (a), (b) rounded hexagonal morphology, and (c), (d) with faceted side faces.

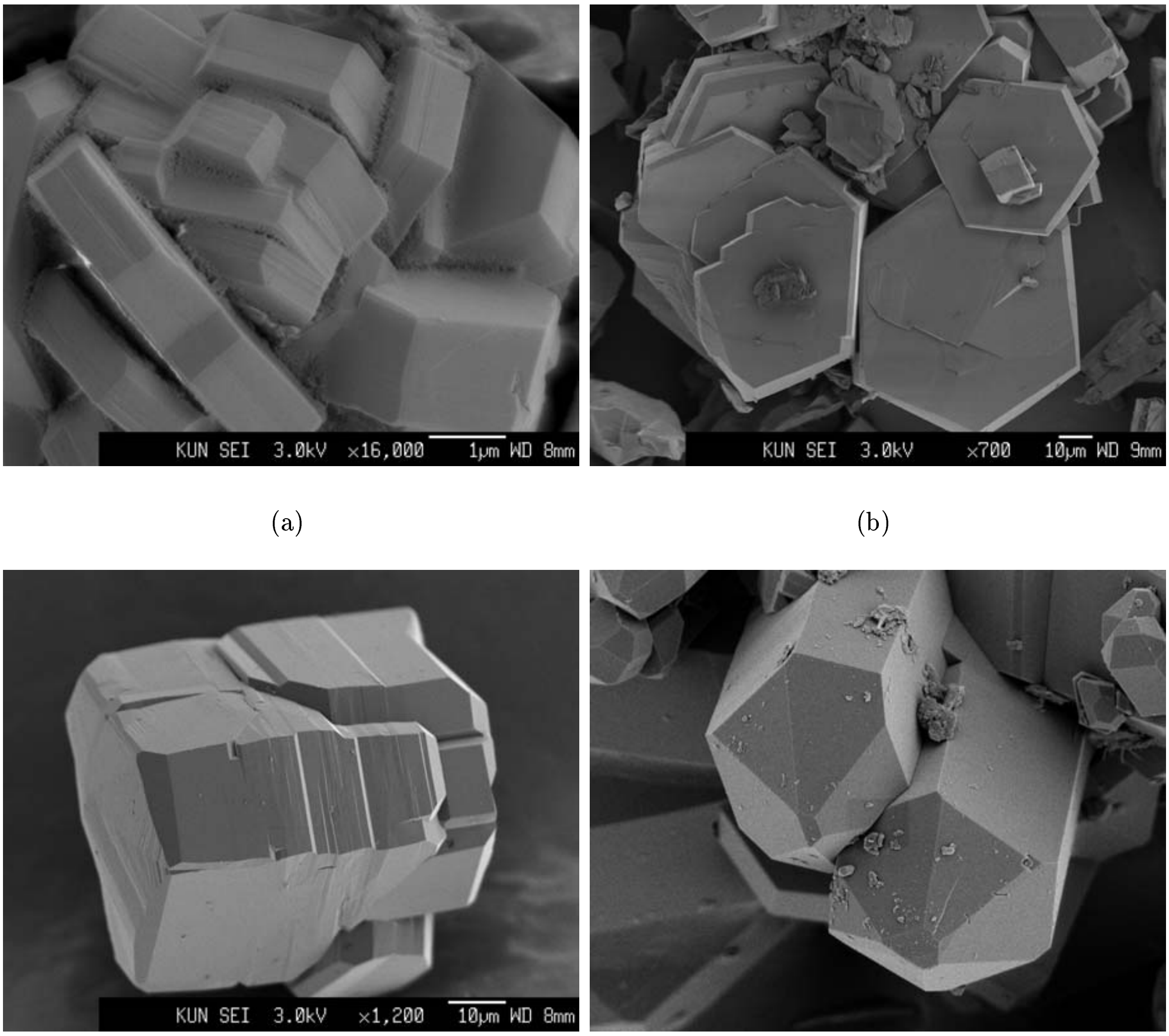

(a) (b)

(c) (d)

Figure 5.4: SEM images of gibbsite crystals upon further growth, with faceted hexagons of (a) a few μm and (b) tens of μm in size, (c) block-shaped crystals, and (d) crystals with large chamfered faces (size of the image is 15 by 12 μm^2).

As crystal growth continued, faceted side faces appeared, which habit changed during growth. At first, the crystals developed to platy lozenges and hexagons, 2-6 μm in diameter and 0.2-1 μm thick. Generally, the hexagonal crystals showed no or only small reentrant corners and no chamfered faces. Upon further growth, the hexagons developed to more block-shaped crystals with typical sizes of 4 by 4 μm^2. An example is shown in figure 5.4a. Further progress of crystal growth resulted in a diversity of crystal morphologies: plate-like, block-like and prismatic crystals were encountered in many different sizes, ranging from 2-25 μm lateral and 4-25 μm in height. Sometimes, crystals of some tens of μm in size were found (figure 5.4c). This change in habit reflects an increase in growth rate along the <001> direction relative to the lateral direction. This can be the result of the decreasing driving force $\frac{\Delta\mu}{kT}$. However, a clear relation between the driving force and the growth rate ratio $\frac{R_{\{001\}}}{R_{lateral}}$ was not found in this study. Moreover, it is known from our previous *in-situ* study that the growth rate ratio $\frac{R_{\{001\}}}{R_{lateral}}$ becomes larger with increasing driving force. Therefore, it is more likely that the enhanced growth along $\boldsymbol{c}$ is the result of the accumulation of defects which generate steps on the basal face. The extent to which this effect changes the habit of the crystals depends on the stage of the crystal growth process. At the end of the crystallisation period, which was about 7 days, crystals of all habits and sizes were observed, suggesting that nucleation and subsequent crystal growth took place continuously during the crystallisation process. In addition, the chamfered faces became well-developed (figure 5.4d).

With polarisation microscopy, it was observed that the hexagons larger than 5 μm were all sixfold twinned in {110}. Most of them were not perfectly twinned, but had very irregular twin boundaries due to stress domains. It was impossible to detect twinning for crystals < 5 μm, even with the use of a Brace-Köhler compensator, because of their limited thickness. Most blocks and prismatic crystals were twinned perpendicular to $\boldsymbol{c}$. The larger blocks (> 10 μm) also showed twinning parallel to $\boldsymbol{c}$, although this was difficult to detect due to light scattering from the striated patterns, in and on the crystals, generated by defects as described in chapter 3.

The morphological evolution suggests the existence of a relation between the morphology of crystals and the 'age', i.e. the crystallisation time of the gibbsite crystals. Upon crystallisation the gibbsite crystals changed from small, rounded hexagonal crystals, to platy and even block-like hexagons with large chamfered faces. It is suggested that, apart from a trivial continued nucleation of new crystals, the influence of the time is at least two-fold. Firstly, the driving force decreases upon growth, which results in a change in relative growth rates of the different crystal faces. This effect clearly caused the appearance of the {101} and {112} chamfered faces at the end of growth. The occurrence of these faces at low driving forces agrees with the equilibrium morphology obtained from the extended connected net analysis described in chapter 6. Secondly, defects are formed and accumulate in the crystals upon further crystallisation and cause dispersion in crystal growth. It is well-known that small crystals, free from defects grow slowly. However, if in a number of crystals dislocations are generated upon collisions or crystals adhere to each other, enhanced growth of certain crystal faces is enabled by a spiral mechanism or contact nucleation. Thirdly, a possible, but less apparent explanation might be the influence of solvent restructuring on the crystal growth process or CO_2 absorption from the ambient. The exact composition of the solution is dependent on its age, which again may affect the relative growth rates of the different crystal faces.

5.4 Morphological aspects

5.4.1 Morphodrome

The morphodrome, illustrating the range of gibbsite morphologies obtained at various crystallisation conditions after 24h growth time, is shown in figure 5.5. It must be noted that only a mean morphological appearance of the crystals is presented.

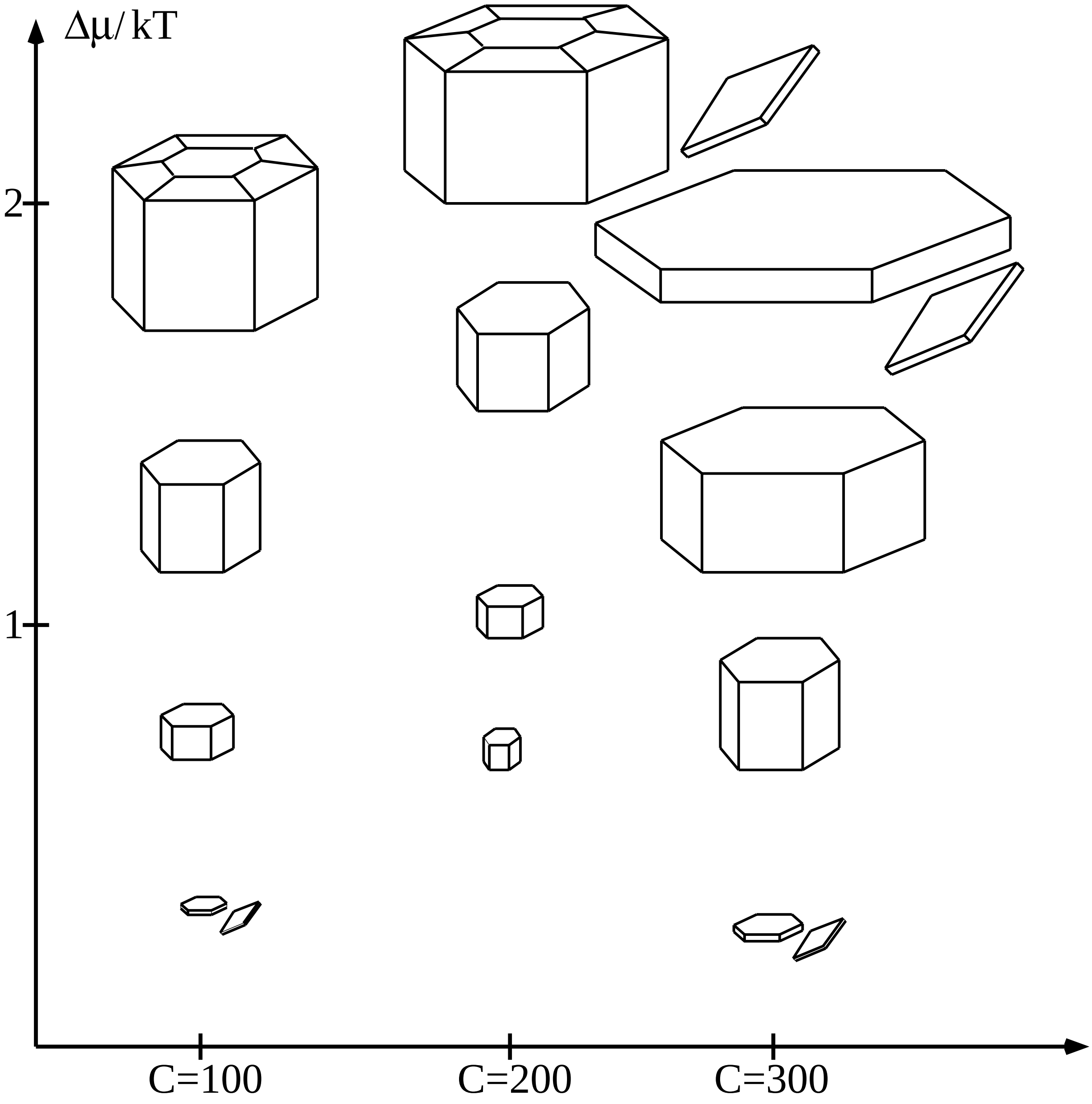

Figure 5.5: Morphodrome, which illustrates the average morphologies of gibbsite crystals grown at various conditions.

Despite the dispersion effects, the morphodrome shows that increasing $\frac{\Delta\mu}{kT}$ as well as the caustic concentration (C) results in faster growth. Furthermore, a larger C gives more platy crystals, i.e. the average growth rate ratio of the {001} top and side faces decreases. The influence of the experimental growth conditions, i.e. caustic concentration and gibbsite concentration, on the crystal shape can, thus, not be characterised by only the driving force parameter.

5.4.2 Lozenge-shaped crystals

It can not be excluded that the platy lozenges encountered in nearly all experiments are composed of another aluminium oxide hydroxide mineral, like the $Al(OH)_3$ polymorphs bayerite and nordstrandite, or AlO(OH) minerals boehmite and diaspore. For bayerite and nordstrandite no morphological data were found, except for one picture in reference [19]. The angle between the side faces of these nordstrandite crystals is measured to be 66° ± 1. The mineral boehmite forms plate-like structures with $\{010\}$ top face and $\{101\}$ and $\{001\}$ side faces [20]. The angle between the $\{101\}$ side faces are 75.6 and 104.4°, corresponding to the angles of the side faces shown in references [20, 21]. The angles between the side faces of the lozenges obtained in our experiments are, however, 60 and 120°, which corresponds to the gibbsite structure rather than boehmite. The appearance of the AlO(OH) mineral diaspore was also not possible, since the angle between its side faces are 65.8 and 114.2°. Laser Raman spectroscopy also proved that the thicker plate-like lozenges are the gibbsite polymorph. The *ultra thin* lozenges were too thin for characterisation with Raman. However, the geometrical similarities between the habits of the thicker and ultra thin lozenges suggests that the latter ones are gibbsite too.

5.4.3 Single and twinned crystals

Figure 5.6 presents a typical group of crystals which was observed at the beginning of crystal growth experiments at high driving force. In this figure, two types of morphology are shown: platy, single crystalline lozenges with $\{001\}$ basal and $\{110\}$ side faces and hexagons sixfold twinned in $\{110\}$ with $\{001\}$ basal and $\{100\}$ side faces. Normally, the hexagonal crystals are much larger than the lozenge-shaped crystals. The relatively larger growth rate of the $\{100\}$ faces of the hexagons together with enhanced growth at the twin plane reentrant corners normally leads to crystals up to hundred μm as described in chapter 2. Probably, these small hexagonal crystals were nucleated just before removal of the crystalline material from the solution.

On the basis of the similarities in the atomic structure of the different prismatic faces $\{110\}$ and $\{100\}$, similar growth rates would be expected at the same driving force. In that case, single crystalline hexagons would be formed and no lozenges. As will be shown in section 5.5, the presence of inorganic impurities does not account for the lozenge-shaped morphology. A detailed connected net analysis (chapter 6) shows that the lozenge-shaped morphology is the result of a difference in edge energy of the $\{100\}$ and $\{110\}$ faces. Since the edge energy of $\{100\}$ is lower, the $\{100\}$ faces are the fast growing faces relative to the $\{110\}$ faces. If the difference in growth rate between the $\{100\}$ and $\{110\}$ faces is large enough, the sixfold twinned hexagons develop into star-like crystals bounded by $\{110\}$ faces, as schematically shown in figure 5.7. In this study, several of such stars were observed, which are presented in figure 5.6. In most cases, however, the enhanced growth of the $\{110\}$ faces as a result of step nucleation at the twin-plane reentrant corners was sufficient to cope with the fast $\{100\}$ growth and normal, sixfold twinned hexagons are formed.

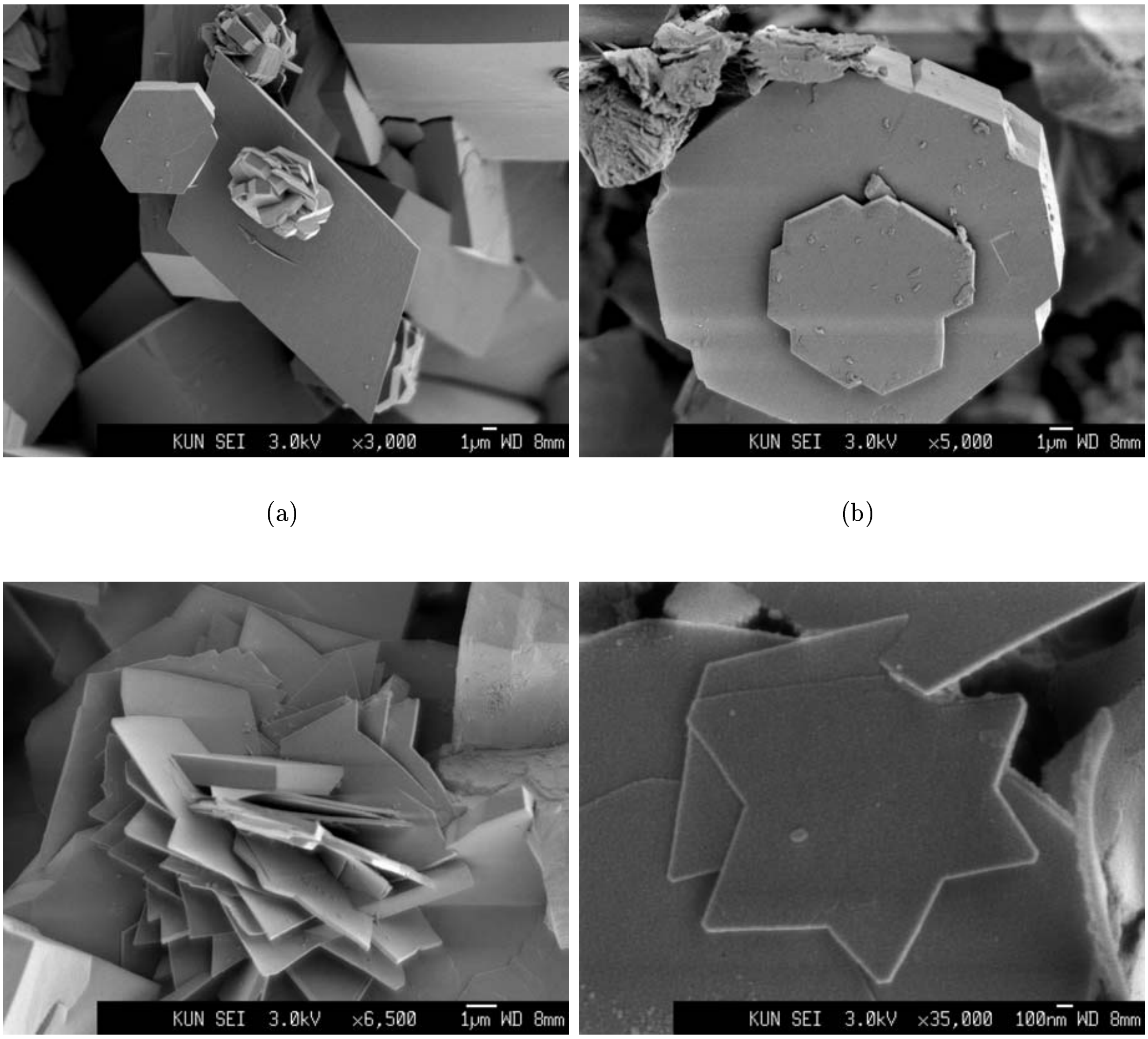

(a) (b)

(c) (d)

Figure 5.6: SEM images of gibbsite crystals formed at high driving forces. (a) Large lozenge-shaped and small hexagonal gibbsite crystals, (b) hexagonal sixfold twinned crystals with large reentrant corners, (c) and (d) star-like gibbsite crystals bounded by {110}, formed by the outgrowth of the {100} faces of the sixfold twinned hexagons.

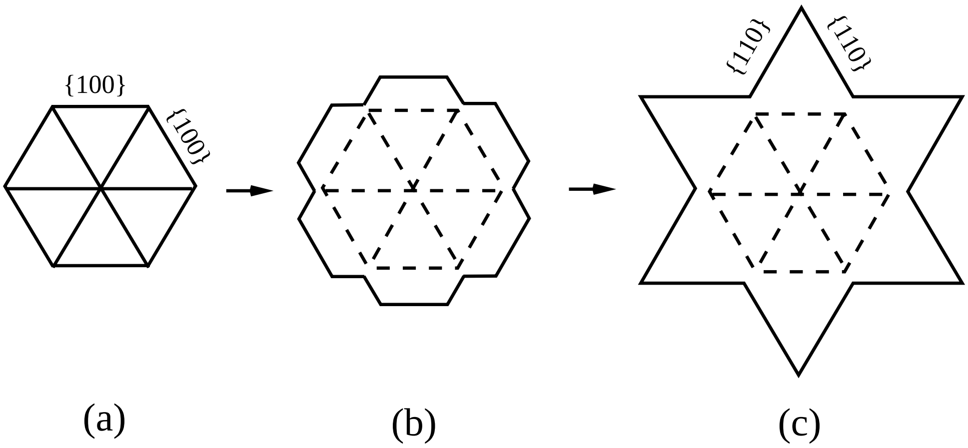

Figure 5.7: Schematic presentation of platelet shaped gibbsite crystals sixfold twinned in {110}. (a) $R_{\{100\}} \leq \frac{\sqrt{3}}{2} R_{\{110\},reentrant\ corner}$ gives hexagonal plates. (b) If $R_{\{100\}} > \frac{\sqrt{3}}{2} R_{\{110\},reentrant\ corner}$, star-like morphologies develop (c).

Figure 5.8 shows a partly dissolved hexagonal sixfold twinned crystal as imaged with *in-situ* optical microscopy. Dissolution was performed by increasing the temperature of the growth cell. It can be seen that dissolution started along the twin boundaries, leading to segmentation of the crystal. This indicates that the twin boundaries possess a lot of stress, which locally enhances dissolution.

Figure 5.8: Dissolution of a sixfold twinned hexagon along its twin boundaries. The size of the image is 200 μm.

5.4.4 Chamfered faces

The platy morphologies found at the beginning of crystallisation changed to block-like morphologies with large chamfered faces at the end of the process. Some characteristics were observed in the development of these faces. Lozenge-shaped crystals often had two $\{101\}$ chamfered faces, situated at the bottom and top of the crystal, which are opposite to each other in case of untwinned crystals (figure 5.9a and b). If the crystal is mirror twinned perpendicular to $\boldsymbol{c}$, then the two $\{101\}$ faces are at the same side of the crystal (figure 5.9c and d). The asymmetry in appearance of the chamfered faces in case of single crystals reflects the twofold axis along [010] in the point group 2/m of gibbsite.

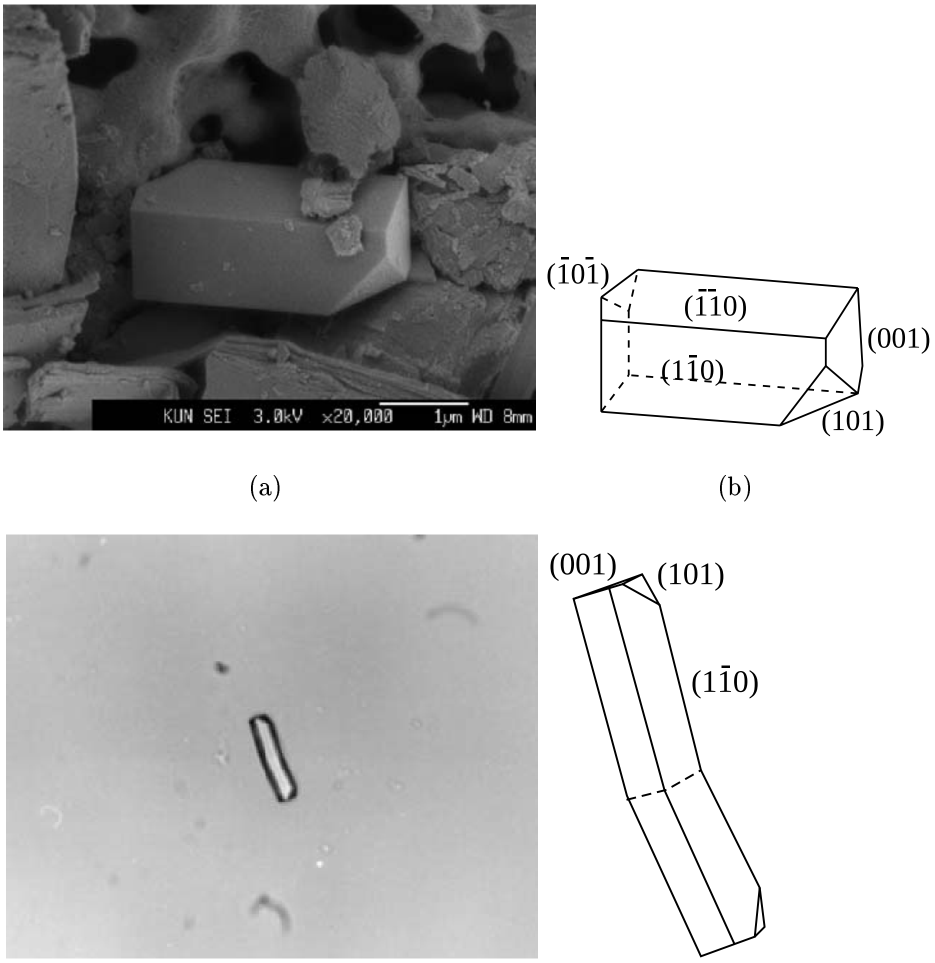

(a) (b)

(c) (d)

Figure 5.9: Development of chamfered faces on lozenge-shaped prisms. (a,b) Single crystal with two opposite $\{101\}$ faces; (b,c) Twinned crystal with the two $\{101\}$ faces at the same side of the crystal. The twin is identified as a mirror twin on $\{001\}$, since the two components are mirror symmetric with respect to the common $\{001\}$ twin boundary, indicated by the dashed line. The width of image (c) is 200 μm.

Hexagonal and prismatic gibbsite crystals often show chamfered faces {101} of different sizes. The symmetry imposed occurrence of the chamfered {101} faces at opposite sides as observed for the lozenges was not found for the hexagons. This is another indication that virtually all hexagons are twinned.

5.4.5 Somatoids

In some experiments, somatoids were found. These deposits were very rough and consisted of cone-shaped particles of a few microns in size. They were mainly observed at high driving forces. Figure 5.10a shows an example of these somatoids. It seems that these particles are often built up of smaller somatoids. Cone-shaped particles were previously observed on the chamfered faces with electron microscopy (chapter 3). Cornell et al. [22] also found the rapid development of numerous small outgrowths on the chamfered faces. These particles coalesced and formed a new layer [22]. In this study, the outgrowth of cone-shaped particles on crystal faces was also observed. However, this occurred on the basal faces of the gibbsite crystals instead of the chamfered faces. In figure 5.10, it is shown that cone-shaped particles formed at the basal faces coalesce to a layer on which some new cone-shaped particles are formed again.

It is possible that these particles are the $Al(OH)_3$ polymorph bayerite. It was suggested by Addai-Mensah [23] that in the crystallisation of $Al(OH)_3$, first an amorphous bayerite layer is formed which is transformed to gibbsite. This would indicate that bayerite is the metastable polymorph of $Al(OH)_3$. High driving forces may well effect the formation of this type of polymorph. Unfortunately, the cone-shaped particles were too small to be recognised with optical microscopy and, therefore, it was not possible to identify them with Raman spectroscopy.

5.4.6 Agglomeration

Gibbsite particles also increase their initial size by agglomeration, which occurs simultaneously with growth. Individual particles form clusters by a process that is not fully understood. It is supposed that agglomeration is favourable if the supersaturation is high [14]. Some authors speculate that in that case $Al(OH)_3$ will not crystallise well on the seed, leading to disordered deposits. This unordered material will lead to randomly oriented crystallites upon further crystallisation. If the crystallisation rate is low, the deposit is better ordered and perfectly formed crystals will appear. Others speculate that agglomeration consists of two steps [24, 25]. Gibbsite particles first stick together, which is followed by growth of gibbsite that 'cements' the loosely formed agglomerates to firm particles.

In this study, it is observed that agglomeration of gibbsite occurs in several ways. The gibbsite particles agglomerated randomly, but also ordered, i.e. face to face or edge to edge. In case of face to face agglomeration, the top basal faces are stuck together and in edge to edge the side faces are stuck together. Figure 5.11 shows some examples. The occurrence of the different kinds of agglomeration may depend on the zeta potential of the individual faces of the crystals, as suggested by Wierenga et al. [26]. Although the

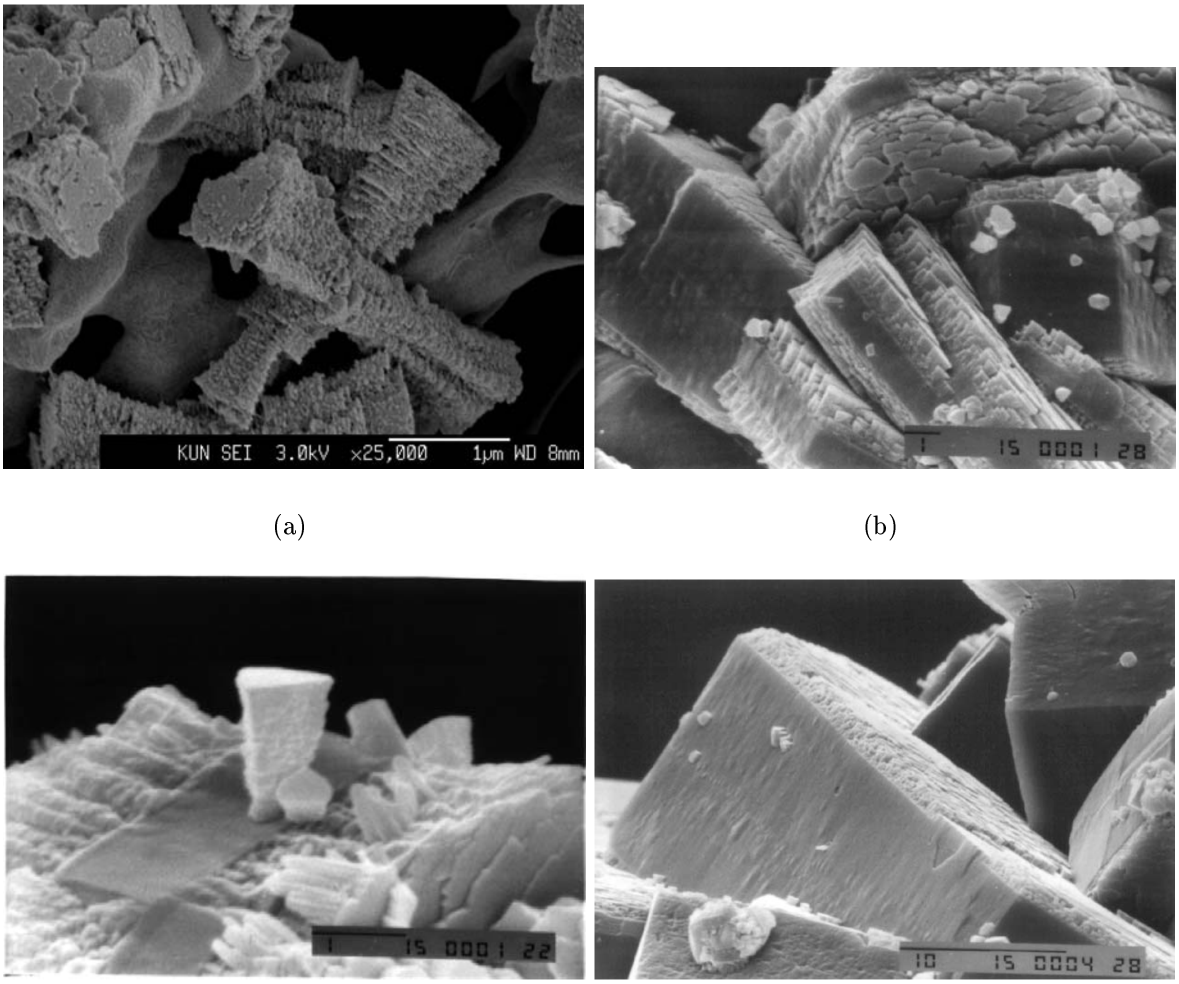

(a) (b)

(c) (d)

Figure 5.10: (a) Somatoids of cone-shaped habit. (b), (c) The appearance of somatoids on the basal face of gibbsite crystals, which coalesce and form a new layer (d). The scale bars in (b), (c) and (d) are 1, 1 and 10 μm, respectively.

strength of the ionic solutions varied as a result of a difference in caustic concentrations, the zeta potential of the faces was such that edge to edge agglomeration was favourable.

The amount and kind of agglomeration varied for different experiments. In the same experiments, edge to edge, face to face as well as random agglomeration were found. Furthermore, the individual crystals of one agglomerate were of similar size, but also agglomerates composed of crystals of random size were encountered. In general, agglomeration increased for higher driving forces, probably since more material is available. The inorganic impurities added to the system did not have an influence on the amount of agglomeration (see section 5.5).

A special kind of agglomeration positioned on the basal face of a large hexagon is shown in figure 5.11d. This kind of agglomeration, which is called 'spiral agglomeration',

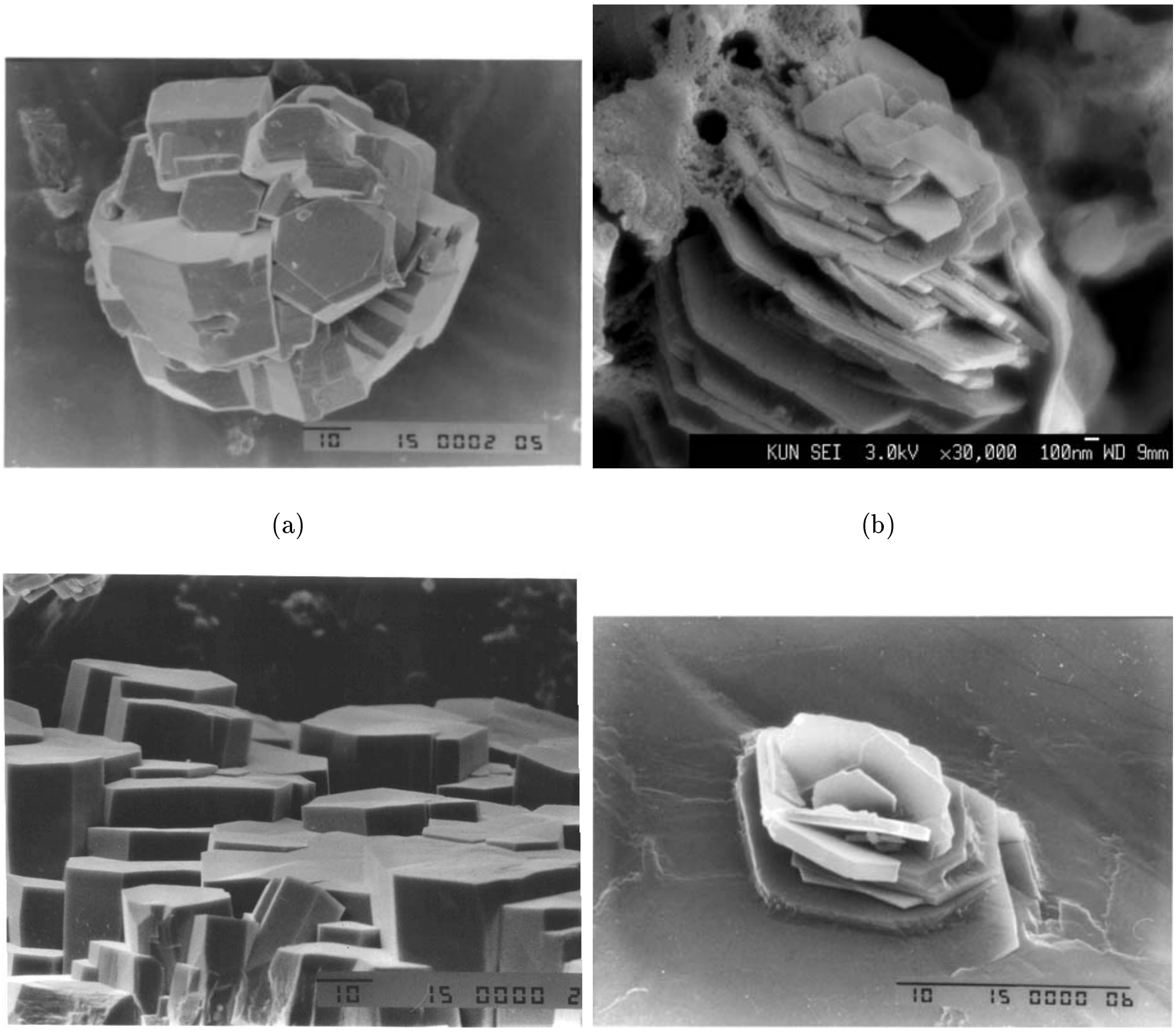

(a) (b)

(c) (d)

Figure 5.11: SEM images of several kinds of agglomeration, (a) random (scale bar is 10 μm), (b) face to face, (c) edge to edge (scale bar is 10 μm), and (d) spiral agglomeration (scale bar is 10 μm).

is mostly composed of thin platelets and rather resembles a kind of spherulitic growth, probably nucleated on a defect.

Besides growth as a result of the agglomeration process itself, agglomeration also induced enhanced growth by contact nucleation at the intersection lines of the individual crystals of the agglomerate. This was already shown in our previous surface topographic study of gibbsite (chapter 3).

5.5 Impurities

5.5.1 Inorganic cations and anions

The crystalline material obtained in the presence of *positively* charged impurities was similar to the crystals obtained from pure sodium aluminate solutions. The morphology, the growth rates of the faces and the aspect ratio of the crystals, thus, did not significantly vary with the addition of these impurities to the solution. Hexagonal plates and blocks were common, up to 100 μm in size. The crystals were often faceted with mostly chamfered faces, but sometimes unfaceted crystals were also obtained. They were all sixfold twinned, with many stress domains. The surface structure was irregular and similar to that described in chapter 3 for large gibbsite crystals. Macro steps, growth hillocks and planar faults were observed on the $\{001\}$ basal faces, while a striated structure was found on the prismatic faces. Observations of Brown [12], suggested that copper ions adsorb on the $\{001\}$ surface and generate secondary nuclei on the prismatic faces of the gibbsite crystals. This is in contrast to our observations. Crystals grown from sodium aluminate solutions with added copper impurity were in all experiments of similar size as crystals grown from pure solutions and showed the same surface structures as described above. The enhanced agglomeration effect upon copper addition as reported by Brown was also not observed. None of the positive impurities added was found to affect agglomeration in our experiments. Although there was no change in habit of the gibbsite crystals, samples grown from Fe^{3+} and Cu^{2+} polluted solutions were coloured, pink and blue respectively. Application of the ICP technique confirmed the presence of these metals in the samples at concentration levels of 17.000 and 7000 ppm, respectively. However, the samples were not coloured homogeneously and EDS showed that these metals were present in phases separate from gibbsite and with a different morphology. In pure gibbsite no other compounds then aluminium and oxygen were found above the EDS detection limit of 1%.

In the presence of *negatively* charged impurities, again the crystals obtained were not significantly different from the crystals grown from pure solutions. Only the crystals grown from sodium aluminate solutions with sulfate ions showed a slight modification in their habit. These crystals had slightly rounded side faces.

Although poisoning of crystal surfaces by impurities would explain the formation of prismatic crystals by blocking of lateral growth (chapter 2), there is no indication from this study that inorganic impurities in trace amounts have an inhibiting (or promoting) effect on gibbsite crystallisation. Even the effect on agglomeration due to surface roughening, as described in the literature [12], was not observed.

Although, inorganic impurities apparently do not play a role in inhibiting the growth of gibbsite, organic impurities can still be important as suggested in the literature.

5.5.2 Alkali ions

Whereas gibbsite grown from sodium aluminate solutions resulted in plates and blocks, prismatic crystals were obtained from potassium aluminate solutions under similar conditions.

This indicates a dramatic change in the relative growth rate of the basal and side faces. Hexagonal prisms were also formed from cesium aluminate solutions. These morphologies correspond with those described by Wefers et al. [15] and Lee et al. [16]. Most of the prisms were twinned perpendicular to $\boldsymbol{c}$, with the $\{001\}$ face as the mirror and composition plane. Some of these crystals showed twofold twinning or threefold twinning perpendicular to $\boldsymbol{c}$. Prisms viewed along the c-axis showed occasionally one twin boundary parallel to $\boldsymbol{c}$. The sixfold twinning as observed for the hexagonal plates grown from sodium aluminate solutions was also found for some of the hexagonal prisms. These results indicate that the alkali ions of the alkali hydroxide solution have a major influence on the morphology of gibbsite, but less on its twinning behaviour. The underlying mechanism of the morphology change is not understood.

5.6 Conclusions

Gibbsite crystallisation is notorious for its large dispersion in defect structure, morphology and size. To investigate the influence of external conditions on these properties, gibbsite crystals were grown under a wide range of conditions and inorganic impurity additions.

From this study, the following conclusions can be drawn:

(1) During growth the gibbsite morphology evolves: Crystallisation starts with the formation of thin, rounded hexagons and faceted lozenges. Upon further growth, these crystals develop into faceted plates and blocks with well-formed basal, prismatic and chamfered faces.

(2) There is a weak dependence of morphology on growth conditions. Changing the external conditions, i.e. increasing driving force and/or caustic concentrations, leads to a faster development of the morphology evolution. Larger crystals are obtained at higher driving forces and higher caustic concentrations.

(3) The influence of small amounts of inorganic impurities on gibbsite growth properties is negligible: Similar growth morphologies and surface structures are obtained for gibbsite grown from pure and impure sodium aluminate solutions.

(4) Changing the alkali ions in the caustic solution (K^+, Cs^+ instead of Na^+) largely effects the crystal morphology: Prismatic crystals instead of mainly platelets and blocks grow from potassium and cesium hydroxide solutions.

In conclusion, the spread in growth morphology of gibbsite crystals is to a considerable extent an intrinsic property, rather than being introduced by external conditions, such as driving force, caustic concentration and impurities. These intrinsic properties are, for instance, twinning at the nucleation stage, accumulation of defects during further growth, continuous formation of nuclei during growth and restructuring of the solution. This also explains the dispersion in growth rate of the crystals. However, many aspects of gibbsite crystal growth are still shrouded in mystery and need clarification in the future.

References

[1] T.G. Pearson, The chemical background of the aluminium industry (Royal Institute of Chemistry, London, Monograph no. 3, 1955).

[2] G. Lever, Light Metals (1978) p. 71.

[3] J.D. Guthrie, P.J. The and W.D. Imbrogno, Light Metals (1984) p. 127.

[4] P.J. The, Light Metals (1980) p. 119.

[5] A. Alamdari, J.A. Raper and M.S. Wainwright, Light Metals (1993) p. 143.

[6] P.G. Smith, H.R. Watling and P. Crew, Colloids and Surf. A 111 (1996) p. 119.

[7] M. Lee, F. Lincoln, G. Parkinson and P. Smith, Proc. of the Fourth International Alumina Quality Workshop (1996).

[8] D.S. Rossiter, D. Ilievski, P.G. Smith and G.M. Parkinson, ICemE 74 (1996) p. 828.

[9] H.R. Watling, R. Townsend and J.S.C. Loh, IChemE (1999).

[10] A. Owen, H.R. Watling, W. van Bronswijk and Z.-S. Yu, ICemE (1999).

[11] I. Seyssiecq, S. Veesler, G. Pèpe and R. Boistelle, J. Cryst. Growth 196 (1999) p. 174.

[12] N. Brown, J. Cryst. Growth 87 (1988) p. 281.

[13] N. Brown, J. Cryst. Growth 92 (1988) p. 26.

[14] S. Veesler, S. Roure and R. Boistelle, J. Cryst. Growth 135 (1994) p. 505.

[15] K. Wefers and C. Misra, Oxides and Hydroxides of Aluminium, Technical Report Technical Paper no. 19, revised Alcoa Research Laboratories, Pittsburgh, Pennsylvania (1987).

[16] M.-Y. Lee, A.L. Rohl, J.D. Gale, G.M. Parkinson and F.L. Lincoln, IChemE 74 (1996) p. 739.

[17] B.N. McCoy and J.L. Dewey, Light Metals (1982) p. 173.

[18] C. Misra, Chemistry and Industry 19 (1970) p. 619.

[19] D.J. Shaw, editor, Colloid and surface chemistry (Butterworth-Heinemann, 1991) 4th edition.

[20] W.-J. Li, E.-W. Shi, W.-Z. Zhong and Z.-W. Yin, J. Cryst. Growth 203 (1999) p. 186.

[21] K. Wefers and G.M. Bell, Oxides and Hydroxides of Aluminium, Technical Report Technical Paper no. 19 Alcoa Research Laboratories, Pittsburgh, Pennsylvania (1972).

[22] R.M. Cornell, C.F. Vernon and D.S. Pannett, Proc. of the Fourth International Alumina Quality Workshop (1996) p. 97.

[23] J. Addai-Mensah, Min. Eng. 10 (1997) p. 81.

[24] I. Seyssiecq, S. Veesler, R. Boistelle and J.M. Lamérant, Chem. Eng. Sci. 53 (1998) p. 2177.

[25] I. Seyssiecq, D. Mangin, J.P. Klein, S. Veesler and R. Boistelle, IChemE (1999).

[26] A. M. Wierenga, T.A.J. Lenstra and A.P. Philipse, Colloids and Surfaces 134 (1998) p. 359.

Chapter 6

Morphology prediction of gibbsite crystals

– An explanation for the lozenge-shaped growth morphology –

C. Sweegers, S.X.M. Boerrigter, R.F.P. Grimbergen, H. Meekes,
S. Fleming, I.D.K. Hiralal and A. Rijkeboer [1]

Abstract

The morphology of gibbsite, γ-Al(OH)$_3$, crystals is predicted on the basis of a complete connected net analysis. It turns out that the morphology can not be explained on the basis of the attachment energy. Instead, it is shown by a Monte Carlo algorithm based on a 2D nucleation model, that the edge (free) energy of the F-faces is the relevant parameter that describes the growth morphology. The algorithm reveals that the morphological importance of the faces follows the sequence: $\{112\}$, $\{11\bar{2}\} \approx \{101\}$, $\{10\bar{1}\} < \{200\} < \{110\} \ll \{002\}$. At zero driving force, gibbsite has a hexagonal morphology with $\{002\}$ basal, $\{200\}$ and $\{110\}$ side and $\{101\}$, $\{10\bar{1}\}$, $\{112\}$ and $\{11\bar{2}\}$ chamfered faces. At higher driving forces, the chamfered faces will disappear first, followed by the $\{200\}$ faces. This corresponds well to our experimental results and is explained in terms of the bonding topology at the surface. The energy for making a 2D nucleus on the prismatic faces is lower for the $\{200\}$ faces compared to the $\{110\}$ faces. This indicates that a lozenge shape, bounded by $\{002\}$ and $\{110\}$ faces, is the basic morphology of gibbsite crystals, in accordance with experimental observations.

---

[1] The work in this chapter has been submitted to *J. Cryst. Growth.*

6.1 Introduction

Gibbsite, γ-Al(OH)$_3$, is commercially important as an intermediate in the production of aluminium metal. In the Bayer process, this compound is formed through crystallisation from hot supersaturated sodium aluminate solutions [1]. As demonstrated in previous chapters, the morphology of gibbsite crystals is an important parameter to understand the crystallisation process.

In chapter 2, the large variety of shapes and sizes in which gibbsite crystals occur when grown from sodium aluminate solutions was described. Amongst these varied forms, hexagonal crystals were often observed. The prismatic faces of the hexagons are usually indexed as $\{110\}$ and $\{100\}$. These crystals, however, were found to be sixfold twinned with the prismatic faces consisting entirely of $\{200\}$ faces. The twinning is very understandable regarding the pseudohexagonal structure of gibbsite. In contrast, single crystals of gibbsite possessed a lozenge-shaped morphology, only consisting of $\{110\}$ side faces, despite the pseudohexagonal symmetry. The $\{200\}$ faces were occasionally observed, resulting in truncated lozenges. Figure 6.1 shows the lozenge-shaped crystal habit of gibbsite, indicating all possible faces. Monitoring many lozenges revealed that the morphological importance of the faces follows the sequence: $\mathrm{MI}_{\{002\}} \gg \mathrm{MI}_{\{110\}} > \mathrm{MI}_{\{200\}} > \mathrm{MI}_{\{101\},\{10\bar{1}\}} \approx \mathrm{MI}_{\{112\},\{11\bar{2}\}}$. The lozenges bounded by $\{110\}$ faces grew laterally much slower than the twinned hexagons bounded by $\{200\}$ faces. The growth mechanisms resulting in the various morphologies have been treated in chapter 2, 4 and 5. The main result is that all faces grow by a 2D nucleation mechanism or a 2D contact nucleation mechanism. In addition, sometimes spiral growth is observed on the $\{002\}$ faces.

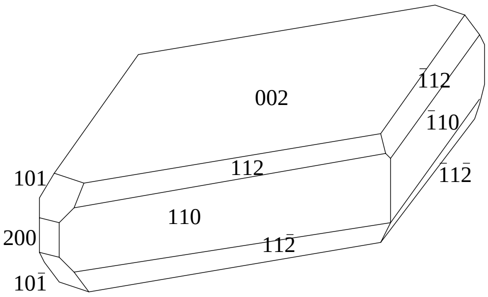

Figure 6.1: The basic lozenge-shaped morphology of gibbsite single crystals, showing all faces that can appear in experiments. The $\{002\}$ and $\{110\}$ faces are always present.

The theoretical morphology of gibbsite crystals has already been studied by other authors. The morphology was predicted by Boistelle, as mentioned in reference [2], according to the periodic bond chain theory. This resulted in a hexagonal habit parallel to $\{002\}$ with $\{200\}$, $\{110\}$ and $\{010\}$ prismatic faces and small $\{101\}$, $\{10\bar{1}\}$, $\{112\}$, $\{11\bar{2}\}$ and $\{011\}$ chamfered faces. Lee et al. [3] calculated the equilibrium and growth morphology of gibbsite based on the surface energy and the attachment energy, respectively, of the various crystal faces using the computer code MARVIN [4]. The calculations use a potential model including covalent type force field contributions as well as long range interactions which cover the ionic character of the gibbsite structure. The effect of surface relaxation was included to predict the gibbsite crystal morphology. Both the equilibrium and growth morphology possessed a hexagonal habit with the {002} faces being the most dominant. The equilibrium morphology was further bounded by the {101}, $\{10\bar{1}\}$, {112} and $\{11\bar{2}\}$ faces, whereas the growth morphology was bounded by the {101}, $\{10\bar{1}\}$ and prismatic {110} faces. The {002} face of the growth morphology was elongated along the [010] direction. Fleming et al. [5] developed these computer modelling techniques further. The predicted equilibrium morphology was similar to the one described by Lee et al. [3] with, in addition, small prismatic {200} and {110} faces. The growth morphology elongated along $\boldsymbol{b}$ was bounded by the {112}, $\{11\bar{2}\}$, {101} and $\{10\bar{1}\}$ faces. The authors suggested that the equilibrium morphology predicted was in reasonable accordance with the experiments, which yielded hexagonal plate-like crystals. However, the calculated morphological importance (MI) of the chamfered {101}, $\{10\bar{1}\}$, {112} and $\{11\bar{2}\}$ faces were much higher than in their experiments [5].

In this chapter, the growth morphology of gibbsite is calculated according to an improved connected net analysis. After a short introduction, a concise summary of the results is presented in section 6.3. This section also describes the definition of the growth units in the covalent gibbsite structure as well as the interaction energies between them calculated with the computer code GULP. Using the attachment energies, a growth morphology was obtained, resembling the one described previously by Lee et al. [3]. Furthermore, Monte Carlo simulations of 2D nucleation were used to simulate gibbsite crystal growth taking the actual bond structure of the various faces explicitly into account. The results are in very good agreement with the experimental morphology, suggesting that the MI of F-faces is not well described by their attachment energies, but rather by the energies involved in creating 2D nuclei on the surface. This will be explained in section 6.5 on the basis of a detailed topological net analysis, leading to the basic lozenge-shaped morphology. Finally, a discussion of the results is given.

6.2 Morphology prediction

6.2.1 Hartman-Perdok theory

Hartman and Perdok (HP) developed a theory that relates the crystal morphology to its internal crystal structure on the basis of the bond energies between the growth units [6–8]. In their approach, the structure of a crystal consists of uninterrupted chains of strong bonds (called Periodic Bond Chains, PBCs) formed between growth units, which can be atoms, molecules or ions. The periodicity of these chains run along specific crystallographic directions. Hartman and Perdok showed that, in general, crystals are bounded by facets that are parallel to at least two intersecting PBCs. These faces are called flat faces (F-faces) and usually dominate the morphology of crystals. This follows from the fact that these faces $\{hkl\}$ have the largest slice energy E_{hkl}^{slice}, i.e. the sum of the energy within a slice of thickness d_{hkl}, and thus the smallest attachment energy, E_{hkl}^{att}, since:

$$E_{hkl}^{cryst} = E_{hkl}^{att} + E_{hkl}^{slice}, \tag{6.1}$$

where E_{hkl}^{cryst} is the crystallisation energy. Faces with a small attachment energy usually grow relatively slowly. The small growth rate of F-faces implies that they will be the most prominent faces on a growing crystal and, therefore, have a high MI.

Conversely, the Hartman-Perdok theory can be used to calculate or even predict the morphology. Combinations of non-parallel intersecting PBCs generate connected nets. From these, a morphology can be constructed using the attachment energies. The relative growth rate R_{hkl} of F-faces is frequently considered to be directly proportional to E_{hkl}^{att}:

$$R_{hkl} = CE_{hkl}^{att}, \tag{6.2}$$

where C is a constant. However, the growth rate of a face depends on the actual growth mechanism of that face. In addition, supersaturation, temperature and solid-fluid interaction are known to influence the growth mechanism. They are rarely accounted for in automated morphology prediction methods to date.

A refinement of the HP theory relates the morphological importance of a face (hkl) to its roughening temperature, which defines the transition from a smooth to a rough interface. This order-disorder phase transition is characterised by a critical Ising temperature θ_{hkl}^{R}, which can even be used directly as a measure for the relative MI [9]. The Ising temperature can be determined from the connected nets of a face and their bond energies.

6.2.2 Connected net analysis

In order to predict the morphology from a crystal structure, the growth units have to be defined along with all the interaction energies between them in the crystal structure. This results in a set of growth units and bonds, which is called the crystal graph. From this crystal graph, it is possible to determine the PBCs and connected nets for all orientations (hkl) with thickness d_{hkl} using the computer program FACELIFT [10]. Equivalent connected nets are separated by the interplanar distance d_{hkl}, corrected for the BFDH selection rules of the space group. After construction of the connected nets, the relative MI of the resulting F-faces has to be determined. This can be done using the assumption that the growth rate is proportional to the attachment energy or, alternatively, inversely proportional to the Ising temperature.

Often, more than one connected net is found for an orientation (hkl). The problem is to determine which connected nets are relevant for the growth of that crystal face $\{hkl\}$. In the case that one connected net has the lowest E_{hkl}^{att}, the facet is expected to be determined by that connected net. The combination of symmetry related connected nets, which separately have a finite Ising transition temperature and possibly a small attachment energy, may result in an overall zero edge energy for that crystal face [11–13]. This results in a roughening temperature of zero Kelvin and, consequently, these faces grow rough. This phenomenon is called symmetry roughening. These faces do not appear in the growth morphology, since they grow much faster than the attachment energy predicts. Moreover, pairs of connected nets that are not strictly symmetry related, and even a single connected net with specific bonding topology, can also cause a relatively small edge energy for the corresponding face [14,15]. This results in a relatively low roughening temperature or low threshold for kinetic roughening and a lower MI of that particular face. All these effects result in a growth rate, R_{hkl}, that is no longer proportional to the attachment energy, E^{att}_{hkl}. Therefore, the actual edge (free) energies together with the relevant growth mechanism offer the best indication for the actual growth rate of a crystal face.

6.3 Connected net analysis of gibbsite

6.3.1 Structure of gibbsite

Gibbsite, γ-Al(OH)$_3$, has a monoclinic space group, $P2_1/n$, with cell parameters $a = 8.684$ Å, $b = 5.078$ Å, $c = 9.736$ Å and $\beta = 94.54°$. The asymmetric unit contains two Al(OH)$_3$ molecules resulting in a total of 8 molecules per unit cell [16]. The BFDH selection rules for the space group $P2_1/n$ are $\{h0l\}$: $h+l = 2n$ and $\{0k0\}$: $k = 2n$. Note that in this chapter Miller indices corrected according to the selection rules of the spacegroup are used. The structure of γ-Al(OH)$_3$ is pseudohexagonal, with the c-axis as the pseudohexagonal axis and consists of double layers (AB) of close packed OH groups with Al atoms occupying two third of the octahedral interstices within the layers [17]. The AB layers are stacked according to the sequence ...-AB-BA-AB-BA-... . Figure 6.2 shows the atomic arrangement of the hydroxide groups and aluminium atoms in the crystal structure.

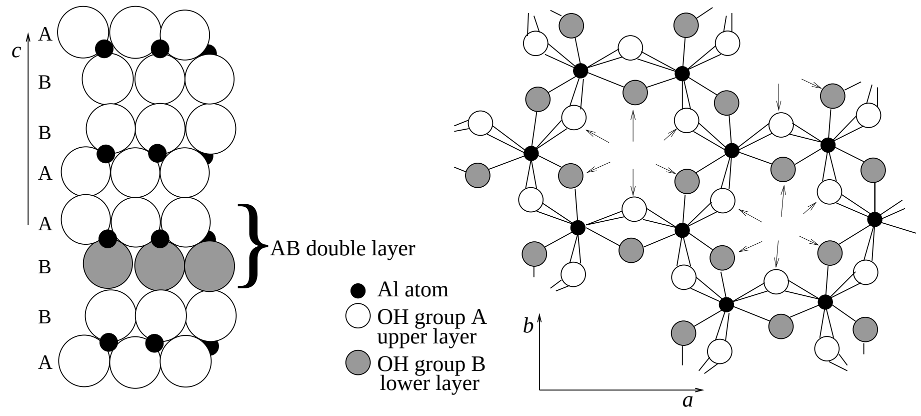

Figure 6.2: Projections of the atomic arrangement of the gibbsite structure; on the left, a view along ***b***: the structure consists of double layers (AB) of close packed OH groups with Al atoms occupying two third of the octahedral interstices within the layers; on the right, a top-view of an AB layer along ***c***: each aluminium atom is octahedrally bonded to three O atoms of layer A and to three O atoms of layer B. Due to the fact that $\frac{1}{3}$ of the octahedral interstices is empty, the hexagonal arrangement is somewhat distorted [17].

6.3.2 Growth units

To apply the connected net analysis to the structure of gibbsite, the relevant growth units of the crystal growing from solution must first be defined. It is assumed that the growth of gibbsite takes place by the addition of $Al(OH)_3$ from dissolved $Al(OH)_4^-$ thereby releasing an OH^- group (chapter 4). Therefore, one $Al(OH)_3$ group is considered as the growth unit. These growth units can not be chosen unambiguously in the AB layer, since each O atom is shared between two Al atoms and each Al atom is octahedrally surrounded by 6 O atoms. Moreover, the interaction of aluminium and oxygen is known to be significantly covalent instead of being purely coulombic [18]. This suggests that the crystal growth process behaves partly as a chemical reaction, creating a kind of supramolecular AB layer, and this making it even more difficult to define separate growth units in the crystal structure. However, since part of the Al-O interactions are already present in the solution, and only rearrange after integration in the gibbsite structure, the definition of $Al(OH)_3$ as the growth unit seems reasonable. This results in 8 growth units per unit cell, situated at the positions which are given in table 6.1. These positions correspond to four Al atoms in the lower AB layer and four Al atoms in the upper BA layer.

Table 6.1: Relative coordinates of the growth units in the unit cell of gibbsite. In addition, the symmetry relations between the growth units are given.

Growth unit	Position			Symmetry		
	x	y	z	2_1	n	$\bar{1}$
1	0.163904	0.545691	0.995792	2	4	3
2	0.336096	0.045691	0.504208	1	3	4
3	0.836096	0.454309	0.004208	4	2	1
4	0.663904	0.954309	0.495792	3	1	2
5	0.335109	0.041911	0.996412	6	8	7
6	0.164891	0.541911	0.503588	5	7	8
7	0.664891	0.958089	0.003588	8	6	5
8	0.835109	0.458089	0.496412	7	5	6

6.3.3 Bond energies

As was mentioned in the previous section, it is impossible to define the growth unit as a separate $Al(OH)_3$ molecule within the AB layer in the crystal structure. Therefore, an unconventional approach is adopted. A growth unit is, more precisely, defined as an aluminium atom with half of each of the six surrounding hydroxide groups. This implies the use of an occupancy factor of 1/2 for each of the six hydroxides, resulting in an $Al(OH)_{6/2}$ growth unit. Thus, these growth units share each of their hydroxides with a first neighbour aluminium and maintain the stoichiometry in this way. The crystallisation energy is then taken as the sum of the interactions between these growth units instead of the total crystal energy produced by taking all the interactions into account. Effectively, this energy definition will disregard half of the Al-O interactions since these were already present in the solution. The ...AB-BA... layer-layer interactions are formed by hydrogen bridges between the hydroxides and can be calculated straightforwardly.

The interaction energies between the growth units needed for the Hartman-Perdok method were determined using a forcefield approach. For this, an adapted version of the General Utility Lattice Program (GULP) by Gale [19] was used. Forcefield parameters were taken from the results of previous work [5], which had been fitted to reproduce the crystal structure and its vibrational modes. The gibbsite structure was relaxed using the default improved Newton-Raphson minimisation algorithm in GULP. The bonds were calculated as the sum of the pairwise atomic interaction energies between the growth units using the occupancy factor described above. Table 6.2 shows the asymmetric set of significant interaction energies. The 1 - 1 [010] and 1 - 3 [001] bonds show that our definition of a growth unit, which is charge neutral, circumvents the strong long range interaction energies encountered in the structure between separate, charged aluminium atoms and hydroxide groups. As the latter bonds are relatively weak, they can be neglected.

The hydrogen bridge interactions between the AB layers give rise to a nearest neighbour and a second nearest neighbour interaction. Relative to the layer plane, these 2 H-bonds possess perpendicular and oblique orientations respectively. The nearest neighbour interaction perpendicular to the layers effectively combines three hydrogen bonds, whereas the oblique interaction is only made up of one. The minimisation of the gibbsite structure showed a similar effect on the hydrogen positions as was reported by Lee et al. [3]. The hydrogen bonding oxygens tend to divert from the crystallographic positions, distorting the hydrogen bridge pattern. This shows that the hydrogen bridge potential is not accurately reproduced by the forcefield and indicates a strong repulsive effect of the forcefields. The hydrogen bridge interactions are expected to be more attractive in reality. However, since the interactions decrease rapidly at increasing distances and the oblique hydrogen bridge interactions are small, these can be neglected.

Therefore, the analysis is limited to the first six interactions presented in table 6.2. This set can be made complete by applying the crystallographic symmetry operations.

Table 6.2: Growth unit interaction energies in gibbsite obtained from forcefield calculations. The translation denotes the unit cell of a second growth unit relative to the first in the [*uvw*] direction. A translation [000] implies, thus, that the interaction between two growth units inside one unit cell is considered. The six strongest interactions are used for the connected net analysis.

Growth units	Translation	Energy (kJ/mol)	Label
1 - 5	[010]	-2410	o
5 - 7	$[0\bar{1}1]$	-2444	p
1 - 5	[000]	-2428	q
1 - 3	$[\bar{1}01]$	-2447	r
1 - 6	[001]	-209	s
1 - 6	[000]	-227	t
1 - 1	[010]	6.40	
1 - 3	[001]	-36.7	
1 - 2	[000]	-69.5	

6.3.4 Crystal graph and predicted morphology

As follows from the bond analysis in the previous section, the set of significant interactions is reduced to strong nearest neighbour interactions within the layers via double hydroxo bridges and the much weaker AB-BA interactions between layers via three H bridges. This reduces the structure of gibbsite to a basic crystal graph with each growth unit having 5 bonds, two of which connect the AB layers; the other three being situated within a layer (see figure 6.3).

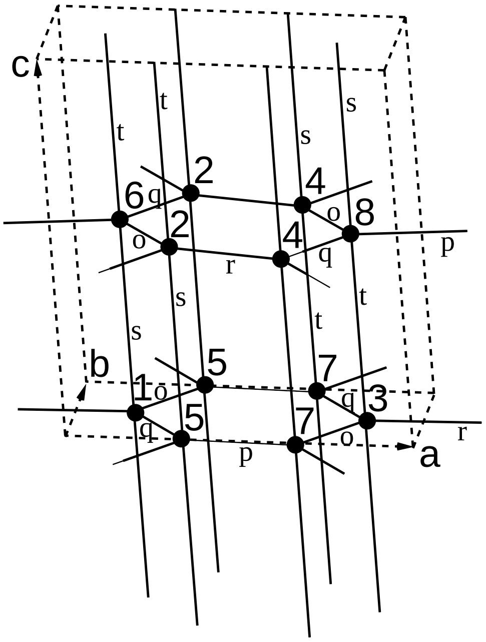

Figure 6.3: The crystal graph of the simplified gibbsite structure, with only Al atoms illustrated. There are 8 growth units per unit cell, each having 5 interactions connecting neighbouring growth units. The different interactions are denoted by *o*, *p*, *q*, *r*, *s* and *t* (see table 6.2). The three bonds inside an AB layer (*o*, *p* and *q*) are built up of double hydroxo bridges. The bonds between the layers (*s* and *t*) are much weaker. Each one is built up of three hydrogen bridges.

Using this crystal graph, all connected nets of gibbsite were determined along with their associated E_{hkl}^{att} energies [10,20]. Table 6.3 presents a summary of all 251 connected nets found. For each face $\{hkl\}$ the attachment energy of the strongest connected net is given and, in addition, the table shows whether this connected net is a singlet *s* or belongs to a multiplet *m*. In the case of a singlet, a connected net (hkl) is not related by symmetry to any other connected net of the same orientation (hkl). A multiplet contains more (mostly 2) symmetry related connected nets of the orientation (hkl). The crystal graph looks rather simple because of the symmetry relations between various bonds. The large number of connected nets is the result of the large number of growth units (8) in the cell.

By applying the Wulff construction to the calculated attachment energies (eq. (6.2)), the growth morphology of gibbsite was determined (see figure 6.4). The most prominent faces on this morphology are the $\{002\}$ faces. Furthermore, it shows the $\{110\}$, $\{101\}$ and $\{\bar{1}01\}$ faces and very small $\{011\}$ faces. This predicted morphology is similar to the growth morphology predicted by Lee et al. [3]. The presence of relatively large $\{101\}$ and $\{\bar{1}01\}$ chamfered faces results in a morphology elongated along $\boldsymbol{b}$.

Table 6.3: Connected nets found for the gibbsite structure as defined in the crystal graph. The interplanar distance d_{hkl} and the number (#) of connected nets are given. In addition, the attachment energy of the strongest connected net is mentioned. s and m denote whether the strongest connected net is a singlet or is part of a multiplet.

$\{hkl\}$	d_{hkl}(Å)	#	E^{att}_{hkl} (kJ/mol)
$\{002\}$	4.853	2	-1744 s
$\{200\}$	4.328	26	-9782 s
$\{110\}$	4.380	45	-9676 s
$\{101\}$	6.220	20	-5724 s
$\{10\bar{1}\}$	6.730	20	-5730 s
$\{011\}$	4.499	46	-10548 m
$\{112\}$	3.189	4	-13374 s
$\{11\bar{2}\}$	3.318	4	-13377 s
$\{111\}$	3.934	38	-12940 m
$\{11\bar{1}\}$	4.054	38	-12940 m
$\{211\}$	3.064	4	-17849 m
$\{21\bar{1}\}$	3.178	4	-17849 m

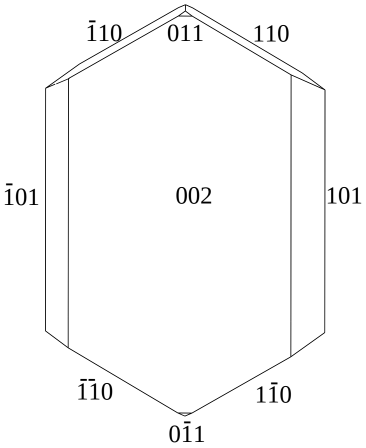

Figure 6.4: The growth morphology of gibbsite based on E^{att}_{hkl}, with $\{002\}$ basal, $\{110\}$, $\{101\}$ and $\{10\bar{1}\}$ side and small $\{011\}$ faces.

6.4 Monte Carlo simulation

Although morphology predictions based on attachment energies usually correspond reasonably well with experimental results, the theoretically predicted morphology of gibbsite is not in accordance with the basic experimental growth morphology, as shown in figure 6.1. These discrepancies are not the result of symmetry roughening, as explained in section 6.2.2. Table 6.3 shows that the orientations found on gibbsite crystals, namely $\{002\}$, $\{110\}$, $\{200\}$, $\{101\}$, $\{10\bar{1}\}$, $\{112\}$ and $\{11\bar{2}\}$ have a singlet as the most stable connected net. The other orientations have a doublet as the most stably connected net, and hence symmetry roughening of these orientations would be expected to occur. However, for these orientations a singlet is also present with a higher energy which determines the stability of the face. Therefore, symmetry roughening can not occur for these faces.

In order to study the discrepancies between the theoretical and experimental morphology, a Monte Carlo algorithm Monty [21] for crystal growth was used. This algorithm can simulate crystal growth from an isotropic mother phase in any direction on any given crystal, using the crystal graph. At present, a 2D nucleation mechanism is implemented. By calculating the probability to attach or detach growth units on every site on the crystal face, its growth can be simulated using the Monte Carlo algorithm. It was shown in chapter 4 from a fit of theoretical growth rate equations with experimental growth rate data, that a 2D nucleation mechanism is the most plausible mechanism for gibbsite crystallisation for all faces without defects. Thus, application of Monty is expected to be well-suited for gibbsite. The simulations were performed for all faces of table 6.3 and, in addition, for the face $\{010\}$ which has no connected nets. Figure 6.5 shows the simulation results. The graph presents the sticking fractions for the various faces, as a measure for the relative growth rates, versus the driving force for crystallisation, which is specified as the energy of a growth unit in the mother phase. Equilibrium ($\frac{\Delta\mu}{kT}$=0) is at -3800 kJ/mol. Decreasing the absolute chemical potential of a growth unit in the mother phase corresponds to increasing the driving force $\frac{\Delta\mu}{kT}$. In figure 6.5, the on-set of a particular growth curve indicates the threshold of the driving force at which that face will start to form stable 2D nuclei and, thus, grow. The higher the threshold driving force, the more stable the face (i.e. higher MI). The graph indicates that the different faces of gibbsite behave differently. At zero driving force, the $\{010\}$ faces grow rough. This is in accordance with the fact that the $\{010\}$ faces have no connected nets. It seems that the $\{011\}$, $\{211\}$ and $\{21\bar{1}\}$ faces also grow rough: immediately after applying a driving force $\frac{\Delta\mu}{kT} > 0$, the relative growth rates are $\frac{3}{4}$ for $\{011\}$ and $\frac{7}{8}$ for $\{211\}$ and $\{21\bar{1}\}$. This suggests that due to the topology of the faces these fractions of the crystallographic positions are available for growth without a barrier. Nevertheless, there is a barrier for the remaining fraction of the growth units. The next group of faces that starts to grow at increasing $\frac{\Delta\mu}{kT}$ are the $\{101\}$, $\{10\bar{1}\}$, $\{111\}$, $\{11\bar{1}\}$, $\{112\}$ and $\{11\bar{2}\}$ chamfered faces, although the E^{att}_{hkl} of the $\{101\}$ and $\{10\bar{1}\}$ faces is such that a large MI of these faces would be expected. The on-set of growth for the chamfered faces occurs far earlier than for the $\{200\}$ and $\{110\}$

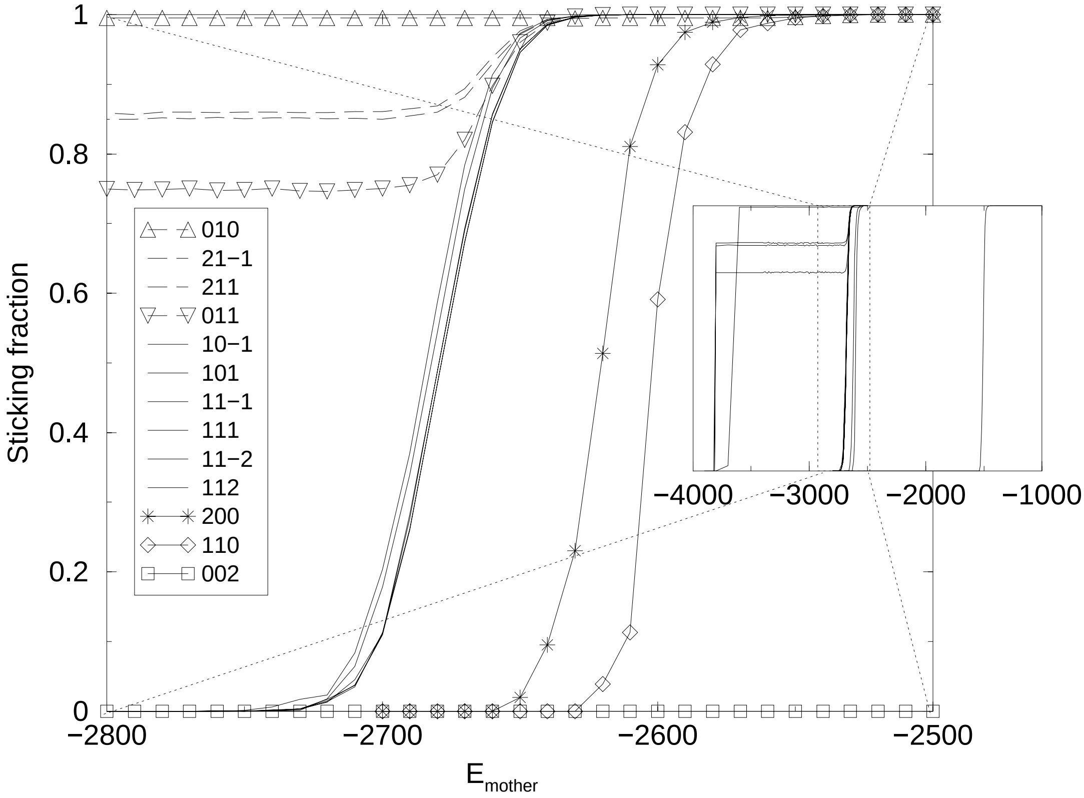

Figure 6.5: Monty simulation results of the sticking fraction, S, versus driving force for the faces of gibbsite crystals. The sticking fraction is the ratio of the amount of attached growth units minus the amount of detached growth units and the amount of attached ones, $\frac{\#_{att} - \#_{det}}{\#_{att}}$. The driving force is specified with respect to the energy of a growth unit in the mother phase, the equilibrium lying at -3800 kJ/mol. The curves appear in the order of the legend.

side faces. The difference between these latter faces shows that the $\{200\}$ faces must have a significant lower MI than the $\{110\}$ faces, although their E^{att}_{hkl} is nearly identical. The curve for the $\{002\}$ basal faces is shown in the inset of figure 6.5. These faces start to grow upon much higher driving force, indicating a very high MI. These results show that the MI for the relevant gibbsite faces would follow: $\{002\} \gg \{110\} > \{200\} > \{112\}$, $\{11\bar{2}\}$ $\approx \{111\}$, $\{11\bar{1}\} \approx \{101\}$, $\{10\bar{1}\}$. This is, in contrast to the E^{att}_{hkl} results, in agreement with the experimental results (see also figure 6.1).

The simulations show that at zero driving force, the growth morphology of gibbsite will be hexagonal with $\{002\}$, $\{110\}$, $\{200\}$, $\{112\}$, $\{11\bar{2}\}$, $\{101\}$ and $\{10\bar{1}\}$ faces, as shown on the left side of figure 6.6. This is in fact the equilibrium morphology determined by the specific surface energy. The simulation results show only a very small difference between the $\{112\}$, $\{11\bar{2}\}$ and the $\{111\}$, $\{11\bar{1}\}$ faces. Since the $\{112\}$ and $\{11\bar{2}\}$ faces are mainly observed on gibbsite crystals, these faces are suggested to prevail above $\{111\}$ and $\{11\bar{1}\}$. Note that the equilibrium morphology is still dependent on the temperature.

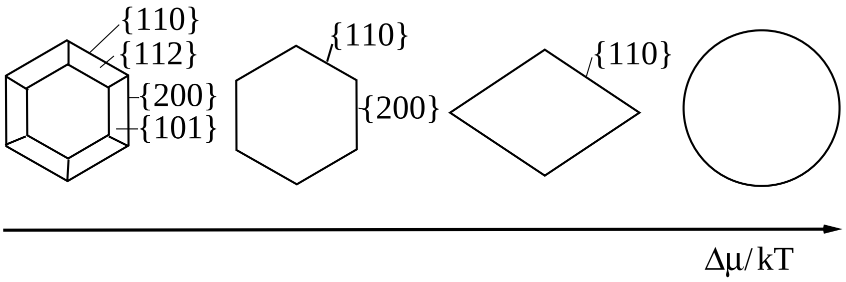

Figure 6.6: Morphology of gibbsite for increasing driving force based on the simulation results. The morphology on the left is the equilibrium morphology. All top faces are {002}.

It is possible that at higher temperatures, certain faces will be thermodynamically rough. By increasing the driving force, certain faces will start to grow. The {101}, $\{10\bar{1}\}$, {112} and $\{11\bar{2}\}$ chamfered faces have the lowest MI and grow rapidly at low driving force, followed by the {200} and {110} prismatic faces, respectively, at higher driving force. This suggests that at a certain driving force, the {101}, $\{10\bar{1}\}$, {112} and $\{11\bar{2}\}$ chamfered and {200} prismatic faces will grow faster than the {002} basal and {110} prismatic faces, generating a lozenge-shaped morphology. At the highest driving force, all side faces will grow kinetically rough resulting in a rounded morphology. The {002} faces will stay flat even for very high driving forces.

In order to understand the results of the Monte Carlo simulations, some of the faces will be studied in more detail in the next section.

6.5 Connected nets and 2D nucleation

In this section, we will explain the difference between the attachment energy prediction and the results of the Monte Carlo simulations for a few of the relevant faces.

6.5.1 {101} and $\{10\bar{1}\}$

Based on the E^{att}_{hkl} criterion, the {101} and $\{10\bar{1}\}$ faces are, after the {002} faces, the most prominent. For these orientations, 20 connected nets were found (see table 6.3). The two most stable nets of each face are both singlets and contain the strongest bonds determining the slice energy. The results of Monty, however, suggest that the edge energy for realising a 2D nucleus on the surface is relatively low, resulting in a small MI.

First, attention is focussed on the {101} face. In order to determine the edge energy, a 2D nucleus on the surface of a {101} face must be constructed. Figure 6.7 shows the most stable singlet of the {101} faces in the [010] projection. Along the $[10\bar{1}]$ direction, this singlet consists of d, r and t bonds. The attachment bonds are the p and s bonds. Note that each d bond inside the layer is made up of two bonds, o and q, of the crystal graph in a zigzag pattern along the [010] direction. In the $[10\bar{1}]$ direction, several profiles for nuclei can be made. The nuclei with the smallest edge energies are indicated in figure 6.7 by the profiles $\alpha\delta\beta\gamma$ and $\alpha\delta\epsilon\gamma$ (the profile $\alpha\beta\epsilon\gamma$ is identical to $\alpha\delta\beta\gamma$). The edge energy of the nuclei is calculated as the difference in broken bond energy for the surface with and without a nucleus. In the case of the $\alpha\delta\beta\gamma$ nucleus, the surface energy is the difference of profiles $\alpha\delta\beta\gamma$ and $\alpha\beta\gamma$ which is equal to $r + 2t - p - 2s = 39$ kJ/mol. In the case of the larger nucleus, the broken bond energy is the difference of $\alpha\delta\epsilon\gamma$ and $\alpha\beta\gamma$ which is also $r + 2t - p - 2s = 39$ kJ/mol. Note that adding additional growth units of the profile $\beta\delta\epsilon\gamma$ does not change this edge energy. However, when adding growth units in the [010] direction, the edge energy of 39 kJ/mol is encountered for each profile $\alpha\delta\epsilon\gamma$ along [010].

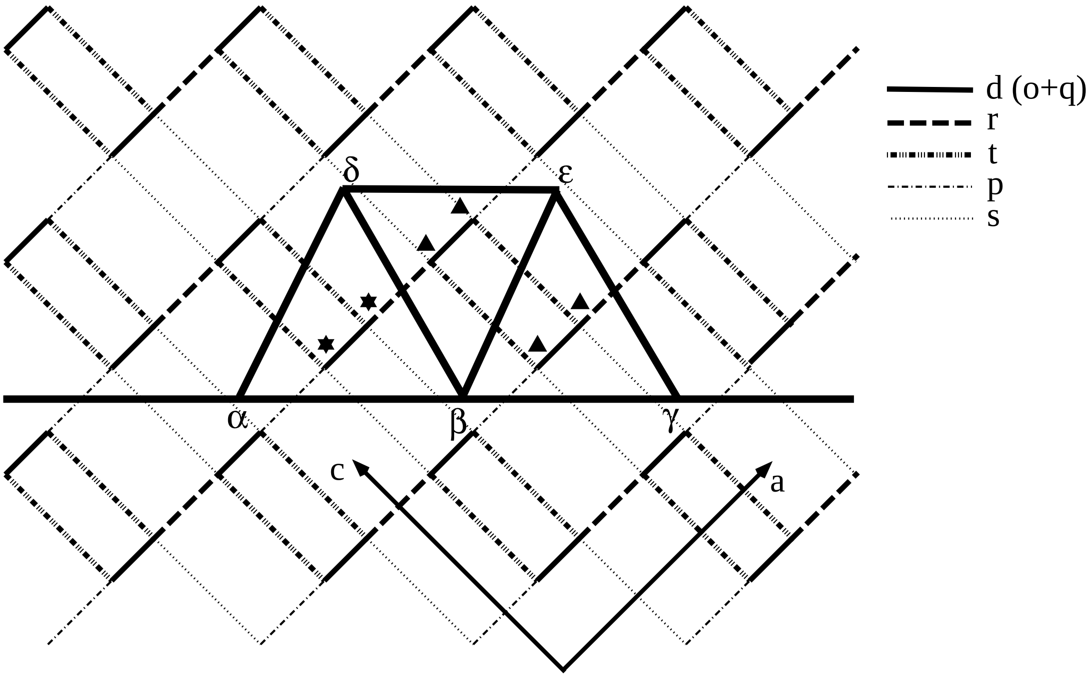

Figure 6.7: [010] projection of the crystal graph of gibbsite. The strongest connected net of the {101} face is indicated by the bold bonds. There are several nuclei indicated with the profiles $\alpha\delta\beta\gamma$ and $\alpha\delta\epsilon\gamma$. The profile $\alpha\beta\epsilon\gamma$ is identical to $\alpha\delta\beta\gamma$. The bond d consists of two bonds, o and q, in a zigzag pattern along the [010] direction. The growth units indicated with ★ and ▲, correspond to those of figure 6.8 and are referred to in the text.

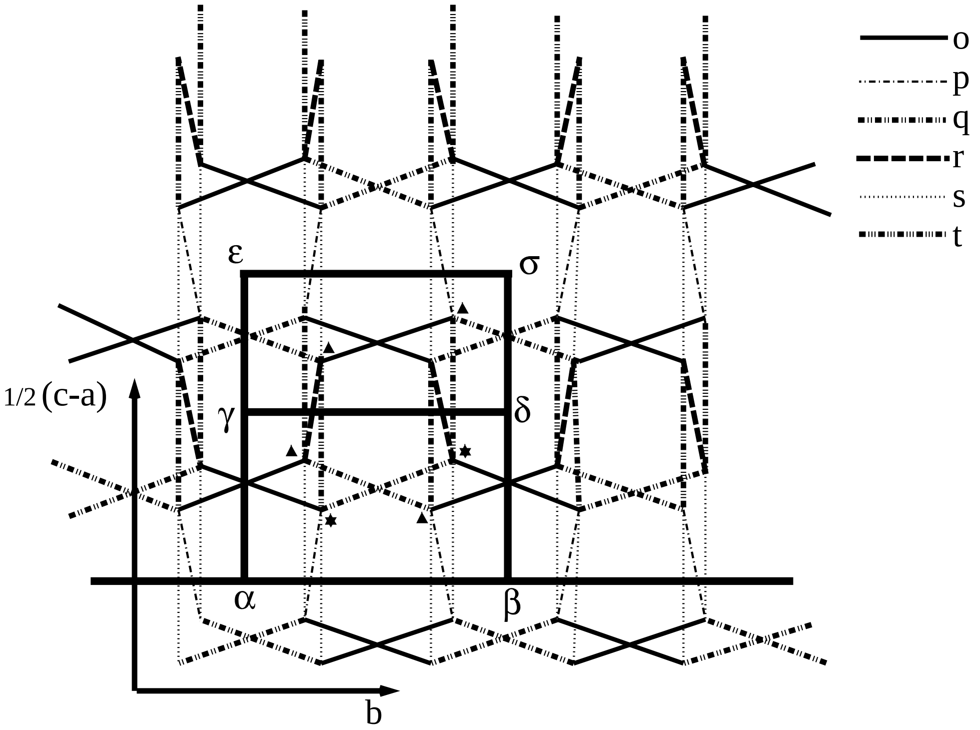

Figure 6.8: The strongest connected net of the {101} orientations in the $[\bar{1}01]$ projection. The small nucleus of figure 6.7 only contains the growth units indicated with ★; the larger nucleus contains those indicated with ★ and ▲.

Consider the $[\bar{1}01]$ projection of the {101} faces as presented in figure 6.8. The strongest connected net is indicated in bold bonds. The edge energy of 2D nuclei in the [010] direction can be calculated in a similar way. The two nuclei of figure 6.7 with the profiles $\alpha\delta\beta\gamma$ and $\alpha\delta\epsilon\gamma$ are indicated in figure 6.8 by the profiles $\alpha\gamma\delta\beta$ and $\alpha\gamma\epsilon\sigma\delta\beta$. The smallest nucleus $\alpha\delta\beta\gamma$ of figure 6.7, however, contains only two growth units. The addition of these two growth units forming this small nucleus is represented in figure 6.8 by the addition of the two growth units indicated with a ★. The edge energy is then the energy of only those bonds broken in the [010] direction which are attached to these growth units. Only the o and q bonds are relevant for this edge energy, because an enlargement of the nucleus along $[\bar{1}01]$ involves only these broken bonds. The attachment bonds p and s only contribute to the edge energy of the profile along $[\bar{1}01]$. The edge energy is equal to $2o = 4820$ kJ/mol. The edge energy of the same nucleus translated over $\frac{1}{2}\boldsymbol{b}$ is $2q = 4856$ kJ/mol. The large nucleus $\alpha\delta\epsilon\gamma$ of figure 6.7 is represented in figure 6.8 by the six growth units indicated with ★ and ▲. The broken bond energy of this nucleus is $4o + 2q = 14496$ kJ/mol. The edge energy of the same nucleus translated over $\frac{1}{2}\boldsymbol{b}$ is $4q + 2o = 11532$ kJ/mol. Figure 6.8 suggests that a nucleus of height $\frac{1}{2}d_{101}$, i.e. the nucleus $\alpha\gamma\delta\beta$ with four growth units, is possible. Such a nucleus, however, corresponds to the nucleus $\alpha\delta\beta\epsilon\gamma$ in figure 6.7 and, in fact, consists of two neighbouring nuclei.

The edge energy of nuclei in all other possible directions $[uvw]$ are expected to be much higher, since they do not follow PBC directions.

Thus, the most favourable nuclei will be those with edge energies of 39 kJ/mol in the $[\bar{1}01]$ direction and 4820 kJ/mol in the [010] direction. The edges of such nuclei give rise to the lowest nucleation barrier. Stable nuclei formed during the simulations are indeed bounded by these edges. They are composed of only two growth units in the $[\bar{1}01]$ direction and are strongly elongated in the [010] direction. The growth of the {101} layer by only these nuclei is, however, not possible, because they do not generate a complete growth layer, d_{101}. The formation of one layer d_{101} is only possible by making nuclei of the size $\alpha\delta\epsilon\gamma$, as shown in figure 6.7. The {101} faces grow through the formation of the nuclei $\alpha\delta\beta$ and $\beta\epsilon\gamma$ (figure 6.7) on which the remaining growth units are added to create the nucleus $\alpha\delta\epsilon\gamma$. The edge energies of the large nucleus are 39 kJ/mol in the $[\bar{1}01]$ direction and 11532 kJ/mol in the [010] direction.

It has been demonstrated by Monte Carlo simulations for a rectangular lattice that, a small edge energy in a single direction results in a low nucleation barrier [12,22]. Therefore, these faces will grow faster and become rough at lower driving forces as compared to isotropic faces. Thus, the {101} surfaces of gibbsite crystals will easily form nuclei at low driving forces which are elongated in the [010] direction. This explains why this face has a much lower MI than expected on the basis of E^{att}_{hkl} (eq. 6.2).

In chapter 2, it is reported that the MI for {101} and $\{10\bar{1}\}$ side faces are unequal. MONTY simulations indeed show a slight difference in the on-set of the curves. Calculation of the edge energy of nuclei on the $\{10\bar{1}\}$ faces in the [101] direction leads to 33 kJ/mol. The difference of 6 kJ/mol in energy of the 'cheapest' edges for these two faces is reflected in the separation of the simulation curves by approximately 7 kJ/mol.

6.5.2 {200} and {110}

In figure 6.9a, the [001] projection of the gibbsite crystal graph is drawn, showing the strongest {200} connected net by the bold bonds. There are two possibilities for constructing energetically favourable nuclei in the [010] direction. The edge energy for these nuclei is calculated by determining the broken bond energies of the surfaces bounded by $\alpha\delta\beta\gamma$ and $\alpha\delta\epsilon\gamma$ compared to the energy of the surface bounded by $\alpha\beta\gamma$. In the [001] direction, the repent growth units for both nuclei contains two growth units. Counting the broken bonds along [010] results in an edge energy of $d + d' - g' = 2o + 2q - p - r$ $= 4785$ kJ/mol for both nuclei. Note that the nucleus $\alpha\delta\epsilon\gamma$ with three growth units is of height d_{200}. The edge energy of 2D nuclei in the [001] direction of this face is the broken bond energy of hydrogen bonds, which is $6t$, or $\frac{1}{2}\boldsymbol{c}$ further, $6s$. These evaluate to 1362 and 1254 kJ/mol, respectively, for the large nucleus $\alpha\delta\epsilon\gamma$ with height d_{200}. The small difference between these two alternative edges shows that the surface is expected to show both edges. This implies that the relevant nuclei are those having only three growth units with edge energies of $o + q - r = 2391$ kJ/mol or $o + q - p = 2394$ kJ/mol, respectively, in the [010] direction and $3t + 3s = 1308$ kJ/mol in the [001] direction.

The edge energies in the $[\bar{1}\bar{1}0]$ direction for the corresponding nuclei of the {110} faces were calculated to be $q + p - o = 2462$ kJ/mol and $o + r - q = 2429$ kJ/mol, respectively. In the [001] direction of this face the edge energy is also $3t + 3s$ (1308 kJ/mol).

From these results, it is concluded that the nucleation barrier for making a 2D nucleus is lower for the {200} faces than for the {110} faces, resulting in a larger MI of the latter.

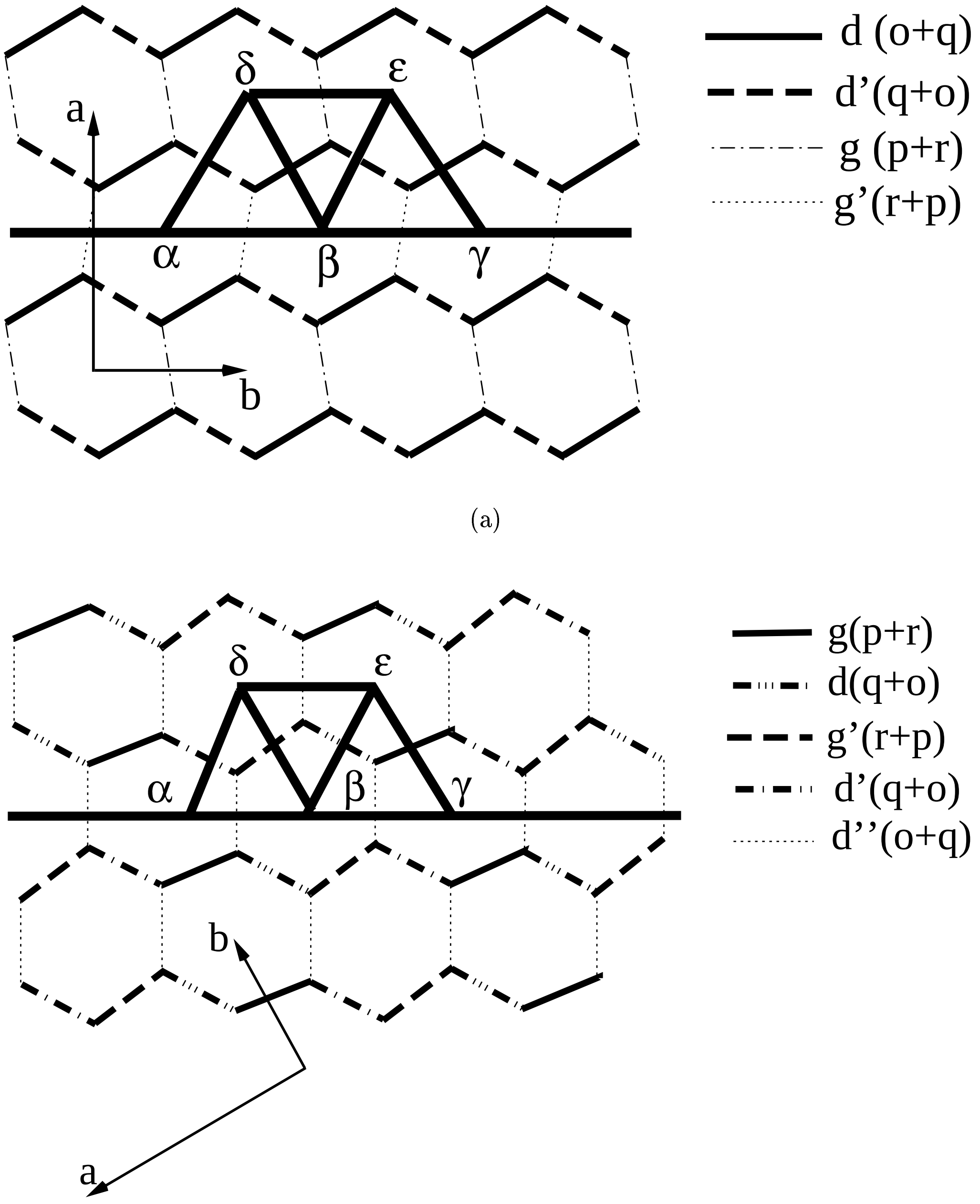

(a)

(b)

Figure 6.9: (a) [001] projection of the strongest connected net of the {200} face, and (b) [001] projection of the strongest connected net of the {110} face of the crystal graph of gibbsite. On both surfaces, 2D nuclei are drawn. In these figures, the *d* bonds are composed of *o* and *q* bonds which are mutually different in orientation. The *g* bonds are composed of *p* and *r* bonds.

Although the difference in edge energy is small, which was also reflected in the on-set of the curves in the Monty simulations, it is significant. Nonetheless, the results strongly suggest that the edge energy difference is of sufficient magnitude to induce the formation of lozenge-shaped crystals under suitable conditions.

6.5.3 {002}

On the {002} surface of gibbsite, only Kossel-like (i.e. parallelogram) nuclei can be made as can be seen in figure 6.10. The relevant directions in the pseudohexagonal structure are [010], [110] and [1$\bar{1}$0]. In each direction several nuclei can be made. The edge energy can be calculated, as shown before, by determining the difference in broken bond energy between the two surfaces. The edge energy in the [100] direction is $p + r + 2s - 2t$ (4855 kJ/mol) for the $\alpha\delta\epsilon\beta$ nuclei, and $p + r + 2t - 2s$ (4927 kJ/mol) for the $\beta\epsilon\phi\gamma$ nuclei. In the [010] direction, the edge energy is $2o = 4820$ kJ/mol or $2q = 4856$ kJ/mol. These edge energies are much larger than the differences in s and t, o and q and p and r bonds. Therefore, one can assume that the {002} faces grow with these small nuclei of size $\frac{1}{2}\boldsymbol{a}$. Note that for all three directions [010], [110] and [1$\bar{1}$0] these nuclei are comparable.

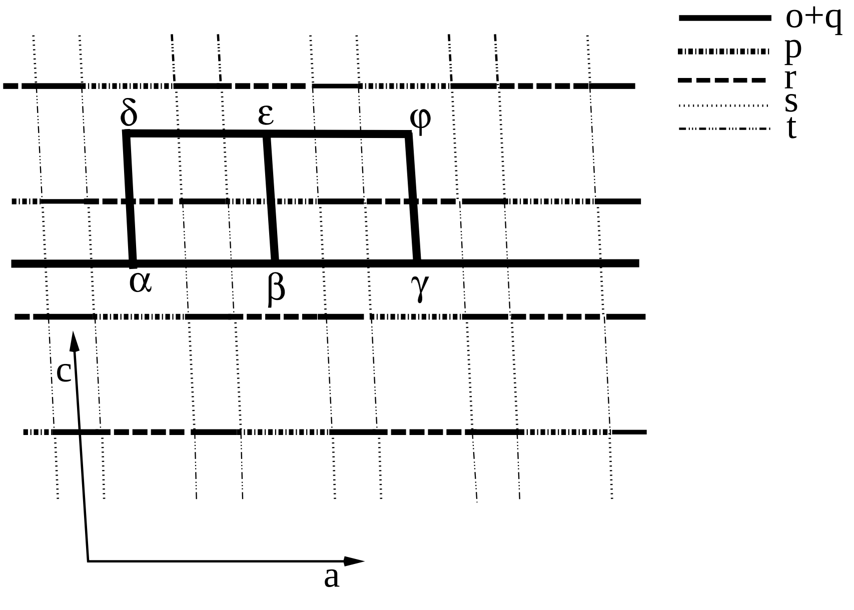

Figure 6.10: [010] projection of the {002} face of the crystal graph of gibbsite. Several nuclei are indicated.

6.6 Discussion

In the previous section, the edge energies have been calculated for nuclei on the experimentally observed surfaces of gibbsite crystals. With these results, the morphological importance of the faces is explained and can be compared with the growth curves as simulated with the Monte Carlo algorithm Monty. The edge energies were determined assuming that the connected net with the lowest attachment energy is the dominating surface configuration in that orientation. For these surfaces, nuclei with the lowest edge energies were analysed. However, it can not be ignored that alternative nuclei, with somewhat larger edge energies, will play a non-negligible role in the growth mechanism. Note that the Monte Carlo algorithm will probe all plausible nuclei with the appropriate probabilities. The present results explain in great detail the morphological results found both experimentally and in the simulations.

The main reason for the discrepancies between the experimental morphology and the predicted morphology based on the attachment energy, is that the edge energy of 2D nuclei for all relevant faces (besides the {002} faces) involves both attachment and slice bonds. This results in 'difference bonds' which can reduce the edge energies drastically. This effect of non-Kossel like bonding topologies has been observed in several other cases [14, 15].

The {101} surfaces easily form elongated nuclei with edges in the $[10\bar{1}]$ and [010] direction with edge energies of 39 and 11532 kJ/mol, respectively (see also table 6.4). In all other possible directions the edge energies of nuclei on {101} are much higher. The small edge energy in the $[10\bar{1}]$ direction causes the formation of nuclei at low driving force. The edge energy calculations explain why this face has a much lower MI than is expected on the basis of E^{att}_{hkl} (eq. 6.2).

Table 6.4: The edge energies of the 'cheapest' nuclei on the most relevant faces. The direction for the edge and the corresponding edge energy are given.

$\{hkl\}$	Direction $[uvw]$	Edge energy kJ/mol
{002}	[100]	4820
	[110]	4856
{200}	[010]	2391
	[001]	1308
{110}	$[1\bar{1}0]$	2429
	[001]	1308
{101}	$[10\bar{1}]$	39
	[010]	11532
$\{10\bar{1}\}$	[101]	33
	[010]	11532

The edge energies of the {200} and {110} faces are almost the same, as presented in table 6.4. However, the small difference in edge energy causes a lower barrier for 2D nucleation on the {200} face than on the {110} face, resulting in a larger MI of the latter.

This small difference results in the appearance of (truncated) lozenge-shaped crystals. The difference in edge energies is, however, rather small. The {002} face has by far the highest nucleation barrier in all directions, resulting in platy crystals with limited growth along ***c***. The morphology dependence on the driving force which results from the simulations (figure 6.6) was also observed experimentally (see figure 5.2 of chapter 5).

In solution, the edge free energies may be altered because of interactions with solution, the presence of complexes, a preordering effect of the mother phase at the interface, or impurities. The interaction of the mother phase with crystal faces may increase or decrease the surface energy and the edge energy for crystal faces $\{hkl\}$. This may result in a larger difference in edge energies and between the {200} and {110} faces, making the formation of lozenges even more probable. The effect of the solvent and impurities present in the solution may also influence the relative MI of other faces, such as the {101} and $\{10\bar{1}\}$ faces.

A remaining point of concern in the prediction of the growth morphology is the calculation of the bond energies, especially the hydrogen bridge interactions. It is suggested that these latter interactions are much stronger in reality than calculated by the adapted GULP program. This may especially affect the relative edge energies and, consequently, the MI of the basal face versus the side faces, since the interaction between the AB layers are only composed of hydrogen bridges.

Furthermore, surface relaxation can influence the growth morphology. In the analysis it is assumed that the crystal structure at the surface and in the bulk are the same. Relaxation lowers the surface energy. However, the difference is mostly small and the effect on the structure of the connected nets and, thus, on the edge energies is small. Moreover, the effect of surface relaxation turned out not to improve the prediction of the gibbsite morphology [5]. On the other hand, if it is possible to calculate the individual energies of the bonds at a relaxed surface, the effect on edge energies might be considerable as these derive from small differences between relatively large bond strengths.

6.7 Conclusions

In this chapter, the morphology of gibbsite crystals was examined on the basis of a detailed connected net analysis. The complete analysis of the simplified structure of gibbsite resulted in 251 connected nets. Growth units were defined for the gibbsite structure, which is comprised of bonded Al and O atoms possessing almost entirely covalent character. The growth units were defined as $Al(OH)_{6/2}$, specifically, an Al atom with half of the six surrounding OH groups.

The six strongest bonds between the growth units were used in the analysis. It was assumed that there are no other relevant interactions in the crystal lattice apart from the bonds defined in the crystal graph. Effects of long range interactions, surface relaxation and crystal-mother phase interactions were ignored.

The growth morphology based on E_{hkl}^{att} is hexagonal tabular parallel to {002} and bounded by the {110}, {101} and $\{10\bar{1}\}$ faces. Although morphology predictions based on attachment energies usually correspond well to experimental results, the theoretically predicted morphology of gibbsite is not in accordance with the basic experimental growth morphology.

To study these discrepancies, Monte Carlo simulations based on the edge energy were performed, showing that the MI of gibbsite faces is as follows: $\mathrm{MI}_{\{002\}} \gg \mathrm{MI}_{\{110\}} > \mathrm{MI}_{\{200\}} > \mathrm{MI}_{\{112\},\{11\bar{2}\}} \approx \mathrm{MI}_{\{101\},\{10\bar{1}\}}$. The equilibrium morphology at zero driving force is hexagonal bounded by the $\{002\}$, $\{110\}$, $\{200\}$, $\{112\}$, $\{11\bar{2}\}$, $\{101\}$ and $\{10\bar{1}\}$ faces. The specific surface topography of certain nets of F-faces $\{hkl\}$ leads to smaller effective edge (free) energies than expected on the basis of the slice energy. The barrier for making 2D nuclei is low, resulting in a relatively high growth rate at low driving force. At higher driving forces, the $\{112\}$, $\{11\bar{2}\}$, $\{101\}$ and $\{10\bar{1}\}$ faces will disappear first, followed by the $\{200\}$ faces, resulting in a lozenge-shaped morphology.

The complete connected net analysis of gibbsite shows that the growth rate of faces is no longer proportional to the attachment energy, but is determined by the actual edge (free) energy taking the relevant 2D growth mechanism into account. Furthermore, the definition of $\mathrm{Al(OH)}_{6/2}$ as growth unit is reasonable as this model is well able to explain the experimentally observed morphologies.

References

[1] T.G. Pearson, The chemical background of the aluminium industry (Royal Institute of Chemistry, London, Monograph no. 3, 1955).

[2] I. Seyssiecq, S. Veesler, G. Pèpe and R. Boistelle, J. Cryst. Growth 196 (1999) p. 174.

[3] M.-Y. Lee, A.L. Rohl, J.D. Gale, G.M. Parkinson and F.L. Lincoln, IChemE 74 (1996) p. 739.

[4] D.H. Gay and A.L. Rohl, J. Chem. Soc. Faraday Trans. 91 (1995) p. 925.

[5] S. Fleming, A. Rohl, G. Parkinson and M.-Y. Lee, J. Cryst. Growth 209 (2000) p. 159.

[6] P. Hartman and W.G. Perdok, Acta Cryst. 8 (1955) p. 49.

[7] P. Hartman and W.G. Perdok, Acta Cryst. 8 (1955) p. 521.

[8] P. Hartman and W.G. Perdok, Acta Cryst. 8 (1955) p. 525.

[9] P. Bennema, Growth and morphology of crystals: Integration of theories of roughenong and Hartman-Perdok theory, In D.T.J. Hurle, editor, *Handbook of crystal growth, vol. 1* p. 476–581, Elsevier Science Publ. (1993).

[10] R.F.P. Grimbergen, H. Meekes and S.X.M. Boerrigter (1997), C-program FACELIFT for connected net analysis, Dept. of Solid State Chemistry, University of Nijmegen.

[11] H. Meekes, P. Bennema and R.F.P. Grimbergen, Acta Cryst A54 (1998) p. 501.

[12] R.F.P. Grimbergen, H. Meekes, P. Bennema, C.S. Strom and L.P.J. Vogels, Acta Cryst A54 (1998) p. 491.

[13] R.F.P. Grimbergen, P. Bennema and H. Meekes, Acta Cryst A55 (1999) p. 84.

[14] R.F.P. Grimbergen, H. Meekes, P. Bennema, H.J.F. Knops and M. den Nijs, Phys. Rev. B 58 (1998) p. 5258.

[15] F.F.A. Hollander, S.X.M. Boerrigter, J. van der Streek, R.F.P. Grimbergen, H. Meekes and P. Bennema, J. Phys. Chem. B 103 (1999) p. 8301.

[16] H. Saalfeld and M. Wedde, Z. für Kristall. 139 (1974) p. 129.

[17] K. Wefers and C. Misra, Oxides and Hydroxides of Aluminium, Technical Report Technical Paper no. 19, revised Alcoa Research Laboratories, Pittsburgh, Pennsylvania (1987).

[18] S.S. Zumdahl, in: Chemical Principles (D.C. Heath and Company, 1995) p. 843 2^{nd} edition.

[19] J.D. Gale, J. Chem. Soc. Faraday Trans. 93 (1997) p. 629.

[20] Cerius^2 User Guide, September 1998. San Diego: Molecular Simulations Inc., 1998.

[21] S.X.M. Boerrigter, G. Josten and H. Meekes, Monte Carlo algorithm MONTY for crystal growth, Dept. of Solid State Chemistry, University of Nijmegen.

[22] J.P. van der Eerden, C. van Leeuwen, P. Bennema, W.L. van der Kruk and B.P.Th. Veltman, J. Appl/ Phys. 48 (1977) p. 2124.

Summary

The crystallisation of gibbsite, γ-Al(OH)$_3$, is an important step in the production of alumina, Al_2O_3. The latter is the material from which aluminium is extracted. Nowadays, the production of alumina is most widely achieved via the Bayer process. In this process, gibbsite is crystallised from seeded sodium aluminate solution, $NaAl(OH)_4$, and is subsequently calcined to alumina. The quality of gibbsite determines the quality of alumina. For that reason, the particle size, the morphology, strength, amount of agglomeration of the gibbsite crystals and the incorporation of impurities are important parameters. Fundamental knowledge of the crystallisation process is necessary to optimise the crystallisation step and to improve the quality of the crystals. The results of a laboratory study of the crystallisation of gibbsite according to the Bayer process are described in this thesis.

Experiments on the crystallisation of gibbsite from unseeded sodium aluminate solutions reveal gibbsite crystals and agglomerates with various morphologies. Many of the crystals are twinned. The various kinds of twinning and the effects on the growth morphology and growth kinetics are discussed in chapter 2. It is shown that single non-twinned crystals are lozenge-shaped, mainly bounded by {001} top and {110} side faces. The relative occurrence of the various faces shows that the morphological importance (MI) of the faces follows the sequence $MI_{\{001\}} \gg MI_{\{110\}} > MI_{\{100\}} > MI_{\{101\}} \approx MI_{\{112\}}$. Single or multiple twinning, dislocations and the presence of impurities lead to the formation of other crystal shapes: large hexagonal plates and prisms. Most of the hexagonal plates are twinned sixfold on {110}, with {001} as basal faces and {100} as side faces. The twinning already occurs at the initial stage of nucleation. The combination of fast growing {100} faces and a nucleation mechanism at the reentrant corners results in large crystals with sizes up to 200 micrometers in diameter. The small prismatic crystals are formed when the lateral growth is inhibited, apparently by impurities. Because the lozenge-shaped gibbsite crystals are single crystalline, it is concluded that these crystals exhibit the basic morphology instead of the hexagons, normally considered as the basic morphology in the literature.

To understand the growth and interface properties of the three main types of gibbsite crystals, i.e. lozenges, hexagons and prisms, a study of the surface topography using optical and atomic force microscopy is done and described in chapter 3. Many of the lozenges show no dislocation sources. This suggests that the growth of these crystals proceeds exclusively by a 2D nucleation mechanism and subsequent step advancement. Lozenges which grow to somewhat thicker crystals show one or a few screw dislocations ending on the basal face. The second type of crystals, the sixfold twinned hexagons, has a complex surface topography as a result of many defects. The various growth features on the {001} faces are shown to be the result of defects in the crystals and inhomogeneities in their environment. The lowest steps observed are about 5 Å high, which is equal to

half of the unit cell dimension along $\boldsymbol{c}$ in accordance with the selection rules of the space group. 2D nucleation at the reentrant corners at the outcrops of twin planes is shown, which verifies the lateral growth mechanism for sixfold twinned crystals as suggested in chapter 2. Crystals of the third major crystal morphology found, prisms, also exhibit many defects. Mosaicity is observed and related to the presence of misaligned crystallites or impurities. It is shown that most gibbsite crystals contain many defects and that each type of morphology reveals a different surface structure.

In-situ optical microscopy has been used to study the growth rates of the individual faces of the different types of gibbsite single crystals growing from aqueous sodium aluminate solutions. The growth rate measurements are presented in chapter 4. The growth rates are measured for the {100} and {001} faces in case of twinned hexagons and {110} faces for single crystalline lozenges. To interpret these results, a definition of the driving force adapted for gibbsite crystallisation from caustic aluminate solution is derived in this chapter. Furthermore, besides the well-known crystal growth models for birth and spread and spiral growth, a new analytical model for enhanced 2D nucleation at the intersection lines of contacting crystals is introduced. Although the crystals were grown under the same external conditions, a significant growth rate dispersion was observed for crystallographically equivalent faces of crystals of the same type. The average growth rates measured as a function of the driving force are fitted with the growth rate equations for the various growth mechanisms. It is shown that a birth and spread-type growth rate equation as well as the equation for contact nucleation growth derived in this chapter can be used to describe the growth rate of gibbsite under various growth conditions for all crystallographic directions. This is in accordance with the surface topography studies reported in chapter 3.

In chapter 5 the effect of a wide range of growth conditions and inorganic impurity additions on the growth morphology of gibbsite crystals is characterised using scanning electron microscopy. These observations lead to the description of a general morphology evolution during the crystallisation process. Crystallisation starts with the formation of thin, rounded hexagons and faceted lozenges, which upon further growth develop into faceted plates and blocks with well-formed basal, prismatic and chamfered faces. Finally, large blocks with many defects and stress regions are formed. This morphology evolution has only a weak dependence on the growth conditions. Changing the external conditions, i.e. increasing driving force and/or caustic concentrations, just leads to a faster development of the morphology evolution. Moreover, increasing the driving force or the caustic concentration leads to larger crystals. The influence of small amounts of inorganic impurities on the growth of gibbsite crystals turns out to be negligible. In contrast, gibbsite crystals grown from potassium aluminate solutions show a morphology which is elongated along the c-axis. This indicates that the alkali ions of the solution have a major influence on the morphology of gibbsite crystals.

Experiments show that despite the fact that the structure of gibbsite is pseudo-hexagonal, a lozenge-shaped morphology is energetically the most favoured one. The theoretical morphology of gibbsite on the basis of a detailed connected net analysis is the subject of chapter 6. This method relies on determining crystal faces parallel to connected nets in the crystal structure, followed by calculation of the edge energy of 2D nuclei for each face. By subscribing the highest morphological importance to the faces with the highest value of edge (free) energy, i.e. the highest nucleation barrier, the growth morphology is obtained. Growth units are defined as $Al(OH)_{6/2}$, specifically, an Al atom with half of the six surrounding OH groups. It shows that 251 different connected nets corresponding with 12 crystal faces can be identified. Monte Carlo simulations based on 2D nucleation growth of these faces show that their MI follows: $MI_{\{002\}} \gg MI_{\{110\}} > MI_{\{200\}} > MI_{\{112\},\{11\bar{2}\}} \approx MI_{\{101\},\{10\bar{1}\}} \gg MI_{\{011\}} \approx MI_{\{211\},\{21\bar{1}\}}$. This corresponds well with the experimental observations. In this chapter, it is shown, with the complete connected net analysis of gibbsite, that the growth rate of faces is no longer proportional to the attachment energy, but is determined by the actual edge (free) energy together with the relevant 2D growth mechanism.

In conclusion, gibbsite crystals have many different growth morphologies. It is fascinating that crystals with different morphologies grow simultaneously in the same batch. This study reveals that gibbsite crystals free from dislocations mainly expand laterally, resulting in an ultra thin lozenge-shaped morphology. Here, growth probably proceeds by a 2D nucleation mechanism. Furthermore, this study indicates that the variation in growth morphology of gibbsite crystals is primarily the result of intrinsic properties of the material, like twinning and accumulation of growth imperfections, but also the continuous formation of nuclei during crystallisation, agglomeration and probably restructuring of the solution. This also explains the dispersion in growth rate of the crystals. External conditions, such as driving force, caustic concentration and impurities, seem to have only a small effect on the growth mechanism of gibbsite crystallisation. There is still an open question why the lateral growth rate of prisms is lower than that of plates and lozenges. This and several other aspects of gibbsite crystal growth are still shrouded in mystery and need clarification in the future.

Samenvatting

De kristallisatie van gibbsiet, γ-$Al(OH)_3$, is een belangrijke stap in de productie van alumina, Al_2O_3. De laatste verbinding is het materiaal waaruit aluminium wordt gemaakt. De productie van alumina wordt vandaag de dag mondiaal uitgevoerd via het zogenoemde Bayerproces. Dit proces bestaat uit twee stappen: de kristallisatie van gibbsiet uit natrium-aluminaat oplossing ($NaAl(OH)_4$) en het calcineren van gibbsiet naar alumina. De kwaliteit van het gibbsiet bepaalt uiteindelijk de kwaliteit van het alumina. Belangrijke parameters voor de kwaliteit van de gibbsietkristallen zijn: de deeltjesgrootte, morfologie, sterkte, mate van agglomeratie en inbouw van verontreinigingen in het kristalrooster. Fundamentele kennis van het kristallisatieproces is nodig om de kristallisatiestap te optimaliseren en zo de kwaliteit van het gibbsiet te vergroten. De resultaten van een studie naar de kristallisatie van gibbsiet volgens het Bayerproces staan beschreven in dit proefschrift.

Gibbsietkristallen en -agglomeraten verkregen door kristallisatie uit ongekiemde natrium-aluminaat oplossingen hebben verschillende vormen. Veel van de kristallen vormen tweelingkristallen. De verschillende soorten twinning en de effecten op de groeimorfologie en groeikinetiek worden beschreven in hoofdstuk 2. Eén-kristallijne, niet-getwinde kristallen zijn wybervormig en worden hoofdzakelijk begrensd door het $\{001\}$ topvlak en de $\{110\}$ zijvlakken. De relatieve verschijning van de verschillende vlakken op deze kristallen laat zien dat de morfologische belangrijkheid (Morphological Importance, MI) van deze vlakken de volgorde $MI_{\{001\}} \gg MI_{\{110\}} > MI_{\{100\}} > MI_{\{101\}} \approx MI_{\{112\}}$ heeft. Enkelvoudige of meervoudige twinning, dislocaties en de aanwezigheid van verontreinigingen leiden tot de vorming van andere kristalvormen: de hexagonale platen en paaltjes. De meeste hexagonale platen zijn zesvoudig getwind in het $\{110\}$ vlak, met $\{001\}$ als topvlak en $\{100\}$ als zijvlakken. De twinning treedt al op in de kiemvormingsfase. De combinatie van snel groeiende $\{100\}$ vlakken en een kiemvormings-mechanisme in de inspringende hoeken op de uiteinden van de twinvlakken leidt tot grote kristallen tot 200 micrometer in diameter. De kleine paalvormige kristallen zijn meestal ook getwind en worden gevormd als de laterale groei wordt tegengehouden door mogelijk aanwezige verontreinigingen. Omdat juist de wybervormige kristallen één-kristallijn zijn, is het aannemelijk dat deze vorm de basis morfologie van gibbsiet is in plaats van de hexagoon die in de literatuur normaal beschouwd wordt als de basis morfologie.

Om de groei- en de grensvlakeigenschappen van de drie hoofdvormen van gibbsietkristallen – de wybers, hexagonen en paaltjes – te begrijpen, is een studie naar de oppervlakte-topografie gedaan. Hierbij is gebruik gemaakt van optische en atomaire kracht microscopie. De waarnemingen zijn beschreven in hoofdstuk 3. Dunne, één-kristallijne wybers hebben vaak geen enkele dislocatiebron. Dit suggereert dat de groei van deze kristallen exclusief gebeurt door een 2-dimensionaal (2D) kiemvormings-mechanisme met stepvoortgang. Indien de één-kristallijne wybers slechts één of enkele schroefdislocaties eindigend aan het topvlak hebben, groeien ze uit tot iets dikkere kristallen. Het tweede type kristallen, de zesvoudig getwinde hexagonen, laat een complexe topografie van het oppervlakte zien. De verschillende groeikarakteristieken op het $\{001\}$ vlak zijn het resultaat van defecten in de kristallen en inhomogeniteiten in hun omgeving. De laagste steps die waargenomen zijn, zijn ongeveer 5 Å hoog. Deze hoogte is gelijk aan de helft van c-as van de eenheidscel. Dit is in overeenstemming met de selectieregels van de ruimtegroep. De oppervlakten van de $\{100\}$ zijvlakken worden gekarakteriseerd door richels parallel aan het $\{001\}$ topvlak. Stepbronnen zijn niet gezien op deze vlakken. Een versnelde 2D kiemvorming in de inspringende hoeken aan het uiteinde van de twinvlakken is wel waargenomen. Kristallen van het derde type morfologie, de paaltjes, hebben ook veel defecten. Mosaiciteit is waargenomen en gerelateerd aan de aanwezigheid van slecht georiënteerde kristallieten of verontreinigingen. Dit hoofdstuk laat zien dat de meeste gibbsietkristallen veel defecten bevatten en dat elk type morfologie een verschillende oppervlaktestructuur openbaart.

In-situ optische microscopie is gebruikt om de groeisnelheid van gibbsietkristallen gegroeid uit waterige natrium-aluminaat oplossingen te bestuderen. De groeisnelheidsmetingen, gemeten voor individuele vlakken van de verschillende typen gibbsietkristallen, zijn gepresenteerd in hoofdstuk 4. Dit zijn de $\{100\}$ en $\{001\}$ vlakken in het geval van getwinde hexagonen en de $\{110\}$ vlakken in het geval van één-kristallijne wybers. Om de resultaten te kunnen interpreteren is in dit hoofdstuk een definitie van de drijvende kracht voor gibbsietkristallisatie uit natrium-aluminaat oplossingen afgeleid. Verder is, naast de bekende kristalgroeimodellen voor 'geboorte en spreiding' (birth and spread of 2D kiemvorming) en spiraalgroei, een nieuw analytisch model voor versnelde 2D kiemvorming op de grenslijn van contacterende kristallen geïntroduceerd. Een opmerkelijke dispersie in groeisnelheid is gemeten voor kristallografisch equivalente vlakken van kristallen van hetzelfde type binnen één experiment, in de tijd en tussen verschillende experimenten, ondanks dat ze onder identieke externe groeiomstandigheden zijn gegroeid. De gemiddelde groeisnelheden als functie van de drijvende kracht zijn gefit met de groeisnelheidsvergelijkingen voor de verschillende groeimechanismen. Zowel de vergelijking voor een 2D kiemvormings-mechanisme als die voor contact-kiemvormings-groeimechanisme, afgeleid in dit hoofdstuk, beschrijven de groeisnelheid van gibbsiet voor alle kristallografische richtingen onder verschillende groeicondities. Dit is in overeenstemming met de oppervlakte topografie, zoals reeds gerapporteerd in hoofdstuk 3.

Hoofdstuk 5 behandelt het effect van de verandering in groeiomstandigheden, waaronder de toevoeging van verontreinigingen, op de groeimorfologie van gibbsietkristallen. De waarnemingen zijn gedaan met scanning elektron microscopie en hebben geleid tot een beschrijving van een algemene morfologie-evolutie tijdens het kristallisatieproces. Kristallisatie begint met de vorming van dunne, afgeronde hexagonen en gefaceteerde wybers. Deze ontwikkelen zich naar gefaceteerde platen en blokken met goed gevormde top-, zij- en schuine vlakken. Uiteindelijk worden grote blokken met veel defecten en spanningsgebieden gevormd. Deze morfologie-evolutie heeft slechts een zwakke afhankelijkheid van de externe groeicondities. Verandering van condities, zoals het verhogen van de drijvende kracht of de natriumhydroxide concentratie, leidt tot grotere kristallen. De invloed van kleine hoeveelheden verontreinigingen op de groei van gibbsiet is te verwaarlozen. Dit in tegenstelling tot gibbsietkristallen die gegroeid zijn uit kalium-aluminaat oplossingen. Deze vertonen juist een morfologie verlengd langs de c-as. Dit impliceert dat de alkali-atomen in de oplossing een grote invloed op de morfologie van gibbsietkristallen hebben.

Experimenten hebben laten zien dat, ondanks het feit dat de structuur van gibbsiet pseudohexagonaal is, een wybervormige morfologie energetisch de meest gunstige is. De theoretische morfologie op basis van een connected net analyse is het onderwerp van hoofdstuk 6. Deze methode is gebaseerd op het bepalen van kristalvlakken welke parallel liggen aan connected netten in de kristalstructuur, en vervolgens het berekenen van de randenergie van 2D kiemen voor elk vlak. Door het toekennen van de hoogste morfologische belangrijkheid (MI) aan de vlakken met de hoogste waarde voor de (vrije) randenergie (de hoogste kiemvormingsbarrière) wordt de groeivorm verkregen. In de gibbsietstructuur, welke bestaat uit gebonden Al en O atomen met een bijna volledig covalent karakter, zijn eerst groeieenheden gedefinieerd. Deze groeieenheden zijn gedefinieerd als $\mathrm{Al(OH)}_{6/2}$, een Al atoom met de helft van de zes omringende OH groepen. De connected net analyse identificeert 251 verschillende connected netten welke overeenkomen met 12 kristalvlakken. Monte Carlo simulaties, gebaseerd op een 2D kiemvormings-groeimechanisme, laten zien dat de MI van deze vlakken de volgorde $\mathrm{MI}_{\{002\}} \gg \mathrm{MI}_{\{110\}} > \mathrm{MI}_{\{200\}} > \mathrm{MI}_{\{112\},\{11\bar{2}\}} \approx \mathrm{MI}_{\{101\},\{10\bar{1}\}} \gg \mathrm{MI}_{\{011\}} \approx \mathrm{MI}_{\{211\},\{21\bar{1}\}}$ heeft. Dit is in goede overeenstemming met de experimentele resultaten. Aldus, de complete connected net analyse van gibbsiet laat zien dat de groeisnelheid van vlakken niet langer evenredig is met de aanhechtingsenergie, maar bepaald wordt door de actuele (vrije) randenergie samengaand met het relevante 2D kiemvormings-mechanisme.

Tenslotte, gibbsiet heeft veel verschillende groeivormen. Het is erg fascinerend dat kristallen met verschillende morfologie in hetzelfde experiment groeien. Deze studie laat zien dat dislocatievrije kristallen voornamelijk lateraal expanderen en resulteren in wybervormige kristallen. Groei gebeurt bij deze kristallen waarschijnlijk via een 2D kiemvormings-mechanisme. Verder laat deze studie zien dat de variatie in groeimorfologie van de gibbsietkristallen hoofdzakelijk het resultaat is van intrinsieke eigenschappen van het materiaal, zoals twinning en accumulatie van defecten, maar ook door de continue vorming van kiemen gedurende kristallisatie, agglomeratie en mogelijk herstructurering van de oplossing. Dit verklaart ook de gemeten dispersie in groeisnelheid van de kristallen. Externe condities, zoals de drijvende kracht, de natriumhydroxide concentratie en verontreinigingen, lijken slechts een klein effect op het groeimechanisme te hebben.

Nawoord

Het lijkt wellicht vanzelfsprekend om het schrijven van een proefschrift te vergelijken met het kristallisatieproces. Begrippen als kiemen, groei en kristalrooster laten zich makkelijk vertalen naar ideeën, kennisopbouw en structuur. Het kristallisatieproces staat ook nooit op zichzelf. Er moet een situatie gecreëerd worden om kristallen te laten kiemen en te laten groeien en de uiteindelijke vorm van het kristal wordt bepaald door de groeicondities en additieven. Zo ook het schrijven van een proefschrift.

Aan de bron van de totstandkoming van dit proefschrift staan Erwin van de Berg en Marcel Verheijen. Ik wil jullie bedanken voor het overbrengen van jullie enthousiasme omtrent de fascinerende wereld van kristallen en kristalgroei gedurende mijn stage bij de vakgroep Vaste Stof Chemie en voor de plezierige, soms ook hardhandige (letterlijk!) manier van begeleiden.

De prettige en enthousiaste begeleiding werd voortgezet door mijn twee begeleiders tijdens mijn promotie: Hugo Meekes en Willem van Enckevort. Het feit dat hun deuren altijd letterlijk en figuurlijk openstaan, doet de in andere vakgroepen aanwezige hiërarchie aanzienlijk verkleinen zo niet verdwijnen. Willem, jou wil ik in het bijzonder bedanken voor het helpen interpreteren van al die kristalgroeifenomenen en voor het grote correctiewerk dat je ondanks de drukte toch altijd snel gedaan had. Je experimentele gedrevenheid en theoretische kennis maken, in ieder geval bij mij, veel indruk. Hugo, jou wil ik bedanken voor het klankborden en het helpen ordenen van mijn soms warrige gedachten. Dit leidden altijd weer tot nieuwe inzichten. Tevens bedankt voor de prettige (soms te prettige) discussies en de geduldige en heldere uitleg over allerlei onderwerpen. Ondanks de vele waarschuwingen van jou, dat er nooit gezegd is dat het gemakkelijk zou gaan, hebben we die kleine kristallen toch aardig weten te dresseren.

Ab Rijkeboer, Iwan Hiralal en Erik Boom van Billiton wil ik speciaal bedanken voor het scheppen van dit onderzoek, voor de stimulerende discussies tijdens de bijeenkomsten en voor het kritisch doorlezen van het manuscript. Al leek de afstand tussen de fundamentele wetenschap en de procestechnologie soms wat groot, we hebben dat toch weten te overbruggen.

Natuurlijk ben ik veel dank verschuldigd aan Xavier Arnould en Heleen de Coninck, die ik tijdens hun stage heb mogen begeleiden. Heleen, je ziet waar die speculatieve gedachten omtrent gibbsietkristalletjes toe hebben geleid. Hartstikke bedankt voor jullie bijdragen en de gezellige samenwerking, merci bien.

Niet te vergeten zijn Marco, Stevie, Sean en Reinier. Jullie kennis en inspanningen hebben geleid tot het ontstaan van maar liefst twee echte jubel-hoofdstukken.

Al die andere wil ik bedanken die met hun aanwezigheid de afdeling gemaakt hebben tot welke zij is. Bedankt voor de collegiale sfeer, de gezellige praatjes, etentjes en afdelingsuitjes. Door jullie ben ik altijd met plezier naar de afdeling gegaan.

Een aantal mensen van de ondersteunende diensten ben ik zeer erkentelijk. Aan de vele foto's in dit proefschrift is te zien dat ik heel wat uurtjes achter de SEM heb doorgebracht.

Huub Geurts, bedankt voor het in topconditie houden van de 'oude' SEM en de hulp bij de nieuwe SEM, waarmee we nog meer fascinerende kristalgroeifenomenen waargenomen hebben. De mensen van de grote en kleine werkplaats hebben me zeer geholpen met het vervaardigen van de vele (proto)typen groeicelletjes, de verwerking van teflon tot 'sophisticated' roerders en de dynamische parallelroerder. De 'kebberrutvollevertrouwenin' heeft tot deze boeiende resultaten geleid.

Na dagen achter een microscoop of computer gezeten te hebben kon ik mijn overtollige energie en stress er altijd lekker 'uitboxen' tijdens een partijtje basketball. Ik denk met veel genoegen terug aan de late vrijdagavond trainingen van D1 van B.C. Heeze. Na een week hard werken was het altijd heerlijk om de geest te legen en de spieren te spannen. Nu speel ik alweer twee seizoenen bij D1 van Yellow Sox. (Ja inderdaad, we hebben gele sokken aan.) Jullie wil ik bedanken voor de hartelijke ontvangst en het opvangen van mijn stressuitspattingen van het afgelopen jaar. Enne Fem, ondanks dat ik geen gemakkelijke opdrachtgeefster was: chique kaft!

Mijn vrije tijd heb ik altijd op aangename wijze weten te vullen. Daan, Vero en Miek, we moeten die vrouwen-dagen toch maar eens frequenter gaan houden. Peter, Erwin en Enrico, nu ik niet meer in de buurt woon, kan ik helaas niet meer meedoen met het filmclubje. Naast de films mis ik vanzelfsprekend ook de lekkere etentjes: de pasta's, de bami's en de g(r)ie(r)s(t)(meel). Verder dank aan al mijn vrienden en kennissen voor alle gezellige etentjes, bierfeestjes en uitjes.

Ze zeggen wel eens: een goede buur is beter dan een verre vriend. Dit geldt zeker niet voor één vriendschap, die is en die blijft, al bijna dertig jaar lang! Biek bedankt, voor wie je bent en voor het lezen van het manuscript met al je zeer nuttige 'vraagjes'.

Pa en ma, bedankt voor jullie onbegrensde, zo vanzelfsprekend lijkende liefde, steun en vertrouwen. Jullie hebben mede de situatie geschapen dat ik kristallen ben gaan groeien. Ik ben klaar met studeren.

Tot slot, dank aan Eymert, jij hebt ook op andere gebieden van het leven dingen naar boven gebracht. Bedankt voor al die weekenden dat ik 'alleen maar bij kwam tanken'. Nu ga ik het huis schilderen.

Chantal

Curriculum Vitae

Naam: Chantal Sweegers
Geboren: 13 juli 1971 te Heeze

Opleiding:

1983 - 1989: V.W.O., Strabrecht College, Geldrop

1989 - 1995: Studie Scheikunde aan de Katholieke Universiteit Nijmegen

Hoofdrichting: Anorganische Chemie (Prof. Dr. Ir. J.J. Steggerda)
Stage-onderwerp: Synthese en karakterisering van verschillende goudfosfineclusters, en speciaal het goud-55 molecuul ($Au_{55}(PPh_3)_{12}Cl_6$), met spectroscopische technieken (infrarood-, UV/VIS- en NMR-spectroscopie) en electrochemie
Scriptie: Oxide/hydroxide verbindingen van aluminium, ijzer en silicium als homogene modelverbindingen voor heterogene katalytische dragermaterialen en de toepassing van deze verbindingen in katalytische systemen

Nevenrichting: Vaste Stof Chemie (Prof. Dr. P. Bennema)
Stage-onderwerp: *In situ* experimenten van caprolactam kristallen uit de gasfase en de groei van één-kristallen met behulp van Bridgeman en Tamman technieken

Werkervaring:

1995-2001: Onderzoeker bij de vakgroep Vaste Stof Chemie van Prof. Dr. E. Vlieg aan de Katholieke Universiteit Nijmegen
Onderzoeks-onderwerp: De kristallisatie van gibbsiet volgens het industriële Bayerproces
Het onderzoek werd gesponsord door Billiton International Metals B.V., Den Haag

2001- Werkzaam als Coating Engineer bij Philips Display Components, Eindhoven